A review of the remote sensing of lower tropospheric thermodynamic profiles and its indispensable role for the understanding and the simulation of water and energy cycles

Volker Wulfmeyer[1], R. Michael Hardesty[2], David D. Turner[3], Andreas Behrendt[1], Maria P. Cadeddu[4], Paolo Di Girolamo[5], Peter Schlüssel[6], Joël Van Baelen[7], and Florian Zus[8]

[1]Institute of Physics and Meteorology, University of Hohenheim, Stuttgart, Germany, [2]Cooperative Institute for Research in Environmental Sciences, University of Colorado, Boulder, Colorado, USA, [3]National Severe Storms Laboratory, National Oceanic and Atmospheric Administration, Norman, Oklahoma, USA, [4]Environmental Science Division, Argonne National Laboratory, Argonne, Illinois, USA, [5]Scuola di Ingegneria, Università degli Studi della Basilicata, Potenza, Italy, [6]European Organisation for the Exploitation of Meteorological Satellites, Darmstadt, Germany, [7]Laboratoire de Météorologie Physique, Observatoire de Physique du Globe de Clermont-Ferrand, Aubiere, France, [8]German Research Center for Geosciences, Potsdam, Germany

Abstract A review of remote sensing technology for lower tropospheric thermodynamic (TD) profiling is presented with focus on high accuracy and high temporal-vertical resolution. The contributions of these instruments to the understanding of the Earth system are assessed with respect to radiative transfer, land surface-atmosphere feedback, convection initiation, and data assimilation. We demonstrate that for progress in weather and climate research, TD profilers are essential. These observational systems must resolve gradients of humidity and temperature in the stable or unstable atmospheric surface layer close to the ground, in the mixed layer, in the interfacial layer—usually characterized by an inversion—and the lower troposphere. A thorough analysis of the current observing systems is performed revealing significant gaps that must be addressed to fulfill existing needs. We analyze whether current and future passive and active remote sensing systems can close these gaps. A methodological analysis and demonstration of measurement capabilities with respect to bias and precision is executed both for passive and active remote sensing including passive infrared and microwave spectroscopy, the global navigation satellite system, as well as water vapor and temperature Raman lidar and water vapor differential absorption lidar. Whereas passive remote sensing systems are already mature with respect to operational applications, active remote sensing systems require further engineering to become operational in networks. However, active remote sensing systems provide a smaller bias as well as higher temporal and vertical resolutions. For a suitable mesoscale network design, TD profiler system developments should be intensified and dedicated observing system simulation experiments should be performed.

1. Introduction

Earth's temperature and water distributions are essential for life. The understanding and the prediction of these variables are fundamental for a sustainable development of the Earth system. However, in the 21st century, geosciences are facing tremendous challenges. The understanding and the simulation of the water and energy cycles still show significant gaps on all temporal and spatial scales. Particularly, two scientific questions are essential for the environment and the society:

1. How predictable are extreme events and how can the predictive skill of model systems be improved?
2. How do the components of the regional and the global water and energy cycles change due to natural variability and anthropogenic influences?

These questions are addressed by a variety of national and international research programs such as the World Weather Research Program (WWRP) with respect to forecast ranges from nowcasting to the seasonal range as well as the World Climate Research Program (WCRP) [*Trenberth and Asrar*, 2014], particularly within the Global Energy and Water Exchanges (GEWEX) project, covering seasonal to decadal simulations and projections.

The success in answering these questions is strongly related to our understanding of key processes influenced by the three-dimensional (3-D) distributions of atmospheric water vapor (WV) and temperature (T) and how these fields evolve with time. These processes include (1) radiative transfer due to its strong sensitivity to WV and T profiles as well as the resulting implications on regional and global water and energy cycles [*Trenberth et al.*, 2007, 2009], (2) land surface-atmosphere feedback including the surface energy balance determining the partitioning of energy in sensible and latent heat fluxes [*Seneviratne et al.*, 2010], and (3) mesoscale circulations and convection initiation (CI) driven by the interaction of large-scale forcing as well as orography and land surface heterogeneity [e.g., *Sherwood et al.*, 2010; *Wulfmeyer et al.*, 2011]. CI results in the formation and organization of clouds and precipitation in dependence of the forcing mechanisms and the preconvective distribution of T and WV, the latter constrained by the Clausius-Clapeyron equation. All these processes are interwoven in a nonlinear way leading to fascinating but challenging studies of the Earth's weather and climate as a chaotic system.

Observations of WV and T profiles—hereafter, for the sake of brevity called *thermodynamic* (TD) *profiling*—are at the heart of the understanding of these key processes. Furthermore, the knowledge of TD fields is crucial for the improvement of forecasts by means of data assimilation. Generally, it is essential to determine WV and T fields with high resolution simultaneously, particularly in the lower troposphere. WV concentrations vary strongly in space and time due to strongly heterogeneous sources at the surface as well as many dynamic and diabatic processes related to cloud and precipitation processes. In the T field, subtle vertical gradients and inversions occur and control the vertical stability from the surface layer to the tropopause. Orography and heterogeneous surface forcing result in the development of convergence zones and vertical motions, whose thermodynamic properties determine vertical exchange and the strength of convective events. Thus, lower tropospheric TD profiling, beginning at the surface, is needed with both high vertical and horizontal resolutions.

This work provides a review of state-of-the-art and new remote sensing technologies for lower tropospheric TD profiling, which have the potential to resolve vertical structures and the mesoscale variability of TD fields. The current and expected positive contributions of these systems to the understanding of the Earth system are assessed.

The sections in this work are organized to answer the following questions: What insight into key Earth system processes can be gathered from the current TD profiling capabilities? Several examples are presented in section 2 confirming the importance of high-resolution and high-quality TD observations.

What is the status of WV and T observing systems and what are their current resolution, accuracy, and coverage? This question is answered in section 3.

Section 4 deals with the question of what are the key requirements for the next generation TD profiling systems. In our discussion, we distinguish and analyze the needs from the perspective of monitoring, verification and calibration, data assimilation, and process studies. For all these applications, detailed specifications of future observing techniques are developed in order to make significant progress in Earth system science. The results are summarized in a table.

The questions arise as to what are the capabilities of remote sensing methods and what is the most suitable remote sensing methodology to meet these requirements. For this purpose, a comprehensive analysis and comparison of passive and active remote sensing techniques is presented in section 5 including considerations with respect to their synergy.

The key conclusions concerning the design of future ground-based networks of WV and T observing systems are presented in section 6. Several research desiderata are identified, and the scientific approaches to close these gaps are summarized. For easier reading, sections 8 and 9 contain tables of all abbreviations and variables used in this work.

2. The Key Role of Water Vapor and Temperature in the Earth System

2.1. Basic Considerations Concerning Temperature and Water Vapor

Simultaneous temperature and water vapor measurements are of the utmost importance in the study of radiative transfer, vertical stability (which is usually studied through potential temperature θ or equivalent
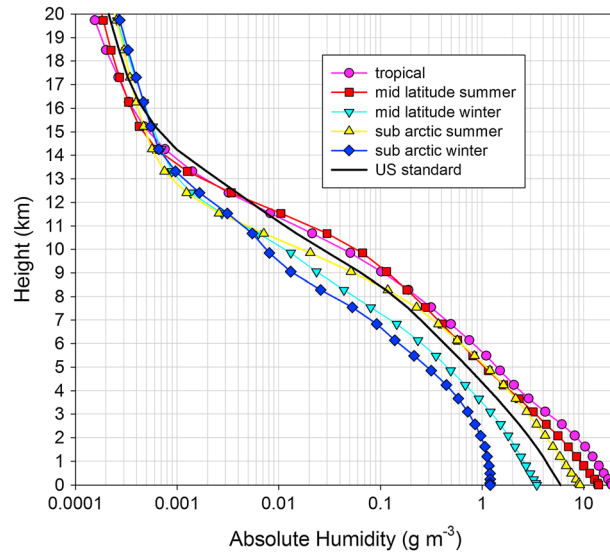
Figure 1. Absolute humidity profiles for the U.S., tropical, midlatitude summer, midlatitude winter, subarctic summer, and subarctic winter atmospheres.

potential temperature), buoyancy, convective available potential energy, convective processes, and the formation of clouds and precipitation. Obviously, it is essential to measure both T and WV profiles with high vertical resolution and accuracy in the lower troposphere so that gradients and temperature inversions as well as WV layers are resolved.

The study of water vapor is particularly challenging, as water is the only atmospheric constituent that exists naturally in all of its three phases. The mean mass of WV contributes to 0.25% of the total mass of the atmosphere [*Trenberth and Smith*, 2005]. However, the combination of the strong absorption of terrestrial radiation by WV due to its hydroxyl bonds and its relatively high number density turns it into the most important greenhouse gas. Under clear-sky conditions, WV contributes ≈60% to the atmospheric greenhouse effect [*Kiehl and Trenberth*, 1997]. The energy released by the condensation of a given mass of WV corresponds to approximately 600 times the energy required to increase its temperature by 1 K and to 2400 times the energy required to increase the temperature of a corresponding mass of air by 1 K [*Wang and Dickinson*, 2012].

Vertical humidity profiles are highly variable in space and time. Figure 1 presents profiles of the absolute humidity ρ_{WV} for a variety of standard atmospheres. Its strong nonlinear behavior is mainly due to the Clausius-Clapeyron equation so that different surface temperatures in the climate regions and the decrease of temperature in the troposphere translate into a strong horizontal and vertical variability of WV. The surface WV amount varies by more than an order of magnitude between tropical and arctic regions. The number density decreases vertically by nearly 5 orders of magnitude, especially in the tropics due to the depth of the troposphere and the corresponding strong decrease in T. Additional variability of the WV profiles is introduced by various phenomena such as evapotranspiration (ET) from the surface, horizontal advection, and diabatic processes such as condensation. Therefore, high-resolution measurements of WV in the lower troposphere are essential to understand and to simulate climate and weather processes.

Many remote sensing systems only retrieve integrated water vapor (IWV) that is the vertically integrated amount of WV throughout a column of the atmosphere in units of $kg\,m^{-2}$. This quantity is related to precipitable water (PW, given in millimeters) by the equation $PW = IWV/\rho_W$, where ρ_W is the density of liquid water. Although IWV measurements do not have information on the vertical variability of WV, they are extensively used for observations of and research on the water cycle. As can be derived from Figure 1, IWV varies from 60–70 mm in the tropics to < 10 mm in polar regions.

2.2. Radiative Transfer As Well As Energy and Water Budgets

Figure 2 presents the most important processes controlled by the vertical distribution of water vapor and temperature in the lower troposphere. The surface fluxes are influenced by soil moisture and temperature, surface roughness, and vegetation as well as the temperature and moisture distribution in the atmospheric boundary layer (ABL). This is the lowest layer of the atmosphere responding rapidly to changes in surface roughness and fluxes [*Stull*, 1988]. The vertical transport of moisture at the top of the ABL is determined by the balance between entrainment and subsidence. The interaction of radiation, heat, temperature, and moisture can be quantified by the budget equation [*Rosen*, 1999]

$$\frac{1}{g} \int_0^{TOA} \frac{\partial}{\partial t} \left(c_p T + L q \right) \, dp + \int_0^{TOA} \vec{\nabla} \cdot \left[\left(\Phi + c_p T + L q \right) \vec{V} \right] dp = F_{TOA} - F_s \tag{1}$$
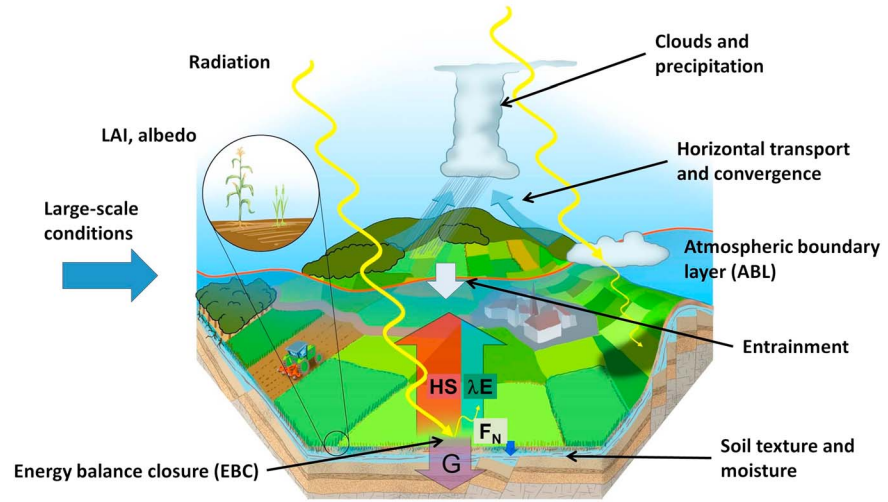
Figure 2. The land system and its feedback processes. The evolution of the ABL and thus CI is critically dependent on the interaction of land surface exchange and entrainment fluxes. F_N: net radiation, HS: sensible heat flux, λE: latent heat flux, G: ground heat flux at the land surface.

where g is the acceleration due to gravity, c_p is the specific heat of dry air at constant pressure p, T is temperature, L is the latent heat of evaporation, q is the specific humidity, and TOA is the top of the atmosphere. The dry static energy is $\Phi + c_p T$, which includes the potential energy Φ of the atmosphere, and $\Phi + c_p T + Lq$ is the moist static energy, which is conserved in the case of negligible kinetic energy of the air mass. The horizontal wind vector is $\vec{V}$, F_{TOA} is the net downward fluxes at the TOA, and F_s is the net downward flux of energy at the surface.

WV and T distributions strongly influence the shortwave and longwave radiative transport, hence, the Earth system energy balance at the TOA and at the land surface [*Lucarini and Ragone*, 2011]. Particularly, the WV profile has a strong impact on the longwave downwelling radiation, which is part of the net surface radiation. The transmission of radiation is described by the radiative transfer equation (RTE) neglecting atmospheric and surface scattering

$$I_v(r) = I_v(0)\exp\{-\tau_v(r,0)\} + \int_0^r B_v[T(r')]\exp\{-\tau_v(r,r')\}\,\alpha_v(r')\,\mathrm{d}r' \tag{2}$$

where $I_v(r)$ is the transmitted radiative power at distance r, v is frequency, and $B_v(T)$ is the Planck function. Depending on the position of the receiver in the RTE problem, the radiation source $I_v(0)$ includes the emission from the Earth's surface as well as the reflected atmospheric emission and extraterrestrial sources. $\tau_v(r,0) = \int_0^r \alpha_v(r')\,\mathrm{d}r'$ is the optical thickness, and $\alpha_v = \sum_i \alpha_{v,i}$ is the extinction coefficient, where the index i stands for the ith constituent in the atmosphere. For instance, for the WV absorption coefficient,

$$\alpha_{\text{WV}} = N_{\text{WV}}\,\sigma_{\text{WV}}(p,T) \tag{3}$$

where N_{WV} is the WV number density and σ_{WV} is the WV absorption cross section, the fundamental quantum mechanical property determining the absorption line strength, which is a function of pressure p and T. The RTE is of fundamental importance for Earth system research. It is the equation used in passive remote sensing of TD profiles, as shown in section 5.1, and it is the basis for the determination of regional and global water and energy budgets. Radiative transfer codes are at the core of every weather, climate, and Earth system model.

Gaps in the knowledge of the representation of radiation transfer physics in clear and cloudy atmospheres in global climate models led to the inauguration of the United States (U.S.) Atmospheric Radiation Measurement Program (ARM, www.arm.gov) [*Stokes and Schwartz*, 1994; *Ackerman and Stokes*, 2003] and various GEWEX projects. This required the development of advanced radiative transfer codes and their

tests by advanced TD profiling. Therefore, in situ and remote sensing techniques for TD profiling were operated, improved, and characterized at the Southern Great Plains (SGP) site in Oklahoma, USA [*Revercomb et al.*, 2003; *Turner et al.*, 2003, 2004; *Ferrare et al.*, 2004, 2006]. In particular, ARM invested heavily to make the WV Raman light detection and ranging (lidar) (WVRL) technique operational. The SGP WVRL made unique contributions to the development of operational and calibrated WV data sets [*Goldsmith et al.*, 1998; *Turner and Goldsmith*, 1999] and improved significantly our understanding of radiative transfer and aerosol processes in the atmosphere (D. D. Turner et al., Development and applications of the ARM Raman lidar, to appear in The Atmospheric Radiation Measurement Program: The First 20 Years, submitted to *Meteorological Monographs, American Meteorological Society*, 2014).

Accurate temperature and humidity profiles are of importance for energy and water budget studies. For example, recent results on the global energy budget, including horizontal transport of energy from ocean to land derived combining global reanalyses such as ERA-40 [*Uppala et al.*, 2005], ERA-Interim [*Dee et al.*, 2011], or satellite measurements [*Kiehl and Trenberth*, 1997; *Trenberth et al.*, 2009; *Stephens et al.*, 2012], show that the determination of radiative fluxes is still rather uncertain. In particular, the TOA outgoing longwave radiation [*Trenberth and Smith*, 2009] and the estimation of surface latent heat and downwelling longwave radiative fluxes are affected by uncertainties in both near-surface temperatures and tropospheric humidity [*Zhang et al.*, 2006]. Furthermore, it was demonstrated that the components of the budget equation *derived* from reanalyses are affected by uncertainty of WV measurements during the assimilation effort [*Bengtsson et al.*, 2004]. The importance of TD profiling for the study of regional and global water cycles is summarized by its governing budget equation [*Oki*, 1999]

$$-\frac{\partial}{\partial t}\,\text{IWV} - \vec{\nabla}_H \cdot \vec{Q} = P - \text{ET} = \frac{\partial S}{\partial t} + \vec{\nabla}_H \cdot \vec{R}_0 \qquad (4)$$

where $\vec{Q}$ is the vertically integrated two-dimensional water vapor flux, P is precipitation, S is water storage in the soil-canopy layer including all phases of water, and $\vec{R}_0$ is surface water runoff. Equations (1) and (4) demonstrate the strong coupling of the water and energy cycles via ET and the TD profiles. The humidity and temperature profiles close to the surface control ET, and the water balance is a function of atmospheric humidity in the first (storage) term and the horizontal water vapor flux divergence.

Similar to global energy budget analyses, several authors found that global- and continental-scale water budgets have large uncertainties because a variety of data sets have to be merged. Particularly, if the water budgets are broken down with respect to oceans or continents, the water vapor flux divergence must be estimated by reanalyses data, which present inconsistencies and sometimes unrealistic values [*Bengtsson et al.*, 2004; *Dee et al.*, 2011; *Trenberth et al.*, 2011]. Similar issues were found in the European Centre for Medium-Range Weather Forecasting (ECMWF) forecast system [*Andersson et al.*, 2005]. If hydrological models are driven by global or regional reanalyses, the uncertainty of the components of the regional water cycles such as ET and runoff increases even further [*Haddeland et al.*, 2011; *Harding et al.*, 2011].

Accurate representation of the water cycle is important for climate modeling as shown by *Schneider et al.* [2010]. Recent research with general circulation models (GCMs) [*Soden and Held*, 2006], observations [*Soden et al.*, 2005; *Dessler et al.*, 2008], or both [*Held and Soden*, 2000] confirmed the existence of a positive WV feedback of 1.5–2 W m^{-2} K^{-1} or at a rate of $\approx$7.5% K^{-1} with respect to surface temperature. This sensitivity is due to a combination of changes in the temperature profile and lapse rate as well as upper tropospheric humidity [*Dessler and Sherwood*, 2009]. GCMs and observations also support the hypothesis that the global average relative humidity will remain approximately constant under climate variability [*Cess*, 2005] permitting a simple assessment of WV climate sensitivity; however, this may not be true for the regional scale. Other studies have predicted increase in surface humidity [*Dai*, 2006], in ET [*Liepert and Previdi*, 2009], and in global PW [*Mieruch et al.*, 2008]. Links between temperature and precipitation extremes have been investigated by *Huntington* [2006], *Alexander et al.* [2006], and *Intergovernmental Panel on Climate Change* [2013, 2014], while *Philipona et al.* [2005] found strong evidence that a considerable part of the temperature increase over Europe during the last decades is due to WV feedback.

Climate sensitivity studies demand more accurate and dense TD data on the regional scale [*Doherty et al.*, 2009]. This becomes even more critical when clouds [*Dessler*, 2010] and precipitation (including its extremes) are included [*Trenberth et al.*, 2003; *Zolina et al.*, 2013], because the effects critically depend on moist adiabatic lapse rates and moisture convergences at the base of convective systems. *Wentz et al.* [2007]

and *O'Gorman and Schneider* [2009] demonstrated that large discrepancies exist between precipitation statistics derived by observations and those simulated by global models.

The need for improving ensemble-based global climate projections such as the Coupled Model Intercomparison Project Phase 5 (CMIP5) was confirmed by *Knutti and Sedláček* [2013]. *Hagemann et al.* [2004] found that regional, dynamical downscaling could provide some benefits that were, however, dependent on the model system and the regions. The most recent ensemble has been provided within the Coordinated Downscaling Experiments (CORDEX) over different regions of the Earth with grid increments of 0.012° [*Giorgi et al.*, 2009]. For example, the performance of regional climate models over Europe has been investigated for 1989–2009 with respect to temperature and precipitation statistics [*Warrach-Sagi et al.*, 2013; *Kotlarski et al.*, 2014] and extreme events [*Vautard et al.*, 2013]. The authors reported the presence of severe biases and a strong intermodel variability in the simulation of temperature and precipitation statistics and identified deficiencies in the simulation of land surface-atmosphere (LSA) feedback and in the convection parameterizations. Although the bias correction is still a debated issue [*Ehret et al.*, 2012], *Warrach-Sagi et al.* [2013] demonstrated that errors in temperature and precipitation statistics can be reduced by simulations on the convection-permitting scale. TD profiling with high accuracy and resolution starting in the lower troposphere and with mesoscale coverage over land and over the oceans could therefore benefit advanced process studies and regional model verification.

2.3. Land Surface-Atmosphere Exchange and Feedback

Figure 2 demonstrates that the soil, the land cover such as vegetation, and the atmosphere must be considered as a coupled *system*. In order to analyze feedbacks in the LSA system, both equations (1) and (4) have to be applied to the ABL. Consequently, the ABL moisture is influenced by the surface energy balance and entrainment fluxes at the ABL top simultaneously. Generally, it is important to study the vertical structure of the ABL during daytime in the unstable surface layer, the mixed layer, and the interfacial (inversion) layer as well as during nighttime in the stable surface layer. Particularly during daytime, the WV flux divergence becomes very important so that both the surface flux $\lambda E = L \overline{w' \rho_{WV}'}_s \propto ET$ and the entrainment flux $\lambda E_{IL} = L \overline{w' \rho_{WV}'}_{IL}$ must be determined. Here w' and ρ_{WV}' are the turbulent vertical wind and absolute humidity fluctuations at the land surface (index s) or in the interfacial layer (index IL). Again, this demonstrates the strong coupling of the energy and water cycles in the lower troposphere and the key role of high-resolution TD profiling.

LSA feedback is the subject of several international projects such as the Global Land/Atmosphere System Study (GLASS) [*van den Hurk et al.*, 2011], the GEWEX Atmospheric Boundary Layer Study (GABLS) [*Holtslag et al.*, 2013], the Diurnal Coupling Experiment (DICE), and the Local Coupling (LoCo) project [*Santanello et al.*, 2009, 2011]. LSA feedback is also subject of the *International Geosphere-Biosphere Program* [2006] and its *Integrated Land Ecosystem-Atmosphere Processes Study* [2005]. A dedicated field campaign for studying LSA feedback was performed in Southern Germany [*Wulfmeyer et al.*, 2014a] with a novel synergy of remote sensing systems, and another campaign is in preparation at the ARM SGP site.

So far, studies of land surface models have mainly relied on surface in situ measurements and radio soundings. The simulation of surface fluxes is based on bulk exchange equations in combination with Monin-Obukhov similarity theory [e.g., *Jiménez et al.*, 2012], which assume locally homogeneous conditions at the land surface. However, recent benchmarking projects comparing the performances of land surface models with respect to ET demonstrated that these are not maximizing the information content in the forcing data [*Best*, 2014]. Furthermore, there are severe deficiencies in the energy balance closure and in the simulation of soil moisture over various crops [*Gayler et al.*, 2013, 2014; *Wöhling et al.*, 2013]. Last but not least, observational and modeling studies indicate the important role of land surface heterogeneity, turbulence, and mesoscale circulations to quantify LSA feedback including cloud formation and precipitation [*Hohenegger et al.*, 2009; *Taylor et al.*, 2012; *Demory et al.*, 2013]. From the modeling perspective, this requires extensive simulations over a hierarchy of model resolutions down to the so-called *grey zone*. This is the grid increment of the order of 1 km where the model starts to resolve convection, mesoscale circulations, and small-scale turbulence so that the assumptions behind turbulence and convection parameterizations are violated [e.g., *Yu and Lee*, 2010; *Ching et al.*, 2014]. Due to the expected advanced forecast skill at this resolution, several grey zone projects have been initiated (e.g., http://hdcp2.zmaw.de) [*Wulfmeyer et al.*, 2014b, 2014c; D. D. Turner et al., submitted manuscript, 2014].

From the observational standpoint, data are needed for studying the energy balance closure and assumptions of Monin-Obukhov theory in complex terrain, entrainment fluxes, and intermittent turbulence at the

top of the ABL as well as the formation of clouds and precipitation, simultaneously. This requires that the TD profiles in the lower troposphere resolve the gradient functions in the stable, neutral, and unstable surface layer as well as gradients and entrainment fluxes at the top of the ABL. Unfortunately, long-term data sets of this kind are entirely missing. Currently, the resolution, the coverage, and the accuracy of operational TD observations is neither sufficient for processes studies nor for model verification. High-resolution TD data over land and the oceans would also be very useful for developing and verifying surface flux databases such as GEWEX SeaFlux and LandFlux, the Water Cycle Multi-mission Observation Strategy (WACMOS) Evapotranspiration (WACMOS-ET) of the European Space Agency (ESA), and the Hamburg Ocean Atmosphere Parameters and Fluxes from Satellite Data (HOAPS) databases [*Andersson et al.*, 2010]. New technologies for addressing these pressing observational needs are emerging. They are based mainly on active remote sensing technologies such as temperature rotational Raman lidar (TRRL) [*Di Girolamo et al.*, 2004a; *Radlach et al.*, 2008; *Newsom et al.*, 2013], WVRL [*Turner et al.*, 2002; *Wulfmeyer et al.*, 2010; *Turner et al.*, 2014b], and water vapor differential absorption lidar (WVDIAL) [*Wulfmeyer*, 1999a, 1999b; *Behrendt et al.*, 2009; *Muppa et al.*, 2015]. Further details are presented in sections 3.2.3 and 5.2.3 as well as in *Wulfmeyer et al.* [2014a, 2014b].

2.4. Mesoscale Circulations and Convection Initiation

Mesoscale circulations and CI can be considered part of the LSA feedback chain leading to the formation of clouds and precipitation. CI is a central topic of weather and climate research, as models are still suffering from limited resolution and insufficient representation of cloud and precipitation processes, particularly in connection with extreme events (see above section 2.2).

Various trigger mechanisms can play an important role depending on the region of interest [*Weisman and Klemp*, 1982; *Stevens*, 2005; *Weckwerth and Parsons*, 2006; *Rotunno and Houze*, 2007; *Browning et al.*, 2007; *Schwitalla et al.*, 2008; *Sherwood et al.*, 2010; *Wulfmeyer et al.*, 2011]. Among them we mention land surface heterogeneity, orographic effects, and their interaction with low-level boundaries and mesoscale convergence zones, which influence low-level moisture, the vertical moisture profile, and the depth of moisture as well as the convergence/updraft strength and depth. Other subtle mechanisms such as vertical wind shear can play an important role in environments that are already close to the onset of convection such as in the tropical Pacific [*LeMone et al.*, 1998; *Lima and Wilson*, 2008]. It has been demonstrated that the exact location and timing of CI are further influenced by small-scale moisture variations caused by colliding boundaries [*Kingsmill*, 1995], small-scale boundary layer organized structures, such as horizontal convective rolls and mesocyclones (convective-scale vortices) [*Weckwerth et al.*, 1996; *Murphey et al.*, 2006], and intersections between boundaries and horizontal convective rolls [*Dailey and Fovell*, 1999]. Convergence zones act to deepen and to enhance the low-level moisture field [*Ziegler and Rasmussen*, 1998; *Weckwerth et al.*, 2005] and to modify the vertical moisture gradient. *Lee et al.* [1991] and *Crook* [1996] demonstrated that the amount of moisture as well as variations of the low-level vertical gradients of moisture and temperature can change the strength of a simulated storm from no CI at all to strong CI. The increase in the intensity of the storm is mainly due to the reduction of static stability with higher low-level moisture content, traditionally characterized by buoyancy, convective available potential energy, and convective inhibition. This sensitivity is crucial for CI and its lifetime under all forcing conditions in midlatitudes [*Wulfmeyer et al.*, 2011] and for CI along the dry line in the central U.S. [*Weckwerth and Parsons*, 2006].

The relationship between the 3-D TD fields and CI, cloud formation, and precipitation has been the subject of a series of field campaigns such as the Mesoscale Alpine Program in high mountains during the 1990s [*Richard et al.*, 2007]; the International H_2O Project in 2002 (IHOP_2002) [*Weckwerth and Parsons*, 2006] focusing on relatively flat terrain in the central U.S. but with strong synoptic gradients such as the dry line, the Convective Storm Initiation Project (CSIP) in maritime environment of southern England in 2005 [*Browning et al.*, 2007], and the Convective and Orographically-induced Precipitation Study (COPS) [*Wulfmeyer et al.*, 2008, 2011] in low mountain regions in Southwestern Germany/Eastern France. The latter was coordinated with the Demonstration of Probabilistic Hydrological and Atmospheric Simulation of flood Events in the Alpine region (D-PHASE) for comparisons and analyses of multimodel ensembles [*Rotach et al.*, 2009].

During all these campaigns, it was envisioned to provide new data sets of the distribution of WV to study their effect on ABL development and CI. However, even applying the new generation of passive and active

remote sensing systems for measuring WV and *T* distributions, the success was limited. This was mainly due to the limited spatial coverage of high-performance TD remote sensing systems, even when combined during field campaigns, and due to constraints with respect to operation times. Obviously, it is necessary to continue and to intensify CI studies using networks of operational TD profilers with very high vertical resolution and accuracy in the lower troposphere over various types of land cover (urban areas and vegetation) and over the oceans combined with a hierarchy of model simulations down to the grey zone.

2.5. Data Assimilation for Reanalyses, Advanced Process Studies, and Forecasting

Data assimilation (DA) is the key methodology for accurate reanalyses, numerical weather prediction (NWP), seasonal forecasting, and parameter estimation. As demonstrated in section 2.2, simulations of the water and energy cycles by means of reanalyses are limited due to a lack of coverage and quality of TD profiling particularly in the lower troposphere [*Dee et al.*, 2011]. Also, short- to medium-range quantitative precipitation forecasting (QPF) is strongly dependent on the initial WV and *T* fields [*Crook*, 1996; *Ducrocq et al.*, 2002; *Richard et al.*, 2007; *Keil et al.*, 2008; *Dierer et al.*, 2009; *Wulfmeyer et al.*, 2011].

Unfortunately, on the mesoscale, the availability of TD profiles (see section 3) is particularly poor so that only a few studies are available yet to support this statement. Currently, mainly surface in situ sensors from surface stations, ships, and buoys complemented by TD profiles from the global radiosonde network are assimilated. Some densification with respect to temperature is provided by aircraft in situ measurements along the tracks of airlines and close to the airports. The radio sounding network has a high vertical resolution; however, its horizontal coverage and the temporal resolution are coarse so that it gives very limited information on mesoscale processes. Spaceborne measurements of TD profiles constitute the backbone of the Global Observing System (GOS) of the World Meteorological Organization (WMO) [*World Meteorological Organization (WMO)*, 2005] and provide vital measurements for global NWP. More than 60% of the forecast skills in terms of short-range global forecast error reduction can be attributed to the TD measurements from operational meteorological satellites [*Joo et al.*, 2013]. Information of TD profiles is primarily acquired in the infrared (IR) and microwave (MW) domains. Observations from National Aeronautics and Space Administration's (NASA) Atmospheric Infrared Sounder (AIRS) on Aqua [*Aumann et al.*, 2003; *Le Marshall et al.*, 2006; *McNally et al.*, 2006] and the operational Infrared Atmospheric Sounding Interferometer (IASI) on the European Organisation for the Exploitation of Meteorological Satellites' (EUMETSAT) Meteorological Operational (MetOp) satellites [*Cayla*, 1993; *Collard and McNally*, 2009; *Guidard et al.*, 2011] as well as the Cross-Track Infrared Sounder (CrIS) onboard Suomi-National Polar-orbiting Partnership (NPP) of the National Oceanic and Atmospheric Administration (NOAA) and NASA [*Han et al.*, 2013] substantially contributed to the increase of forecast skills in global NWP [*Hilton et al.*, 2009, 2012].

For the assimilation into NWP, IR spectra are directly used in combination with RTE observation operators without transferring them into TD profiles by any retrieval methods. The error characteristics of the measured radiance spectra are well understood and can be combined with NWP background knowledge of the atmospheric state. Hence, bias corrections, explaining the systematic differences between measured and calculated radiances, are kept to a minimum. IR soundings are generally limited to cloud-free areas. The averaging kernels of the RTE limit the vertical resolution of *T* and WV information in the lower troposphere to approximately 1 km and 2 km, respectively, mostly smoothing out the details of the stable and convective ABL.

The data of geostationary satellites such as Meteosat and the Geostationary Operational Environmental Satellite (GOES) are also assimilated into NWP. However, their clear-sky radiances are mainly sensitive to upper tropospheric WV [*Köpken et al.*, 2004] and not to WV and *T* in the lower troposphere. This will change with the Meteosat Third Generation (MTG), which will also embark a hyperspectral IR sounder [*Stuhlmann et al.*, 2005].

TD observations in clear and cloudy atmospheres provided by operational MW sounders are also assimilated. These include the Advanced Microwave Sounding Unit-A (AMSU-A) on the MetOp and latest NOAA satellites, the Microwave Humidity Sounders (MHS), and the Advanced Technology Microwave Sounder (ATMS) embarked on the Suomi-NPP satellite [*Kleespies*, 2007], and the Special Sensor Microwave Imager Sounder (SSMIS), flown as part of the U.S. Department of Defense's Meteorological Satellite Program (DMSP). A general complication of assimilating IR and MW data into NWP is the fact that it requires radiative transfer modeling of surface emissivity, which is straight forward over oceans but poses problems over land surfaces, which have spatially and temporally variable emissivity. Therefore, DA is primarily limited to spectral channels that are not strongly influenced by surface contributions.

In the near IR, sensors such as the Moderate Resolution Imaging Spectroradiometer (MODIS) are carried on the NASA's Earth Observing System (EOS) Terra and Aqua satellites and the MEdium Resolution Imaging Spectrometer (MERIS), which is an instrument on ESA's Environmental Satellite (ENVISAT) platform. These instruments provide unique IWV fields over land surfaces, where IR and MW soundings close to the surface are not much exploited. The assimilation of IWV over land, as derived from MERIS showed neutral to positive impact [*Bauer*, 2009].

Another source of signals containing WV and *T* information are the Global Navigation Satellite System (GNSS) Zenith Total Delays (ZTDs), Slant Total Delays (STDs), and radio occultation (RO) bending angle (refractivity) profiles. Particularly, RO data have been successfully applied to global DA [*Cucurull et al.*, 2007; *Healy et al.*, 2007; *Poli et al.*, 2010]. The RO technique provides a unique combination of global coverage, high vertical resolution, high accuracy, and all-weather capability [*Kursinski et al.*, 1997; *Anthes*, 2011]. With a horizontal footprint of only ≈200 km but high vertical resolution of ≈200 m, the forecast improvement using RO data is as large as the one obtained from AIRS or IASI [*Cardinali and Healy*, 2014]. The impact on the WV and *T* fields is strong from the middle to the upper troposphere. This demonstrates that in these regions, RO data close a gap in accurate WV and *T* observations complementing the passive remote sensing retrievals. Due to signal tracking issues, in particular, in the subtropical and tropical lower troposphere, the number of observations decreases and observation errors increase substantially toward the surface. In the early RO missions such as the proof of concept mission Global Positioning System Meteorology (GPS/MET) [*Ware et al.*, 1996], which used closed-loop tracking, less than 50% of the profiles reached below 1 km, especially in the tropics. However, with the development of the improved open-loop tracking [*Sokolovskiy*, 2001] the percentage of profiles reaching 1 km was increased between 60 and 90% [*Anthes et al.*, 2008]. Besides improving the ability to probe deeper into the lower troposphere and ABL [*Sokolovskiy et al.*, 2006], the open-loop tracking also enables the acquisition of rising signals, thereby doubling the RO data from the same instrument [*Ao et al.*, 2009].

ZTD data are available from several ground-based receiver networks. The density of GNSS receivers for DA is extremely heterogeneous. Whereas only a few sensors exist in Africa, Central Asia, and South America, high density has been reached over the U.S., Europe, and Japan. For instance, near real-time measurements are available from the European Meteorological Network (EUMETNET) GNSS Water Vapor Program (E-GVAP). Numerous impact studies have shown that the usage of ZTD data improves the skill of limited area weather forecast models [e.g., *Kuo et al.*, 1993; *Gutman et al.*, 2004; *Nakamura et al.*, 2004; *Guerova et al.*, 2006; *Zus et al.*, 2008; *Schwitalla et al.*, 2011]. As ZTD data are available in near real time over Europe, they are assimilated operationally at several NWP centers in their regional and global NWP models, e.g., at Météo-France [*Poli et al.*, 2007] and the United Kingdom (UK) Met Office (UKMO) [*Bennitt and Jupp*, 2012].

In principle, higher impact can be expected by DA of STDs, as low-level slants contain information about the spatial heterogeneity of the WV content in the ABL. A study using three-dimensional variational analysis (3-DVAR) and the HIgh Resolution Limited Area model (HIRLAM) simulating hypothetical GNSS receivers indicated a positive impact on the WV analysis [*Jarvinen et al.*, 2007]. Other studies utilizing ZTD and STD data from a station network in Germany demonstrated a small positive impact on the WV field [*Zus et al.*, 2008, 2011]. The benefit of STDs on top of ZTDs, however, was hardly demonstrated, probably due to limitations of the elevation angle to ≈20° [*Bauer et al.*, 2011]. A stronger impact is expected as soon as low-elevation observations down to a few degrees are included, as such observations capture the local asymmetry of the WV field. Further studies are ongoing such as the implementation of a rapid and precise forward (adjoint) operator in the Weather Research and Forecasting (WRF) model system. A promising candidate for such operator was recently suggested [*Zus et al.*, 2014]. Another demonstration of the potential of STD using a 4-DVAR over Japan has been presented in *Kawabata et al.* [2013]. Another option could be the use of GNSS tomography for deriving 3-D WV density fields; however, this has not been explored in detail yet for operational purposes and assimilation in NWP models.

With respect to ground-based passive remote sensing using either MW radiometers (MWRs) or IR spectrometers, we found only one early study [*Kuo et al.*, 1993] where MWR-derived IWV was assimilated in the mesoscale model 4 (MM4). In fact, the MWR network was simulated by radio soundings, which were used to derive IWV. In any case, a positive impact on the WV field was found. Recently, new interest in the assimilation of MW data aroused by the availability of new MWR networks such as MWRnet (http://cetemps.aquila.infn.it/mwrnet). In *Cimini et al.* [2014], a DA experiment was performed showing at least neutral impact on short-range forecasts.
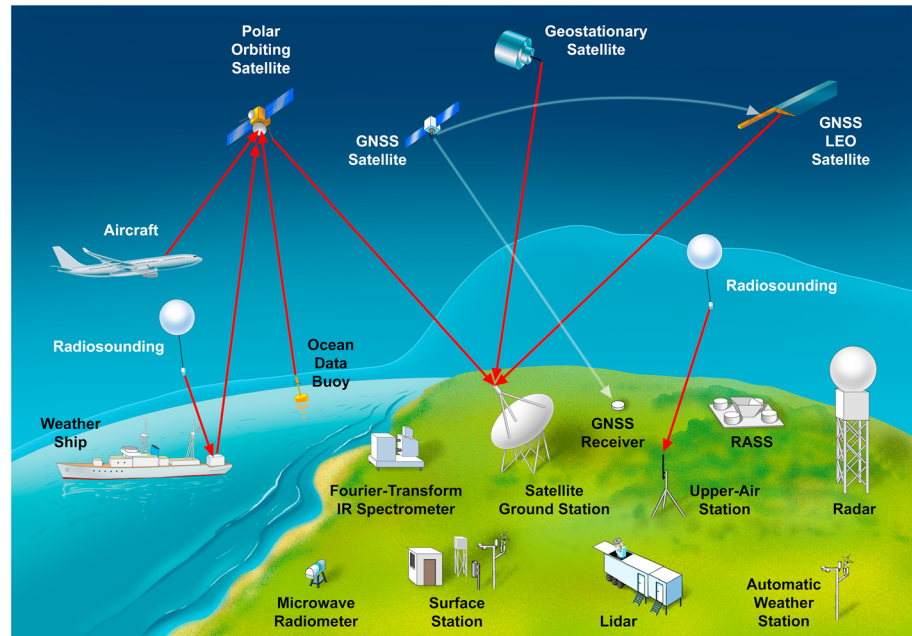
Figure 3. The Global Observing System (GOS) showing the synergy of in situ, passive, and active remote sensing systems for TD measurements. The shading of the atmosphere above the surface indicated the depth of the ABL over the ocean and over the land.

Other studies utilized ground-based or airborne active remote sensing systems such as WVRL or WVDIAL. The first WV lidar DA study was based on the airborne NASA Lidar Atmospheric Sensing Experiment (LASE) instrument utilizing data from the Convection and Moisture Experiment (CAMEX)-4 campaign. The data were assimilated in the Florida State University (FSU) global spectral model using a 3-DVAR. A strong positive impact on initial WV fields, hurricane track and intensity, and QPF was demonstrated [*Kamineni et al.*, 2003, 2006]. Using the MM5 model, the first mesoscale 4-DVAR using WV lidar data was performed during the IHOP_2002 campaign and utilized WVDIAL data from the airborne NASA LASE system as well [*Wulfmeyer et al.*, 2006]. A strong positive impact of CI and QPF was demonstrated. Based on the MM5 model, the first 4-DVAR assimilating a triangle of ground-based WVRLs was performed by *Grzeschik et al.* [2008]. By comparisons with ground-based GNSS sensors, a significant correction of the vertical structure of the WV field was found, which was maintained in the forecast system up to 12 h. A positive impact was also demonstrated by the assimilation of the German Aerospace Agency (DLR) airborne WVDIAL in the ECMWF model [*Harnisch et al.*, 2011]. The most recent impact study was performed during the COPS campaign. Airborne measurements of both the DLR WVDIAL and the CNRS airborne LEANDREII WVDIAL were assimilated using 3-DVAR in the AROME model [*Bielli et al.*, 2012]. A positive and significant impact was found for 6 h precipitation with an improvement lasting up to 24 h. Furthermore, the first DA of TRRL showed a strong positive impact on the vertical temperature profiles including a correction of inversion strength and ABL depth [*Adam et al.*, 2015].

These studies confirm a significant positive impact of WV and T active remote sensing on short-range forecasting based on case studies. A larger positive impact by the simultaneous assimilation of operational TD profiling is expected, if corresponding networks become available with sufficient density and coverage both over land and the oceans. This was illustrated by an Observing System Simulation Experiment (OSSE) over land where various networks of ground-based remote sensing systems were simulated and their forecast impact was assessed [*Otkin et al.*, 2011; *Hartung et al.*, 2011].

3. The State of Observing Systems

The development and maintenance of global, consistent data sets containing variables of the energy and water cycle is an ongoing effort. The backbone for providing operational observations is the WMO GOS (see Figure 3). It consists of a coordinated network for acquiring meteorological and other environmental observations

on a global scale in support of all WMO programs (http://www.wmo.int). The GOS components include surface, upper air, marine, radio detection and ranging (radar), airborne, and satellite observations as well as other observation platforms. This operational network is mostly maintained by National Meteorological Services (NMSs) as well as national and international organizations such as EUMETSAT and NOAA. Another operational setup comprising satellite observations is the space component of the European Union (EU) Copernicus program, which is dedicated to the global monitoring of the environment and implemented by ESA through the Sentinel series of satellites. The operational programs are complemented by dedicated experiments including experimental satellites. The latter comprise spaceborne measurement platforms such as the NASA satellites Terra, Aqua, and Aura.

Data from the GOS and the experimental setups are heavily used within the Global Energy and Water Exchanges (GEWEX) Data and Assessment Panel (GDAP) and various other teams such as the WMO Network for Sustained and Coordinated Processing of Environmental Satellite Data for Climate Monitoring (SCOPE-CM), the EUMETSAT Network of Satellite Application Facilities (SAF), the Global Climate Observing System (GCOS), the Committee on Earth Observations Satellites (CEOS), and NOAA's National Climatic Data Center (NCDC). Another organization dealing with the observation of all components of the Earth system is the Group on Earth Observations (GEO), which is responsible for the coordination of international activities to set up a Global Earth Observation System of Systems (GEOSS). Relatively new data sets were generated within the Global Water Vapor Project (GVaP) providing monthly IWV fields over the globe by blending in situ radio soundings with passive remote sensing data [*Randel et al.*, 1996]. Other WV data sets are available via the EUMETSAT Climate Monitoring-SAF (CM-SAF) [*Schulz et al.*, 2009] and recently within the WACMOS [*Su et al.*, 2014].

In the following, the status of spaceborne and ground-based observations of TD profiles is reviewed with respect to in situ and remote sensing measurements. We do not consider airborne measurements, as they are limited to flight routes and field campaigns so that it is not possible to derive long-term time series of vertical profiles in specific regions from these. In contrast to section 2.5 where it was demonstrated that mainly radiances are used for the assimilation of passive remote sensing data, we are focusing here on the current capability of passive and active remote sensing systems to retrieve or to derive TD profiles in the lower troposphere.

3.1. Spaceborne Measurements

Spaceborne passive remote TD measurements are mainly performed in the near-IR, IR, and MW spectral regions. Retrievals are either based on WV absorption or on the atmospheric emission in absorption bands influenced by WV and T. The methodologies are presented in detail in section 5.1. The only active remote sensing system in space dedicated to TD measurements is GPS RO, which can be used either to derive WV and T via links between low Earth orbit (LEO) satellites or STDs and ZTDs from ground-based receivers. In contrast to lidar and radar techniques, GNSS signals are measured in transmission. Thus, the RO signals provide TD properties along the raypath with high vertical resolution. However, the horizontal footprint is relatively coarse (a few hundreds of kilometers), which results in a horizontal smearing of the signal. The GNSS methodology is presented in detail in section 5.2.2.

3.1.1. Passive Remote Sensing

We distinguish between polar orbiting and geostationary satellites and analyze the retrievals of WV and T profiles with respect to the platforms on which they are operated. This is due to the fact that IR and MW retrievals are complementary in the same observed atmospheric volume so that the performance of the resulting products depends critically on the available combinations of IR and MW channels on the same platform.

With respect to polar orbiting satellites, global operational observations of WV and T fields became possible with the launch of the Television Infrared Observational Satellite program (TIROS)-N/NOAA satellites in 1978 carrying the High-Resolution Infrared Radiation Sounder (HIRS) (T and WV) and the Microwave Sounding Unit (MSU, T only) instruments that provided about 7.5×10^5 and 3.7×10^4 soundings per day, respectively. Advanced microwave sounders, the AMSU-A and MHS instruments, replaced the MSU and are now also providing humidity soundings with a higher density at spatial sampling capabilities of 3.2×10^5 and 2.6×10^6 soundings per day, respectively.

The NOAA satellites were complemented in 1987 by the DMSP satellites, carrying the Special Sensor Microwave (SSM/I, SSM/T, and SSM/T2) sensors, which were later replaced in 2003 by a single radiometer, the SSMIS on follow-up DMSP satellites with $\approx 10^4$ observations over 6 h achieving global coverage within a few days. Another new instrument is the ATMS on the Suomi-NPP satellite, combining the AMSU-A and MHS capabilities.

Depending on frequency, the MW sounders sample the atmosphere at nadir with footprints having diameters of 16 km at higher frequencies to 75 km at lower frequencies. With increasing scan angle of these cross-track sounders, the footprint size increases. Another class of MW instruments consists of conically scanning ones, which offer imaging capability under constant viewing angles. These include the SSMIS and the Global Precipitation Mission's (GPM) Microwave Imager (GMI). The latter is a pure imager without sounding capability, measuring only total columnar WV.

WV and T retrieval techniques were developed, which are applicable even in the presence of nonprecipitating clouds extending the coverage of observations over the oceans. However, retrievals over the land surface remain very difficult due to a large dependence of the surface emissivity on soil moisture and vegetation. Observations made in the MW and the few channels available result in a coarse vertical resolution of WV and T profiles of a few kilometers and an accuracy of 10–20% [*Huang et al.*, 1992]. Information on lower tropospheric TD profiles is at best some bulk estimation of ABL water vapor content [*Schulz et al.*, 1993].

Examples of near-IR remote sensors are the MODIS and the MERIS instruments. The first MODIS instrument was launched on the Terra satellite in December 1999, and the second was launched on Aqua in May 2002. MERIS was operated on ENVISAT from March 2002 to April 2012. As demonstrated in *Gao and Kaufman* [2003] for MODIS, and in *Bennartz and Fischer* [2001] for MERIS, it is possible to derived IWV with high horizontal resolution using the ratio of two channels with different sensitivities to WV absorption around 940 nm and measuring the WV extinction. No vertically resolved information concerning lower tropospheric TD is available. However, their combination with IR and MW passive remote sensing systems can improve the representation of small-scale horizontal variability of the WV field.

Observations of optical imagers such as MODIS and MERIS provide information on lower tropospheric WV mostly in the near-IR spectral region. Using their channels influenced by the broad WV absorption band around 940 nm, it is possible to derive IWV with high horizontal resolution over land surface [*Gao and Kaufman*, 2003; *Bennartz and Fischer*, 2001]. Unfortunately, MERIS data are no longer available since communication to ENVISAT was lost in April 2012. However, its successor, the Ocean and Land Colour Imager (OLCI) will be flown as an operational mission on the Sentinel-3 satellite series from 2015 onward [*Donlon et al.*, 2012].

A considerable advance was achieved by combining MW and IR remote sensing sounders, e.g., the sounding system flying on board of the NOAA Polar Orbiting Environmental Satellite (POES) series. However, *Chédin et al.* [1993] and *Stephens* [1994] recognized that WV and T retrievals from this combination of instruments still do not reach the required level of accuracy needed for a future climate monitoring system.

This motivated the development of more sophisticated IR and MW sounding systems with optimized choice of spectral regions and resolutions with respect to TD profiling. This effort culminated in the launch of the MetOp platforms of EUMETSAT, NASA's Aqua and Terra satellites, and on the Global Change Observation Mission-Water SHIZUKU (GCOM-W) of the Japan Aerospace Exploration Agency (JAXA). The payload of interest for TD profiling consists of AMSU-A, MHS, the Advanced Very-High Resolution Radiometer (AVHRR/3), and HIRS/4 complemented by IASI [*Hilton et al.*, 2012]. The IASI is an IR Fourier transform spectrometer (FTIR) with a spectral sampling of 0.25 cm^{-1}. A footprint size of 12 km at nadir allows a good sampling in clear and partly cloudy areas. The horizontal resolution of the retrievals is ≈25 km collecting about 80,000 measurements within 6 h. In a global constellation with three operational satellites, it takes about 4 h to get global coverage. The vertical resolution of the retrievals is driven by the width of the averaging kernels in the RTE, the spectral resolution, and the radiometric noise. In the case of IR WV retrievals, this results in a vertical resolution of 2 km with an accuracy of 10% in the middle to the upper troposphere and 2 km and 20% in the lower troposphere, respectively [*Pougatchev et al.*, 2009]. The resolution of T profiles is somewhat higher (1 km), and the accuracy is ≈1 K in the middle and upper troposphere degrading to 2 km and ≈2 K in the lower troposphere [*Li et al.*, 2000; *Amato and Serio*, 2000; *Pougatchev et al.*, 2009; *August et al.*, 2012]. This accuracy and resolution has been confirmed by retrievals over complex terrain during the COPS campaign [*Masiello et al.*, 2013].

A similar suite of sensors is flown on the Terra and Aqua satellites, namely, the Advanced Microwave Scanning Radiometer–EOS (AMSR-E), AMSU-A, the Humidity Sounder for Brazil (HSB), and MODIS combined with AIRS. The AIRS uses a grating spectrometer with a spectral resolution of 0.85 cm^{-1}. Due to the similarity of the instruments, the coverage, horizontal resolution, and accuracy as well as the vertical resolution of the WV and T retrievals are similar. The coverage of the IR measurements is mainly limited by the presence of clouds where soundings are possible only down to the respective cloud top. The accuracy close to the land

surface was previously degraded by a larger uncertainty in surface emissivity. However, this has been substantially improved by the possibility to simultaneously derive surface emissivity from the same hyperspectral measurements [*Zhou et al.*, 2011; *Capelle et al.*, 2012].

Zhou et al. [2003] show that an error of 0.1 in surface emissivity can lead to an error in the retrieved near-surface temperature profile of 0.8 K. Particularly, in arid and semiarid regions the surface emissivity varies by about 0.2 and 0.12 at wavelengths of 4 and 9 μm, respectively, while the simultaneous retrieval of temperature profiles and surface emissivities reduces the uncertainty of the latter to 0.045 and 0.02 at 4 and 9 μm, respectively [*Capelle et al.*, 2012], so that the corresponding error in the low-level temperature profile can be reduced by at least 0.8 K. Similarly, *Seemann et al.* [2008] show that the use of a retrieved surface emissivity instead of a commonly assumed constant value of 0.95 in the columnar WV retrieval reduced the retrieval error by more than 40%.

In the MW, the vertical resolution is poor; however, retrievals are possible in the presence of nonprecipitating clouds. The repeatability of the measurements from polar orbiting satellites depends on the number and phasing of available satellites and the geographic region of interest. Three operational satellites with local overpass times separated by 4 h allow for observing some developing phenomena and start to resolve the diurnal cycle. Due to strong overlap of observation swaths the atmosphere at higher latitudes (>60°) is covered at shorter time intervals, so that polar orbiters start to support nowcasting applications where no geostationary satellite measurements are available. However, most critical processes such as CI require a time resolution of 10–15 min and observations used for nowcasting with a forecast range of 0–6 h require an update cycle with much higher resolution than this range.

Therefore, geostationary satellites such as the GOES 11 and 12 operated by NOAA, Meteosat Second Generation (MSG) operated by EUMETSAT, and Himawari by JAXA provide an essential complement of polar orbiting platforms. Passive remote sensors on these platforms are, e.g., the Spinning Enhanced Visible and Infrared Imager (SEVIRI), which observes the Earth in 12 channels from the visible to the IR and the GOES imager and IR sounder. Typically, the time resolution of the observation of the Earth's disk is 15 min and the spatial resolution of the pixels is a few kilometers. These observations are very interesting for monitoring, DA for NWP, and nowcasting. However, the low spectral resolution of their channels does not permit retrievals with high vertical resolution because its channels dedicated to WV are mainly sensitive to upper tropospheric humidity. Microwave remote sensing from geostationary orbit is not currently performed, as the antenna would have to be extremely large in order to have reasonable temporal integration time.

An attempt to combine the information content of different satellites is the WACMOS project [*Su et al.*, 2014]. For instance, combining SEVIRI and IASI, WV fields will be provided for three vertical layers from 200 to 500 hPa, 500 to 850 hPa, and 850 hPa to surface with a horizontal resolution of 25 km. A SEVIRI + MERIS product will contain IWV for the Elbe/Oder basin with a resolution of ≈3 km for the time period between June and November 2008. For both data sets, a temporal resolution of 3 h is envisioned.

Upcoming new data sets with higher accuracy and resolution will certainly improve our understanding of the regional water and energy cycles. However, it should be mentioned that the current and likely the future generation of IR passive remote sensing systems might approach their theoretical limits with respect to vertical resolution in the lower troposphere. For example, the next geostationary platforms such as MTG will contain scanning spectrometers, which have similar properties as IASI or AIRS. An enhancement of the spectral resolution and the reduction of radiometric noise are also planned for the next generation of polar orbiting satellites. Consequently, some improvement of vertical resolution and accuracy can be expected, particularly for the IR temperature sounding in the lower troposphere [*Crevoisier et al.*, 2014], the WV observation in the blue spectral range [*Wagner et al.*, 2013b], and finally, the hyperspectral MW sounding that will allow higher vertical resolution by new technology developments [*Blackwell et al.*, 2011].

For the future generation of IR sounding (IASI-NG), *Crevoisier et al.* [2014] estimate from information content studies that the relative gain of the future instrument providing doubled spectral and doubled radiometric resolution compared to the currently flying IASI instrument will increase from about 10% to >20% in the *T* sounding of the ABL, where the relative gain in precision is expressed as the difference between a priori and a posteriori error, divided by the a priori error. Contrary, the relative gain in WV soundings is limited to the middle and upper troposphere, no improvement in WV retrieval can be obtained in the ABL, for reasons described below (section 5.1). WV soundings in the blue spectral range will benefit from generally higher

surface reflectivity, especially over water surfaces, in this spectral range compared to the red part and therefore will provide more sensitivity to the near-surface layers of the atmosphere. This technique is in a state of demonstrating feasibility, and no firm quantitative error estimates are available yet. The same is true for the use of hyperspectral MW soundings for T and WV, targeting in a tenfold spectral resolution compared to currently flying instruments. Initial information content studies (Aires, conference communication 2014) indicate that $> 20\%$ improvement can be achieved for T and $> 35\%$ for WV in the ABL. However, despite these advances, it will hardly be possible to resolve the structure and the gradients of WV and T in the lower troposphere leaving still significant observational gaps for weather and climate research.

3.1.2. Active Remote Sensing

3.1.2.1. Global Navigation Satellite System

Currently, the only active remote sensing system for WV and T measurements in space is GNSS. Based on the RO technique, bending angle (refractivity) profiles are derived that are sensitive to WV and T. Following GPS/MET, a number of satellites were equipped with GPS receivers, such as the Scientific Application Satellite-C (SAC-C), the Challenging Mini-satellite Payload (CHAMP), the six Constellation Observing System for Meteorology, Ionosphere, and Climate (COSMIC) [*Anthes et al.*, 2008], the Gravity Recovery and Climate Experiment (GRACE) [*Wickert et al.*, 2009], the MetOp-A and MetOp-B, the Terra Synthetic Aperture Radar (SAR)-X, and the TerraSAR-X-Add-on for Digital Elevation Measurements (TanDEM-X) satellites. Currently, around 3500 RO soundings are available per day. However, not all profiles reach Earth's surface due to signal tracking issues. Furthermore, as the RO bending angle (refractivity) depend both on WV and T, their contributions must be disentangled, which is possible only with additional information from another measurement or a numerical weather model.

#### 3.1.2.2. Other Potential Active Remote Sensing Techniques

Possible future solutions for providing TD profiles down to the lower troposphere are the operation of active remote sensing systems such as lidar on polar orbiting satellites. For this purpose, the WAter vapour Lidar Experiment in Space (WALES) mission was proposed in 2000 [*European Space Agency (ESA)*, 2001, 2004]. Its great potential was presented in *Gérard et al.* [2004]. *Wulfmeyer et al.* [2005] demonstrated that a corresponding mission would considerably increase the coverage, resolution, and accuracy of water vapor profiling even in comparison to IASI. Furthermore, the high vertical resolution and accuracy of spaceborne WVDIAL was confirmed by analyzing and extrapolating aircraft WVDIAL measurements to space [*Di Girolamo et al.*, 2008]. *Di Girolamo et al.* [2006] even demonstrated that temperature profiling from space is possible with rotational Raman lidar (TRRL), as well as relative humidity in combination with WVDIAL. Unfortunately, these concepts are still at their infancies, and extensive technological and methodological advances are still necessary until the operation of WVDIAL in space becomes reality.

3.2. Ground-Based Measurements

3.2.1. In Situ Measurements

In situ networks or surface measurements and soundings still provide the backbone of the development of global data sets for the determination of climatologies and initial fields for weather forecasting. Still to date, radiosondes are almost the only instruments measuring WV and T profiles with sufficient resolution to resolve the structure of the ABL including the surface layer, the mixed, and the interfacial layers at the ABL top.

The coverage of surface observations and sounding locations, however, is extremely inhomogeneous and coarse. One of the regions with highest density of observations is Central Europe. Figure 4 presents the current location of stations, which are considered in the WMO Global Telecommunication System (GTS). It is obvious that the density of the surface and sounding stations does not allow for resolving the mesoscale variability of WV and T. The data gaps are particularly large over the oceans. It is still an ongoing effort to densify surface observations with meteorological sensors that are not yet included in the GTS often operated by nonmeteorological agencies and organizations. A pivotal model was the collection of the Joint D-PHASE-COPS data set over Europe during 2007, which probably still represents the densest surface data set in that region [*Wulfmeyer et al.*, 2011]. Consequently, the situation of radio soundings is quasi inverted in comparison to spaceborne passive remote sensing. Whereas the spatial coverage of radiosonde stations is poor, their vertical resolution and accuracy is high; the coverage of spaceborne passive remote observations is high; however, the vertical resolution is poor and the accuracy is limited. It would be necessary to increase considerably the density of the radiosonde network and the frequency of launches in order to get insight into the mesoscale variability of the regional water cycle and to increase the
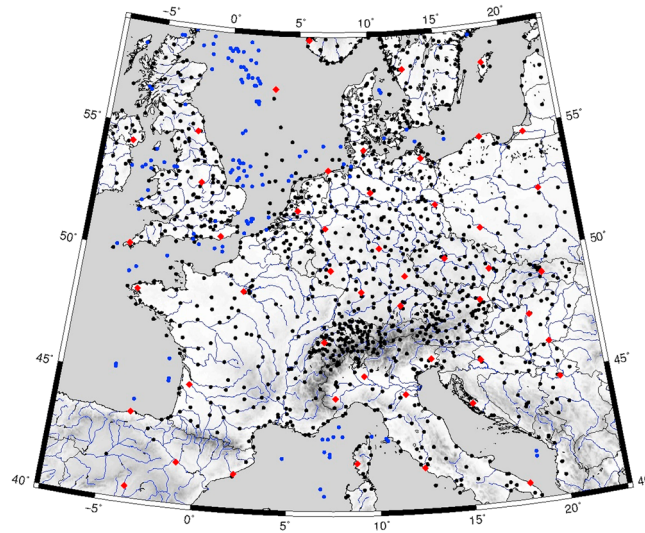
Figure 4. European in situ surface and TD profiling network. Black circles: Surface synoptic stations of the weather services and meteorological stations at airports over Europe, blue circles: shipborne WV and *T* measurements, and red diamonds: radiosonde stations.

representativeness of the sounding of WV and *T* on this scale. This is considered not feasible due to resource limitations.

3.2.2. Passive Remote Sensing

Data gaps can be reduced with networks of operational passive remote sensing of TD profiles using IR spectrometers or MWRs. Several ground-based FTIRs [*Feltz et al.*, 2003; *Knuteson et al.*, 2004a, 2004b] and MWR networks [*Cadeddu et al.*, 2013] are already operating within the ARM. Also, in Europe networks of MWRs are operated [e.g., *Crewell et al.*, 2004], which are currently being combined in a global network of passive remote sensing systems called MWRnet [*Cimini et al.*, 2012]. The operation of FTIRs and MWRs is also possible on shipborne platforms, as demonstrated, for example, during various campaigns of the ARM.

However, the density of these observations is still lower than that achieved with radio soundings. Figure 5 shows an overview of current network of passive and active TD profilers. It becomes clear that not only this network but also all others (discussed below in section 3.2.3) are far from being capable of resolving any mesoscale features over land and over the oceans.

The methodology, the potential, and the limitations of passive remote sensing are presented in section 5.1. The temporal resolution of a retrieval is typically 5–10 min in order to reduce noise errors in the determination of the radiances in different MW channels or in the IR spectra [*Smith et al.*, 1999; *Feltz et al.*, 2003]. The systematic and root-mean-square (RMS) errors, which remain in the retrievals of TD profiles, depend on the radiometric and spectral calibration of the instrument, the radiative transfer model chosen, the inversion method, the atmospheric conditions, and whether the observations are made in the IR or the MW.
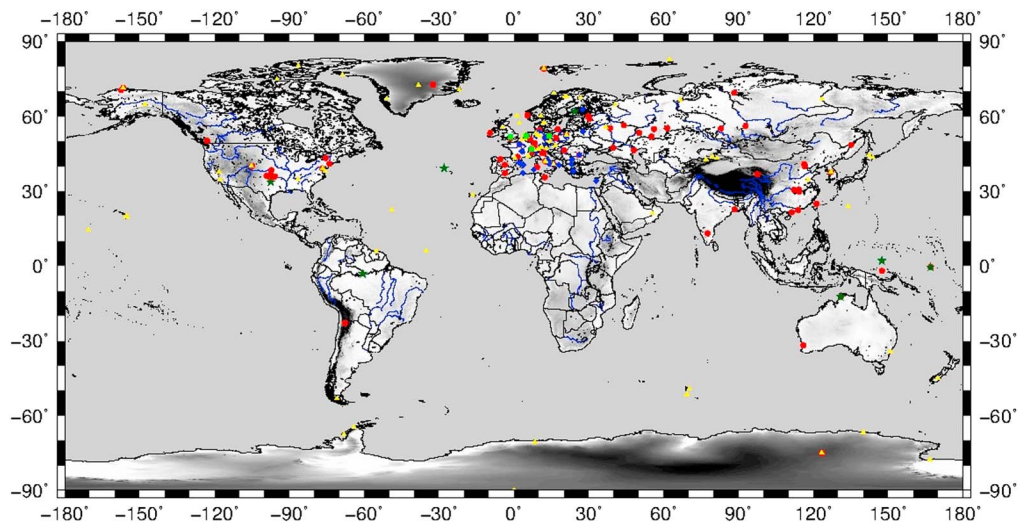
Figure 5. Global network of passive and active TD profilers. Red circles: MWRs, blue diamonds: EARLINET stations with potential WV and *T* profiling capabilities, green squares: WV and *T* lidar systems at observatories, yellow triangles: NDACC profiler stations, and dark green stars: ARM sites.

Generally, the resolution is better close to the surface and degrades to the middle troposphere. For IR retrievals, the resolution of T and WV profiling is $\approx$100 m near the surface to roughly 800 m at 2 km, which often corresponds to the ABL top. For retrievals in the MW, the resolution for T is $\approx$300 m at the surface rapidly decreasing to $\approx$1 km at the ABL top. The use of scanning can improve the resolution to 100 m close to the surface. For WV retrievals, the resolutions are a few 100 m close to the surface to 2 km at the ABL top, respectively. Due to the limited vertical resolution, the fine structure and the gradients of WV and T profiles will be smoothed in the surface layer, the interfacial layer, and the free troposphere. While MWRs are able to penetrate clouds, RMS errors of IR retrievals increase in the presence of clouds but retrievals are now possible as well up to the cloud base [*Turner and Löhnert*, 2014]. Therefore, for optimized TD profiling, it is reasonable to use a synergy of MWRs and IR spectrometers.

Depending on the application, the stability and reliability of operational passive remote sensing systems on different platforms including ships [e.g., *Westwater et al.*, 2003] make these a very interesting option to close the huge temporal and spatial gaps in ground-based networks for TD profiling.

3.2.3. Active Remote Sensing

In contrast to passive remote sensing, active remote sensing systems transmit radiation, which can either be analyzed with respect to their transmitted, bended, phase shifted, or backscattered signals. Active remote sensing systems using transmission, bending, and phase shifts are GNSS and differential optical absorption spectroscopy (DOAS). Whereas active DOAS can provide interesting integrated information about atmospheric T, WV, and other trace gases, we are not aware of these systems being used operationally so that we refer the reader to the literature here [*Platt*, 1994] and focus in the following on GNSS. Examples of active remote sensing systems using backscatter signals are radar and lidar. The immediate advantage of this technology is the intrinsic and high range resolution of the backscatter signals achieved by a time-of-flight measurement.

Active remote sensing systems have the potential to significantly improve accuracy and resolution of TD profiles. These techniques are scalable so that the signal-to-noise ratio (SNR) of the signals can be improved by increasing transmitter power and receiver efficiency. However, until recently, active remote sensing systems played a minor role in global TD observations. This situation changed during the 1990s when techniques like GNSS, radar, and lidar started to show the potential for long-term and reliable WV and T measurements.

3.2.3.1. Global Navigation Satellite System

During recent years, the coverage of ground-based GNSS receivers has been considerably increased. Furthermore, algorithms for deriving ZTD and STD have been developed and improved. Networks of GNSS receivers with harmonized retrieval algorithms are operated in Europe such as E-GVAP and in the U.S. Details of GNSS methodology are presented in section 5.2.2.

When GNSS signals are received by a ground-based station, it is, in general, not possible to derive a refractivity profile or separate TD profiles. However, the estimated ZTD, which represents the integrated refractivity above the station, is closely linked to IWV. For this reason ZTD data are becoming increasingly useful for weather and climate research [*Wickert and Gendt*, 2006]. The tropospheric WV estimates retrieved from GNSS postprocessed data are used not only for the analysis of meteorologically significant events [*Bock et al.*, 2004; *Walpersdorf et al.*, 2004; *Brenot et al.*, 2006; *Van Baelen et al.*, 2011; *Labbouz et al.*, 2013] and for process-oriented studies [*Adams et al.*, 2013] but also for the evaluation of long time series with an homogeneous analysis scheme in the framework of climate studies [*Wang et al.*, 2007; *Sguerso et al.*, 2013]. Higher resolution observations of the WV distribution in the lower troposphere may be realized using STDs. When the available network of ground-based GNSS stations is sufficiently dense for the line-of-sight tropospheric delays to interleave in the atmospheric volume above the network, tomographic inversion enables the retrieval of the 3-D water vapor distribution. This method has the potential to provide a WV field with reasonable space and time resolution: several kilometers horizontally, a few hundreds of meters vertically and better than 15 min. However, it is highly dependent upon the network density and geometry. Several campaigns have shown good comparisons of the retrieved water vapor field with other type of measurements and numerical model outputs but also demonstrated the usefulness of GNSS tomography to study atmospheric situations in ties with CI and heavy precipitation events in the Tropics [*Flores et al.*, 2000], in the Mediterranean [*Champollion et al.*, 2005; *Bastin et al.*, 2005; *Brenot et al.*, 2014], in the Alps [*Troller et al.*, 2006; *Perler et al.*, 2011], the great plains in the U.S. [*Champollion et al.*, 2009], low mountain ranges within COPS [*Van Baelen et al.*, 2011; *Labbouz et al.*, 2013; *Weckwerth et al.*, 2014], and in south America [*Adams et al.*, 2011, 2013]. Recently, the estimation of precipitable water

vapor from shipborne GPS measurements was also demonstrated [*Rocken et al.*, 2005; *Fujita et al.*, 2008]. Its potential to study the prediction of intense weather events was analyzed in *Boniface et al.* [2012]. For operational applications, the current networks deployed in numerous countries in Europe are too sparse with mean distance between stations of about 50 km; however, with the ever-increasing number of stations and the advent of new GNSS constellations such as GLONASS and Galileo, tomography could hold some promises for the future.

3.2.3.2. Radar Techniques

Weather radar signals do not contain much information about WV and *T* contents. However, a technique has been developed to retrieve 2-D surface maps of refractivity [*Fabry et al.*, 1997] using the time evolution of the phase information from ground targets as an indication of small perturbations in the refractive index caused by changes in the humidity, temperature, and pressure fields. Using hard-target returns in suitable environment with small orography, it is possible to produce these maps with a resolution of 15 min and a range of 50 km [*Weckwerth et al.*, 2005; *Roberts et al.*, 2008]. However, measurements in the vertical are not possible and unknown heights of the radar cone above the terrain can produce significant deviations from surface measurements [*Bodine et al.*, 2011]. Therefore, this technique can mainly be seen as an approach for closing gaps between ground-based in situ sensors but not for deriving TD profiles. Other radar techniques are in the research stage and are briefly introduced in section 5.2.1.

Another approach at TD profiling with radars has been investigated with wind profilers using the radio acoustic sounding system (RASS) for temperature [*Peters et al.*, 1983] and refractivity index gradients profiles for humidity [*Tsuda et al.*, 2001]. However, whereas RASS temperature data are now available in networks (see, e.g., madisdata.noaa.gov/cap/profiler.jsp), several limitations of the humidity retrieval technique in terms of vertical coverage, physical assumptions, and need of other supporting measurements have been a major hurdle for any operational use. Further details are provided in section 5.2.1.

3.2.3.3. Lidar Techniques: Temperature Rotational Raman Lidar, Water Vapor Raman Lidar, and Water Vapor Differential Absorption Lidar

In the UV, visible, or near-IR, lidar signals can have a strong sensitivity to both WV and *T*. For the derivation of *T* profiles the TRRL and for WV profiles the WVRL or the WVDIAL techniques can be applied. As range-resolved measurements are performed and the solution of the lidar equation is unique, we call the determination of WV and *T* profiles with lidar a *derivation*. Consequently, a higher accuracy and resolution in comparison to passive remote sensing retrievals can be expected. Typically, measurements with a range resolution of a few 10 m to several 100 m and a temporal resolution of 1 s to several 10 min are possible depending on the range. However, lidar systems are more complex with respect to system setup, maintenance, and routine operation, which concern all components such as the laser transmitter, the receiver, and the data acquisition system.

Lidar systems perform measurements with high SNR in the cloud-free atmosphere and through optically thin clouds. In the presence of optically thick clouds, range-resolved measurements are possible within clouds for an optical thickness typically not exceeding 2; otherwise, measurements are possible up to the cloud base. Measurements during rain are hardly possible due to the large extinction of the transmitted radiation. Therefore, similar operation times can be achieved as for IR spectrometers.

The high resolution and the accuracy of ground-based WV lidar measurements have been demonstrated with WVRL [e.g., *Whiteman et al.*, 2006b] and WVDIAL [*Wulfmeyer and Bösenberg*, 1998]. The first operational WVRL at the ARM SGP (36.61°N, 97.49°W) site in the U.S. has been running in an almost continuous mode since February 1998 [*Goldsmith et al.*, 1998; *Turner and Goldsmith*, 1999]. Similar systems came in operation, e.g., in Payerne, Switzerland, by Meteo-Swiss, the Raman Lidar for Meteorological Observations (RALMO) [*Dinoev et al.*, 2013; *Brocard et al.*, 2013], and in Lindenberg, Germany, by the German Meteorological Service (DWD), the Raman Lidar for Atmospheric Moisture Sensing (RAMSES) [*Reichardt et al.*, 2012], and the WVRL operated at the Cabauw site [*Apituley et al.*, 2009]. The current operational systems at observatories of the meteorological services and the ARM sites are shown in Figure 5 together with the global network of passive remote sensors. Figures 4 and 5 demonstrate that huge data gaps remain over all regions of the Earth with respect to TD profiling in the lower troposphere.

A variety of additional WVRL research systems have been developed and are operated by different international scientific institutions. Some of these systems do not have an exclusive dedication to WV, as, in fact, they have multipurpose atmospheric applications; however, they provide high performance in terms of WV measurement

capability. These include the Scanning Raman lidar (SRL) of the Goddard Space Flight Center (GSFC) in Greenbelt, USA [*Whiteman*, 2003a, 2003b]; the Backscatter, Extinction, lidar Ratio, Temperature, and Humidity profiling Apparatus (BERTHA) of the Leibniz Institute for Tropospheric Research (IfT) in Leipzig, Germany [*Althausen et al.*, 2000]; the RASC Raman Lidar in Japan [*Behrendt et al.*, 2002, 2004]; the Università della Basilicata Raman lidar system (BASIL) in Potenza, Italy [*Di Girolamo et al.*, 2009a]; the Raman lidar system of the Max Planck Institute for Meteorology (MPI) in Hamburg, Germany; the Water vapour and Aerosol LIDAR (WALI) of the Laboratoire des Sciences du Climat et de l'Environnement in Gif-sur-Yvette, France [*Chazette et al.*, 2013]; the Amazon WVRL in Brazil [*Barbosa et al.*, 2014]; and the new WVRL at the University of Hohenheim in Stuttgart, Germany [*Wulfmeyer et al.*, 2014a; *Hammann et al.*, 2015]. All these systems are housed within seatainers or mobile vehicles, which makes them easily transportable for the specific purposes of field deployments.

Ground-based WVRLs have been successfully applied for studies of mesoscale processes such as long-term WV evolution [*Turner and Goldsmith*, 1999], fronts [*Melfi et al.*, 1989; *Demoz et al.*, 2005], the dry line [*Demoz et al.*, 2006], stratospheric intrusion events [*Di Girolamo et al.*, 2009a], and hurricanes [*Whiteman et al.*, 2001]. Due to advances in daylight background suppression, *Wulfmeyer et al.* [2010] and *Turner et al.* [2014a, 2014b] showed that high-power Raman lidar can even be applied for monitoring profiles of turbulent moments up to the third order in the daytime convective atmospheric boundary layer (CBL). Additionally, the combined use of the WVRL and TRRL techniques has been exploited to perform measurements of relative humidity [*Mattis et al.*, 2002; *Di Girolamo et al.*, 2009b; *Hammann et al.*, 2015], e.g., for the characterization of cloud condensation levels in the CBL and cirrus cloud microphysical properties.

Different lidar techniques can also be applied for temperature measurements in the lower troposphere [*Behrendt*, 2005]. The technique of choice is now the TRRL [*Radlach et al.*, 2008]. TRRL does not show systematic errors even inside optically thin clouds [*Behrendt and Reichardt*, 2000]. Alternative approaches like the high-spectral resolution lidar (HSRL) [*Hua et al.*, 2005] or the DIAL technique [*Theopold and Bösenberg*, 1993; *Wulfmeyer and Bösenberg*, 1998; *Bösenberg*, 1998] produced too large systematic errors (several degrees) in the presence of aerosol layers and thin clouds.

Similar to WVRL, TRRL also performs better at night. A 3-D scanning, combined WVRL and TRRL system, has been realized at the Institute of Physics and Meteorology (IPM) of the University of Hohenheim (UHOH) in Stuttgart, Germany. Other Raman lidar systems include not only WVRL but also TRRL capabilities as well [*Di Girolamo et al.*, 2009a; *Newsom et al.*, 2013]. Like WVRL, the TRRL performance, too, can be scaled with the laser power and receiver size. With narrowband filters and UV primary wavelengths, the measurements have been extended to daytime [*Behrendt et al.*, 2002, 2004; *Di Girolamo et al.*, 2004a, 2009a; *Arshinov et al.*, 2005; *Radlach et al.*, 2008; *Hammann et al.*, 2015]. Recently it has been shown that even noontime CBL turbulence studies are possible with the IPM TRRL [*Behrendt et al.*, 2015]. Furthermore, scanning ground-based operation has been applied to observe the 3-D structure of *T* and its gradient at the CBL top [*Radlach et al.*, 2008]. Simulations show that not only future airborne [*Behrendt et al.*, 2004] but also spaceborne TRRLs are feasible [*Di Girolamo et al.*, 2006].

WVDIAL sets very high demands with respect to the properties of the laser transmitter. If these challenges are overcome, WVDIAL measurements can be performed with very high temporal and spatial resolution. This potential has been demonstrated for ground-based vertically pointing systems at the Max Planck Institute for Meteorology in Hamburg, Germany [*Wulfmeyer*, 1998; *Wulfmeyer and Bösenberg*, 1998; *Ertel et al.*, 2005], the Karlsruhe Institute of Technology (KIT) in Garmisch-Partenkirchen, Germany [*Vogelmann and Trickl*, 2008], the University of Montana and the National Center for Atmospheric Research (NCAR) in Boulder, USA [*Repasky et al.*, 2013; *Spuler et al.*, 2015], and at IPM in Stuttgart, Germany [*Wagner et al.*, 2011, 2013a]. The IPM developed the first WVDIAL with 3-D scanning capability [*Behrendt et al.*, 2009; *Späth et al.*, 2014] so that measurements can be started close to the surface. Using the DIAL technique, WV profiles can be derived that do not require a calibration of the received signals [*Ismail and Browell*, 1989; *Bösenberg*, 1998]. This makes DIAL currently the most accurate WV remote sensing technique. This has been confirmed by various comparisons with other sensors [*Wulfmeyer and Bösenberg*, 1998], particularly during the ARM Water Vapor Intensive Observation Periods (IOPs) [*Browell et al.*, 1996; *Revercomb et al.*, 2003; *Ferrare et al.*, 2004], IHOP_2002 [*Whiteman et al.*, 2006a, 2006b; *Behrendt et al.*, 2007a, 2007b], COPS [*Bhawar et al.*, 2011], and during recent dedicated intercomparison campaigns [*Wulfmeyer et al.*, 2014a; *Späth et al.*, 2014]. Also,

for validation of other sensors, WVDIAL and calibrated WVRL systems have been applied [*Revercomb et al.*, 2003; *Ferrare et al.*, 2004]. A comparison between spaceborne passive remote sensing and DIAL is presented in *Wulfmeyer et al.* [2005] and *Masiello et al.* [2013].

Well-designed WVRL and WVDIAL systems were acknowledged by WMO as reference standards for WV measurements in the atmosphere with an accuracy of < 5% throughout the troposphere. For instance, these systems were proposed as component of level-1 water vapor reference stations within the GCOS Reference Upper Air Network (GRUAN) [*Thorne et al.*, 2013]. The final limitation of the accuracy of WVDIAL for climatological measurements is the knowledge of spectroscopic parameters, which can be improved by more accurate laboratory measurements. It has been demonstrated that WVDIAL provides the best combination of resolution and accuracy for daytime WV profiling [*Wulfmeyer*, 1999a].

Ground-based and airborne WVDIAL systems have been applied for studies of ABL heterogeneity [*Kiemle et al.*, 1995], for deriving turbulence statistics and latent heat fluxes [*Senff et al.*, 1994; *Kiemle et al.*, 1997; *Wulfmeyer*, 1999a; *Giez et al.*, 1999; *Linné et al.*, 2007; *Wulfmeyer et al.*, 2014a; *Turner et al.*, 2014b; *Muppa et al.*, 2015] and comparisons of turbulence statistics with large-eddy simulations (LES) [*Wulfmeyer*, 1999b]. Studies of the mesoscale WV field [*Ferrare et al.*, 2004; *Wakimoto et al.*, 2006] and of tropospheric-stratospheric exchange were also possible [*Ehret et al.*, 1999; *Flentje et al.*, 2005]. As DIAL and Raman lidar systems are becoming operational, they can be applied for model evaluation [*Hennemuth et al.*, 2008; *Milovac et al.*, 2014]. Recent advances include the first scanning operation of DIAL for studying land surface exchange and lower tropospheric transport processes [*Behrendt et al.*, 2009; *Späth et al.*, 2014]. Furthermore, DIAL systems have been used for studying CI and the preconvective environment in complex terrain [*Wulfmeyer et al.*, 2011; *Behrendt et al.*, 2011; *Corsmeier et al.*, 2011].

It should be pointed out that current TD profilers based on lidar techniques can still be improved with respect to accuracy and resolution. This is possible by increasing the transmitter power (typically to the eye-safety limit) and receiver efficiency and by optimizing the laser transmitter properties, e.g., with respect to its spectral properties. The derivation of TD profiles can be adapted to user needs by trading off the vertical and temporal resolution. These dependencies are very well understood and derived for TRRL in *Behrendt* [2005], for WVRL in *Whiteman* [2003a, 2003b], and for WVDIAL in *Wulfmeyer and Walther* [2001a, 2001b].

For routine TD profiling it is necessary that lidar systems can also be operated on shipborne platforms or buoys. In principle, shipborne operation is possible as demonstrated in *Bluestein et al.* [2001]. Routine operation in networks, e.g., using WVDIAL, requires a more compact and reliable design. A system based on diode laser technology was recently presented in *Spuler et al.* [2015]. The corresponding lidar methodology is presented in section 5.2.3.

Due to these technological challenges, only recently have lidar networks for observing atmospheric profiles been developed and placed into operation. The most important examples are the ARM network, the NASA Micro Pulse Lidar Network (mplnet.gsfc.nasa.gov), the European Aerosol Research Lidar Network (EARLINET, www.earlinet.org), and the Network for the Detection of Atmospheric Composition Change (NDACC, www.ndsc.ncep.noaa.gov). The locations of the sites are shown in Figure 5. These networks are measuring different variables. The simplest application is the observation of lidar backscatter profiles, which contain information about aerosol layers, the ABL depth, and clouds. Only a part of these networks are measuring WV profiles such as some NDACC and EARLINET stations, mainly using WVRL and one WVDIAL. However, most of them are focusing on measurements starting in the middle troposphere so that surface and ABL processes are hardly observed.

4. Key Applications and Requirements of Water Vapor and Temperature Profilers

The specifications for observing systems to fulfill the desired measurement quality depend strongly on the user demands. For instance, WV profiling for climate research requires moderate temporal and spatial resolution but must have small biases that are independent of the day or night conditions. This accuracy requirement must be stable over decade length scales to successfully be used for trend analyses. For weather research, *Weckwerth et al.* [1999] and *Wulfmeyer et al.* [2003] stated that ground-based networks are required to measure inhomogeneities of the 3-D temperature and water vapor field within 10 min, a vertical resolution of a few hundreds of meters, and a horizontal resolution of a few kilometers. The RMS error should be 0.5 K

or $< 5\%$, respectively. Since these first general assessments of WV measurements, it is necessary to revise those estimates because significant progress has been made in observations, mesoscale modeling even down to the grey zone, and process understanding. Furthermore, it must be considered that the demands of the weather and climate communities are approaching each other more and more due to their capabilities to include similar complexities in model physics and to simulate processes on similar scales.

The specific demands of the end users should also be taken into account. Mainly three aspects are considered important: The performance of the thermodynamic profiler should exceed (a) the capabilities of existing instrumentation with respect to routine operation and calibration, (b) the temporal and spatial resolution of the currently available TD observations, and (c) our existing capability of representing the 3-D distribution of WV and T fields in all climate regions. In order to study point (c), results of present weather forecast and regional climate models can be applied as well, which, however, should be carefully interpreted as they are limited by their current resolution and performance.

The following overarching applications have been identified and are discussed in order of increasing user demand: (1) monitoring, (2) verification and calibration, (3) data assimilation (DA), and (4) process studies.

For topics 1–4 the following stringent profiling requirements are identified and discussed:

1. *The accuracy of the measurements according to well-defined temporal and vertical resolutions* (*see Appendix A for an overview of definitions of errors and their estimation*). We define accuracy here according to the International Organization for Standardization (ISO) 5725 standard as the combination of the *bias* (*systematic error or trueness*) and the *noise error* (*precision*). When accuracy is estimated by a least square algorithm, it corresponds to the *RMS error*. The bias refers to the closeness of the mean of the measurement to the true value. This systematic deviation cannot be removed by averaging. The bias can be estimated either theoretically or by intercomparisons. If a theoretical analysis is possible, e.g., by end-to-end performance models, an expected bias range for the instrument can be specified. However, usually it is not possible to determine whether the bias is positive or negative. If the bias is determined by comparisons, the existence of a reference standard is assumed. The bias of a single TD profile can be determined, if the noise errors are negligible. However, usually a bias statistics is derived by a large set of comparisons under different meteorological conditions. The noise error is given by the shape of the probability density function (PDF) of the measurement. The methodologies for deriving this error characteristic depend on the remote sensing technique, namely, passive or active. In contrast to the bias, the noise error can be reduced by improving the SNR of the measurement. Similar to the bias, the noise error can be determined for a single profile either theoretically by noise error propagation using the measurement methodology or by the characterization of the retrievals or the derivations. Alternatively, a large set of comparisons with a reference standard can be produced assuming that the RMS error of the reference is negligible. This demonstrates the importance of the development of reference standards for TD profiling. For retrieval and derivation characterizations and DA applications, the *noise error covariance matrix* must be specified.

2. *The range resolution.* This is defined as the distance between statistically independent range bins in the derivation or the retrieval of TD profiles. In active remote sensing, the range resolution is determined by range averaging of the return signals with the constraint of the range weighting functions given by the pulse duration of the transmitter or the resolution of the digitizer whatever is coarser. In passive remote sensing, it is constrained by the width of weighting functions in the RTE.

3. *The minimum and maximum range of the measurements.* The minimum range is usually limited by the setup of the receiver optics and scanning capabilities. In the case of active remote sensing, the overlap function between the transmitter and the receiver is critical and the maximum range is limited by signal statistics. In the case of passive remote sensing, the minimum range is right at the instrument and maximum range is achieved when the width of the averaging kernels is degrading to several kilometers or the information content in the observations drops close to zero.

4. *Coverage and density.* The domain and mean distance of the sensors of a potential network of profilers.

5. *Operation under specific weather conditions.* What are the most important weather conditions where the respective thermodynamic profiling can be performed? This includes a discussion whether it would be more critical to make observations during rain or during the preconvective environment.

6. *The climate regions where the measurement can be performed maintaining the specifications above.* In many applications, measurements in all climate regions of the Earth are not necessary; however, critical regions can be identified.

4.1. Monitoring
4.1.1. Importance and Applications

Monitoring is the continuous observation of a variable of the Earth system. The requirements are strongly dependent on the user demands and the application but there is usually no limit of operation time; the data set should be collected as long as possible. The goal of monitoring is the derivation of climatologies of specific variables with suitable resolution and accuracy with respect to the application. This is getting more and more attention in the era of anthropogenic climate change and is important in all climate regions.

Monitoring does not necessarily imply a high temporal and/or spatial resolution. In many cases, an observation twice a day or even once a day may be sufficient. A key aspect is the reproducibility of the measurement and the maintenance of the performance characteristics of the remote sensing system. Generally, a minimization and characterization of systematic errors is of major concern.

Common examples are the global radiosonde network or the surface networks of the meteorological services. Here simultaneous measurements are performed for deriving statistics, gridding of the data for model comparisons and for consistent DA. However, as demonstrated in section 3, the spatial density of these measurements is far from being sufficient for deriving climate trends on the mesoscale.

4.1.2. Requirements Set to Observing Systems

Taking into account the analyses performed in sections 2 and 3, new tools for monitoring of TD profiles should exceed current capabilities of observing systems and support the current generation of model systems. The requirements include a specific accuracy at a well-defined temporal and vertical resolution. The minimum and maximum range of the measurements needs to be given where the temporal and spatial requirements are maintained. Furthermore, the climate region, where the measurements are performed, needs to be specified.

With respect to the temporal resolution, the profiles should be able to resolve the diurnal cycles of WV and T. Observations are important in daytime in the convective mixed layer and at night in the stable ABL. This requires a *temporal resolution of $\leq 1\,h$*. Important is the resolution of the water vapor profile throughout the ABL up to the lower troposphere. Gradients close to the surface and at the ABL top should be monitored. This requires a vertical resolution of a few *10 m close to the surface*, *100–300 m in the convective mixed layer*, and *10–100 m in the interfacial layer*. At these resolutions, the *systematic error (bias) in the WV profiles should be < 5%* because this corresponds to or exceeds the performance of other observing systems [*Ohring et al.*, 2005]. A *lower bias down to 2%* would be even more useful because the WV profiler could be used as reference standard. In fact, if a provider of a TD profiler can claim a systematic error clearly below 5%, users could eliminate bias corrections, a process that is known to be both challenging and time consuming.

At the specified vertical and temporal resolution, the WV *noise error should be < 10%*, because this should still allow the user to derive daily diurnal cycles. Furthermore, for deriving statistics on different scales (monthly, seasonal, etc.), the resulting WV distribution functions will hardly be influenced by these noise error characteristics.

In the case of T profiling, the *bias should be < 0.5 K and the noise error < 1 K* for detecting regional climate trends and resolving weather processes such as CI. A *bias of 0.2 K* would be even better for reducing the averaging time for detecting temperature trends. The same vertical resolution as for WV should be maintained so that temperature gradients can be detected.

The coverage and spatial resolution depend strongly on the user demands. However, recent progress in process understanding such as LSA interaction and convection initiation should be considered. Representative observations seem only to be possible if the density of the profiles covers the meso-beta to the meso-gamma scale in order to capture the high variability of WV and T. We suggest focusing on orographic terrain, terrain with strong land surface heterogeneity (land-sea contrast, vegetation boundaries, etc.), terrain with high precipitation amounts, urban areas, and megacities.

Concerning the weather conditions where the profiling should be performed, an all-weather observing system is usually requested. This capability would avoid sampling errors in climatologies with respect to certain weather conditions. If this is not possible, the preconvective environment including ABL measurements would be very beneficial because this sets the environment for CI. In principle, also measurements are requested in and above ABL clouds, which are often limiting the measurement range for ground-based IR passive remote sensors and lidar systems.

4.2. Verification and Calibration
4.2.1. Importance
Verification and monitoring may appear similar, but in practice, there are significant differences in detail. Monitoring requires continuous long-term measurements for deriving climatologies. The analysis of these climatologies is generally model independent and may lead to improved process understanding of the Earth's water and energy cycles.

In contrast, verification is the process of assessing the quality of a *model simulation*. Model simulations may be weather forecasts, a prediction of the future state of climate, reanalyses, and hindcasts of weather and climate using different model configurations. For instance, regional climate models are usually verified by downscaling experiments in the past (e.g., for CORDEX the verification period is 1989–2009) where the models are driven at the boundaries by GCMs or reanalyses such as ERA-Interim.

Consequently, the verification process depends on the model configuration, the time period, and the variables of interest. It is obvious that WV and *T* are the critical variables for verification because they link land surface exchange and ABL development with the development of clouds and precipitation.

In weather forecasting, verification is routinely performed by meteorological services and it is an extremely important task. Here the goals of verification include (1) the *monitoring* of forecast quality—how accurate are the forecasts and are they improving over time? (2) the *improvement of* forecast quality—the first step toward getting better is discovering what is going wrong—and (3) the *comparison* of the quality of different forecast systems—to what extent does one forecast system give better forecasts than another, and in what ways is that system better?

More details are presented on the website of the WWRP Joint Working Group on Forecast Verification Research (JWGFVR) (www.wmo.int/pages/prog/arep/wwrp/new/Forecast_Verification.html) and in *Ebert et al.* [2013]. Verification research is not only dealing with the development and application of present or new scores. Another important component is the handling and analysis of point and gridded data sets. This is not a trivial task because data sets suffer from sampling errors, representativeness errors, systematic errors, and noise errors. The JWGFVR strongly recommends the gridding of observational data to the resolution of the models in order to reduce sampling and representativeness errors. As pointed out above, this requires the setup of denser networks of TD profilers in order to reduce these errors and to provide gridded data sets on the meso-gamma scale for the new generation of weather and climate models.

The verification of observing systems can be achieved through the comparisons of their calibration and retrieval methodologies. If the WMO acknowledges that an observing system has a particularly high accuracy, it is recommended as a WV or *T* reference standard. The methodology for comparing different kinds of WV measurement techniques was derived and presented in a variety of publications [*Turner et al.*, 2003; *Ferrare et al.*, 2004, 2006; *Behrendt et al.*, 2007a, 2007b; *Bhawar et al.*, 2011].

4.2.2. Requirements
Based on the considerations above, verification demands more stringent requirements than monitoring. Such requirements are driven by the model and instrument developers. Lower tropospheric measurements are particularly critical for verification, as this allows for studying the skill of the model system simulating land surface exchange, entrainment, CI, and the development of clouds and precipitation.

With respect to the temporal resolution, important processes such as CI need to be verified in the daytime and at night. This requires a *temporal resolution of ≤ 15 min*. A similar vertical resolution as for monitoring is required, e.g., a vertical resolution of a few 10 m close to the surface, 100–300 m in the convective mixed layer, and 10–100 m in the interfacial layer. Again, the profiles should get as close as possible to the ground and reach about 3–4 km.

The systematic error (bias) in the WV profiles should be as low as requested for monitoring in order to avoid systematic errors in the derivation of skill scores and for instrument intercomparisons and calibration. A *systematic error of < 5%* is considered very beneficial, a bias down to 2% would be even more interesting because then the WV data would become a reference standard. Again, as for monitoring, this low systematic error is expected to be a very desirable feature for weather forecast centers and space agencies, as bias corrections can be avoided.

At the specified vertical and temporal resolution, the *noise error should be < 5%* because this should still be sufficient to identify atmospheric processes such as the development of convergence lines, CI, and land surface heterogeneity. This results in an *overall accuracy requirement of better than 10%*. Again, for deriving verification statistics on different scales (monthly, seasonal, etc.), the resulting WV distribution functions need to be nearly independent of noise error characteristics. The requirements for T measurements are a *bias of 0.2–0.5 K* and a *noise error of < 1 K*.

An optimal network design should provide the best compromise between current data availability, coverage, and station density, which is subject of research activities on its own (e.g., *Muller et al.* [2013]). As in monitoring, the data used for verification should be representative for the grid cells of the model so that the density of the profilers should reach the meso-beta to the meso-gamma scale. Again, a reasonable start would be the setup of networks in target regions such as domains with strong surface heterogeneity and strong precipitation, as well as urban areas including megacities. Networks with similar density should be made available in different climate regions in order to compare model performance. A different network design may be set up for calibration. In this case, the coverage should comply with the observation capabilities of the sensors to be calibrated. For instance, for polar orbiting satellites, ground-based WV and T profilers may be set up in such a way that measurements are collected during certain local times corresponding with the overpasses of the Sun-synchronous satellites.

Verification and calibration is important during all weather conditions. A usual first step is the determination of scores averaged over all weather conditions. However, it is also common to separate verification scores with respect to forcing conditions. It is reasonable to distinguish between forced/frontal situations, forced/nonfrontal conditions, and local forcing. Details are discussed in *Wulfmeyer et al.* [2011]. The performance of models generally depends on the interaction of forcing conditions because different processes at different resolutions are involved, which are simulated with different skills.

The preconvective environment during these forcing conditions is therefore critical. Observations within clouds and rain are also beneficial, however, they may be covered by cloud and precipitation radars in combination with T profile information (RH = 100%). There is general agreement that models and new observation systems must be capable of simulating TD fields in clear air before and while clouds are developing. Measurements before and during CI are very important. If the models and observation systems fail already during this period, precipitation forecasts will also fail. Consequently, measurements in the lower troposphere during the preconvective environment will be extremely valuable for model verification and calibration. Model verification and calibration are interesting in all climate regions of the Earth over land and the oceans.

4.3. Data Assimilation
4.3.1. Importance and Methodology
In order to specify the state of the Earth system as accurately as possible, the information content of the model system and of the observations must be used and merged in a consistent manner. Consequently, two sources of information must be considered: (a) The a priori state of the system and its PDF with its temporal development according to the model operator as well as (b) the observations with their PDF and their error covariance matrices. The merging of their information content is called DA and leads to the analysis of the initial state of the system. The information content of observations is maintained in the system by the operation of an *analysis cycle or a rapid update cycle* (RUC). This cycle consists of a forecast step used to assess the next expected a priori state of the system. It follows the analysis step, in which the forecasted fields are merged with the observations. By means of the RUC, the information content of the observations is spread and distributed in the forecast system. As pointed out above, it became state of the art to perform ensemble forecasts on nearly all time scales from nowcasting to the medium range. A corresponding ensemble prediction system will also be capable of merging the ensemble forecast with observations resulting in an improvement of probabilistic forecasts.

DA is not only essential for weather forecasting but it is a key methodology in Earth system sciences. DA can also be applied for the initialization of seasonal prediction and climate models depending on the temporal range of the simulations. Particularly, it is expected that DA of land surface and oceanic data will lead to advanced probabilistic predictive skill on decadal time scales. Another essential application is the consistent and continuous DA of observing systems in a frozen model system from the past to today. This reanalysis—such as ERA-40 and ERA-Interim—can be considered the best estimate of water and energy cycles and other climate statistics (see sections 2.2 and 2.5). Further applications include parameter estimations in land surface-vegetation models, OSSEs, Observing System Experiments (OSEs), uncertainty studies of model systems, and predictability studies.

As far as TD profilers are concerned, they play an essential role in nearly all of these applications. Their assimilation is requested for weather forecasting from nowcasting to the medium range. WV and T profiles are also essential for regional reanalyses, which are currently in preparation within European projects. For all these applications, WV and T DA with advanced observing systems will lead to better forecast skill and advanced understanding of regional water and energy cycles as well as the predictability of atmospheric processes such as precipitation by probabilistic QPF. Particularly, it can be expected that joint DA of clear air TD fields and radar observations in the preconvective environment as well as in and around convective systems will lead to a reduction of the model imbalance at initial time increasing the impact of radar data [e.g., *Kawabata et al.*, 2011; *Bluestein et al.*, 2014].

Nearly all current DA methodologies rely on Gaussian error distributions of the model and the observations and employ two approaches: variational (VAR) analysis and extended Kalman filter (EKF). It can be shown that these methodologies are related to each other under certain conditions but this is beyond the scope of this review. Here it is sufficient to study the most important properties of these solutions. We distinguish between the optimal least squares estimator or variational (VAR) analysis and the ensemble-based DA. The variational analysis can be implemented in various ways such as the "Best Linear Unbiased Estimator (BLUE)" algorithm, the 3-D, or the 4-D variational (3-DVAR or 4-DVAR) techniques. The variational technique is in principle a computationally affordable approximation of the BLUE algorithm. Variational techniques need an estimation of model and observation errors and their correlation. These are called the model error background matrix $\boldsymbol{B}$ and the observation error covariance matrix $\boldsymbol{R}$, respectively.

The other technique is the EKF. It requires an analysis of the Kalman gain matrix and of the error covariance matrices $\boldsymbol{B}$ and $\boldsymbol{R}$. It can be shown that the solution of the EKF is extraorbitant for our system of interest so that an approximation must be developed. This is the ensemble Kalman filter (EnKF), which approximates the EKF by an ensemble of forecasts and leads to the current generation of ensemble-based DA techniques. An advantage of the EnKF over variational techniques is that it provides not only an analysis of the present state with an error estimate but also a flow-dependent update of the $\boldsymbol{B}$ matrix. However, it should also be mentioned that similar results can be achieved with an ensemble of variational analyses (En3-DVAR or En4-DVAR). In any case, an update of $\boldsymbol{B}$ in each analysis step is considered very important due to the chaotic nature of the Earth's weather and climate system. Both 3-DVAR and EnKF are intermittent DA techniques where the observations are assimilated at well-defined analysis times. Typically, a RUC of 1–3 h is applied on the mesoscale but in connection with radar DA even higher update rates have been proposed up to 5 min [*Sun*, 2005; *Stensrud et al.*, 2009].

In contrast, 4-DVAR, which continuously assimilates observations during a DA window, is a smoother. This is an advantage for assimilating data with high temporal resolution such as lidar and radar. Furthermore, model spin up or inconsistencies at initial time are reduced, which is important for improving forecast skills from nowcasting to the short range [*Kawabata et al.*, 2014a]. However, on the convection-permitting scale, 4-DVAR becomes computationally demanding. Nevertheless, at nearly all major weather forecasting centers, both the variational and ensemble-based DA techniques are being investigated and even hybrid approaches are under consideration combining their respective advantages [e.g., *Barker et al.*, 2012; *Zhang and Zhang*, 2012; *Clayton et al.*, 2013].

Both variational and ensemble-based DA systems are capable of handling indirect observations, e.g., from passive remote sensing systems. This is a huge advantage of both techniques in comparison to traditional techniques such as nudging. Indirect observations are assimilated by application of a model observation operator $\boldsymbol{H}$. This operator is in principle the application of the RTE to the model variables in order to simulate the observations such as radiances. As many state-of-the-art remote sensing observations of WV and T are based on indirect or passive remote sensing measurements, this makes the study of $\boldsymbol{H}$ a very important
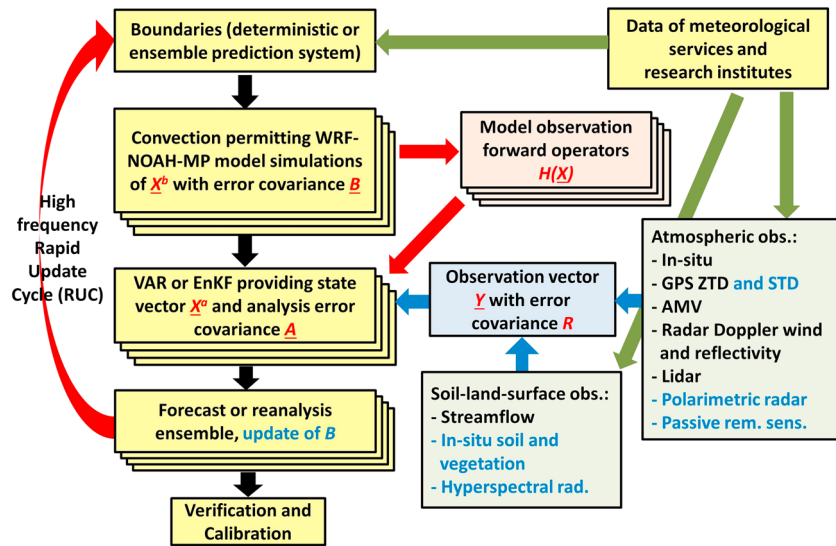
Figure 6. Setup and ingredients of an ensemble variational or ensemble-based forecast system using advanced observations. It is based on the WRF–NOAH-MP model system and currently under development at IPM. Marked in red are the operators essential for closing the gap between model output and observations as well as for estimation of observational and model errors. Black observations in the green boxes: Ready and used for assimilation. Blue observations in green boxes: In preparation for assimilation. AMV: Atmospheric motion vectors.

research area. Furthermore, this issue makes TD observing systems very interesting, because they provide direct measurements and minimize the development and application of **H**. This is due to the fact that the impact of indirect measurements into a DA system is suboptimal due to cross sensitivity to other variables, unknown cross terms in the error covariance matrixes, and due to the introduction of systematic errors.

For characterizing the DA process, the error covariance matrix of the analysis **A** is very important. It reads

$$\mathbf{A} \cong \left[\mathbf{B}^{-1} - \mathbf{H}^T\mathbf{R}^{-1}\mathbf{H}\right]^{-1} \quad \text{for} \quad \text{3-DVAR,}$$
$$\mathbf{A} \cong \left[\mathbf{B}^{-1} - \mathbf{M}\mathbf{H}^T\mathbf{R}^{-1}\mathbf{H}\mathbf{M}\right]^{-1} \quad \text{for} \quad \text{4-DVAR,} \quad \text{and} \tag{5}$$
$$\mathbf{A} \cong \mathbf{B}\mathbf{H}^T\left[\mathbf{H}\mathbf{B}\mathbf{H}^T + \mathbf{R}\right]^{-1} \quad \text{for} \quad \text{EnKF,}$$

where **M** is the model forward operator. This substantiates the expectation that the impact of an observing system to the analysis is particularly strong if $\mathbf{R}_{ij} \ll \mathbf{B}_{ij}$. An example of a future variational or ensemble-based 3-DVAR model system currently under development at IPM [*Schwitalla et al.*, 2011; *Schwitalla and Wulfmeyer*, 2014] is presented in Figure 6. It is based on WRF coupled to the NOAH-MP land surface model [*Jiménez et al.*, 2012; *Niu et al.*, 2012]. This system can be applied for reanalyses, nowcasting to medium-range probabilistic forecasting as well as OSEs and OSSEs. Except for standard observations of the ECMWF MARS archive, new observations on the mesoscale can already be assimilated or are in preparation for assimilation. Of great interest are additional TD observations provided by passive profilers and lidar systems [*Wulfmeyer et al.*, 2006; *Grzeschik et al.*, 2008] or using GNSS STDs [*Zus et al.*, 2011; *Kawabata et al.*, 2013]. Particularly, it is expected that the assimilation of TD profiles provided by ground-based networks will reduce the model imbalance at initial time and lead to improved, seamless forecasts from nowcasting to the medium range.

Whereas WVDIAL, WVRL, and TRRL data can be directly assimilated, passive remote sensing systems still require the development of suitable model forward operators for the IR and the MWR, which should be strongly pursued. In principle, a future DA system should be capable of a consistent incorporation of hydrological variables such as soil moisture and streamflow, from which the latter was realized by *Warrach-Sagi and Wulfmeyer* [2010], as well as land surface, vegetation, and atmospheric variables [*Wulfmeyer et al.*, 2014b, 2014c].

For impact studies, OSEs are using existing WV and *T* profilers; however, this needs the existence, setup, and operations of these instruments in the real world. Another way to assess the impact of new observation

systems is the performance of OSSEs. Here the impact of additional observations is compared with respect to a sophisticated nature run. OSSEs have the advantage of being capable to simulate and to study the impact of observing system networks that do not exist yet. Initial OSSEs comparing the impact of passive and active remote sensing systems have been performed by *Otkin et al.* [2011] and *Hartung et al.* [2011]. However, these studies did not simulate the full set of observations, which are routinely available such as radar networks, plus the additional observations of new instruments. This is essential because the impact of new observations will be artificially increased, if other observations are omitted. Therefore, it is very important to perform new OSSEs on the mesoscale in order to assess the impact of networks of ground-based WV and *T* profilers.

4.3.2. Requirements

The temporal resolution of the observations should correspond to the resolution of the DA RUC. A *resolution of 1 h* is the minimum requirement for resolving the diurnal cycle and for reaching the nowcasting range. If radar data are to be assimilated, which are usually provided with a temporal resolution of 5 min, this should be done with other observations as well. If smoothers such as 4-DVAR or the Kalman smoother are applied, the *temporal resolution should be about 5–10 min* as well in order to take advantage of the information content of high-resolution observing systems in the DA windows [e.g., *Sun*, 2005; *Kawabata et al.*, 2011]. A corresponding resolution is also very interesting for quantitative precipitation estimation, NWP for nowcasting, and QPF.

The vertical resolution should be similar to the one used in monitoring and verification, because for DA the fine structure of the lower tropospheric WV and *T* profiles is critical. Furthermore, the structures from the ground to the lower troposphere (3–4 km) need to be observed in order to ensure a high impact on the mesoscale analysis.

The systematic and the noise errors of the WV and *T* profiles should be considerably lower than the diagonal terms in the model background error covariance matrix **B**. Unfortunately, the derivation of this matrix is quite uncertain and a research area of its own. Nevertheless, the **B** matrix of mesoscale models gives fundamental insight on whether a WV or *T* profile will have a positive impact. It can be expected that an observing system with a *bias of < 5%* will be accurate enough to avoid a bias correction. Current experience from global and mesoscale modeling demonstrates that model errors are about 20% in the ABL. An example is found in *ESA* [2001] where the values of the relative errors associated with the model WV background field at several pressure levels are shown for the models of the Canadian Meteorological Center (CMC) and the UKMO. From the surface to the lower troposphere, the errors increase from 20% to 30%. Recent results of the determination of the **B** matrix using mesoscale models point at humidity background errors of $\approx 1 \, g \, kg^{-1}$ in the ABL [e.g., *Brosseau et al.*, 2011], which corresponds to 5–10% during most meteorological conditions. The temperature background errors are estimated to be < 1 K. Correspondingly, the *noise error should be < 10% or < 1 K* to ensure a significant impact of the observations. DA requires not only the specification of noise errors but also of *the noise error covariance matrix* **R**. Therefore, the observation system must be capable of providing the **R** matrix for the measurement configuration and all weather conditions. During events with strong nonlinearity of the involved processes such as cloud development and precipitation, the determination of the **R** and **B** matrices is still subject for research [e.g., *Montmerle*, 2012].

A high density and large coverage of the profilers is essential to ensure that under all upstream conditions, the information content of the WV and *T* profilers is ingested downstream in the model domain. The coverage, density, and location of the network for ensuring improvement of forecast skills are important areas of OSEs and OSSEs which unfortunately are lacking on the mesoscale yet. With respect to weather conditions, observations in the preconvective environment are essential. A particular high impact is expected, if the TD profilers are applied in synergy with radar networks as shown in *Kawabata et al.* [2011, 2014b] and *Schwitalla and Wulfmeyer* [2014]. This is due to the fact that strong model imbalances with respect to the TD field are incorporated if just single-radar observations are assimilated. Thus, the point is not the operation of WV and *T* measurements under "all weather conditions" but their synergetic, well-designed operation in combination with other observing systems. In any case for DA, a positive impact of a TD profiler network is expected in all climate regions. Particularly critical are regions with high-impact precipitation events such as the midlatitudes, the subtropics, and tropics, especially the monsoon regions.

4.4. Process Studies

4.4.1. Most Important Applications

As pointed out in section 2, WV and T distributions are the results of a large number of interwoven processes in the Earth system. The understanding of the mesoscale water cycle including all its phases and forecasts of extreme events are two of the most important topics.

This interaction is dependent on the forcing conditions, which has been discussed for the midlatitudes in connection with CI in *Wulfmeyer et al.* [2011] and for the tropics in *Stevens* [2005]. For CI, large-scale lifting is essential, which can be caused by forced-frontal situations, weakly forced conditions (e.g., no surface front but upper level instability) or by local forcing, e.g., due to orographic flow. Upper level instabilities are due to potential vorticity advection, e.g., related to troughs and Rossby waves. The relative strength and interaction of these forcing mechanisms result in the development of cloud and precipitation systems. High-resolution WV and T measurements are able to identify these instabilities and the corresponding forcing conditions.

Particularly critical are WV transport and exchange processes in the ABL, which are indicated in Figure 2. Heterogeneity of the soil and the land cover as well as the orography cause a spatial modulation of the surface energy balance. This results in a spatial variability of the ABL depth and complex mesoscale flow pattern. These structures determine and modulate the development, shape, and strength of convergence zones that lead to the development and organization of clouds and precipitation. All these processes are imbedded in and controlled by the large-scale environment.

Critical gaps in process understanding mainly exist at interfaces where the exchange of water is important. This includes the land surface including the land cover, the interfacial layer at the top of the ABL, and cloud and precipitation microphysics, the latter requiring measurements of relative humidity. Various international projects are currently investigating the surface flux heterogeneity over the vegetated land surface and its feedback to ABL structure and entrainment [*Santanello et al.*, 2009, 2011; *Holtslag et al.*, 2013]. A correct simulation of weather conditions and climate statistics requires a realistic modeling of the interaction of the large-scale and small-scale processes explained above. This is only possible with very dense networks or high-resolution 3-D scanning sensors.

4.4.2. Requirements

For process studies, the requirements depend strongly on the application but are generally stringent because of the importance of turbulence and the variability of water vapor transport processes on the meso-gamma scale. For instance, for water vapor flux measurements in the convective ABL, temporal and vertical resolutions of about 1–10 s and 60 m are required, respectively [*Senff et al.*, 1994; *Wulfmeyer*, 1999a, 1999b]. The temporal and spatial resolution must be even higher in the surface and the interfacial layers. Daytime turbulence resolution has been achieved with WVDIAL [*Muppa et al.*, 2015], WVRL [*Wulfmeyer et al.*, 2010; *Turner et al.*, 2014a, 2014b], and recently with TRRL [*Hammann et al.*, 2015; *Behrendt et al.*, 2015]. Daytime scanning applications, e.g., for 3-D studies of CI, need even higher resolution and large range [*Wulfmeyer and Walther*, 2001a, 2001b]. Currently, these requirements can only be met by research, ground-based TD remote sensing systems such as high-power WVDIAL [*Behrendt et al.*, 2009; *Wagner et al.*, 2013a; *Späth et al.*, 2014].

4.5. Summary

In this section, an overview of future applications of WV and T profilers was presented. Four fields were identified as most important applications: (1) monitoring, (2) verification and calibration, (3) data assimilation (DA), and (4) process studies.

For each topic, the use of profilers was explained and discussed in detail. Corresponding requirements were derived. The results are summarized in Table 1. Table 1 demonstrates that the requirements are similar for various applications. The vertical resolution should be sufficient for resolving temperature and moisture gradients in the lower troposphere (10–100 m). The bias should be 2–5% (0.2–0.5 K) and the noise errors < 10% (<1 K) in a single vertical range bin. For monitoring and DA, it is essential that this low bias is maintained over a long time. The main differences are in the temporal resolutions. The highest temporal resolution of 1–60 s is required from process studies where 3-D structures and/or turbulent fluxes have to be resolved. For DA applications, modern NWP systems are reaching the nowcasting range where update cycles of 5–10 min are envisioned. These require also a fast processing of the TD retrievals or derivations with a very short latency of the data. The networks should be operated on the meso-beta to the meso-gamma scales in all climate regions over land and over the oceans.

Table 1. Requirements for TD Profilers, Which Are Useful for Monitoring, Verification, DA, and Process Studies (Compiled From *Weckwerth et al.* [1999], *Wulfmeyer et al.* [2003], *ESA* [2001, 2004], and *WMO* [2004, 2005])

Parameter	Monitoring	Verification	Data Assimilation	Process Studies
Vertical resolution in ABL (m)				
Surface layer	10–30	10–30	10–30	10
Mixed layer	100–300	100–300	100–300	10–100
Interfacial layer	10–100	10–100	100	10–100
Lower free troposphere	300–500	300–500	300–500	100
Time resolution (min)	<60	<15	5–15	1/60 to 1
WV noise error (%)	<10	<5	<10 + noise error covariance matrix	<10
WV bias (%)[a]	2–5	2–5	<5	<5
T noise error (K)[a]	1	1	1	0.5
T bias (K)	0.2–0.5	0.2–0.5	0.2–0.5	0.2–0.5
Latency (min)	—	—	1 for nowcasting	—
			Minutes to 1 h for short-range weather forecasting	
Horizontal resolution of network	Mesoscale	Meso-beta to meso-gamma scale	Meso-beta to meso-gamma scale	Turbulence to meso-gamma scale
Coverage			All climate regions	

[a]Must be time independent.

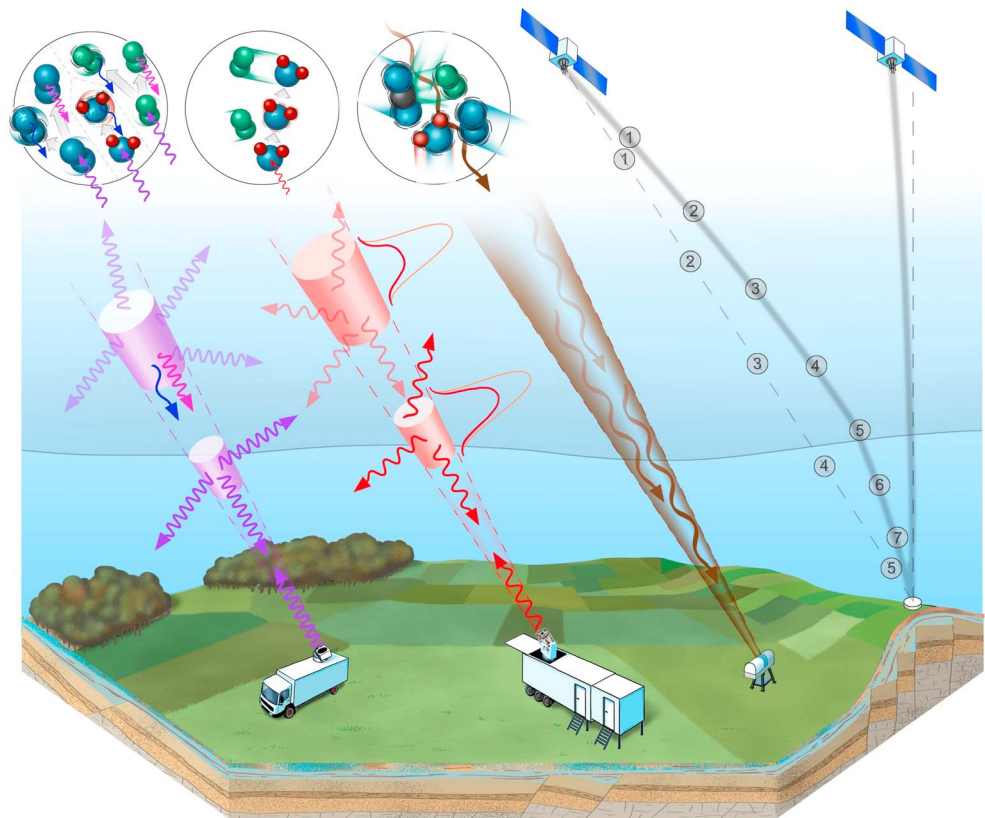## 5. Remote Sensing Methodology

Active and passive remote sensing systems are based on various physical principles, which need to be considered in a comparison of their performance and limitations. Passive remote sensing exploits the interaction of optical, IR, and MW radiation with matter. Active remote sensing analyzes the interaction of transmitted electromagnetic waves with matter from the ultraviolet (UV) to the MW. The matter to be considered can be the land surface consisting of the soil and the canopy layers as well as the constituents of the atmosphere, which consists of molecules, aerosol particles, and hydrometeors. In dependence of frequency, this requires the understanding and simulation of scattering processes, extinction due to scattering and absorption, nonlinear scattering for Raman lidar, and the propagation, bending, and delay of radiation in an inhomogeneous medium for GNSS – all of which are wavelength dependent. Thus, remote sensing is a research field, which combines our knowledge and creativity in the use of laws of classical physics, thermodynamics, electromagnetism, and quantum mechanics including nonlinear phenomena such as Raman scattering.

Figure 7 depicts an overview of the most important remote sensing methodologies and geometries. The left ground-based system indicates a lidar system using the inelastic Raman scattering effect for WV and T measurements. In the scattering volume, a photon is absorbed by a molecule, e.g., water vapor, oxygen, or nitrogen, which is immediately excited to an upper vibrational and another rotational level. The wavelength of the scattered radiation is shifted to the red and the blue (depending of the population of the ground state) due to the energy gap between the initial and the final energy level after the transition. The frequency of the backscattered radiation is characteristic for the scatterer and measured in dependence of traveling time so that a range-resolved measurement is possible.

The middle ground-based system shows a DIAL using the absorption of WV for range-resolved absolute humidity measurements. The absorbed photon is lost and extracted from the incident electromagnetic field of the laser. Due to the high pressure of the environment, this energy is immediately transferred to the environment by collision with the surrounding molecules. Therefore, the lifetime of the upper level is determined by the collision process so that the fluorescence is quenched. The ratio of an unabsorbed and an absorbed signal, respectively, corresponds to a direct measurement of the atmospheric transmission of WV based on Beer's law, which can be uniquely inverted for deriving absolute humidity. Also here a range-resolved measurement can be performed.

The ground-based system on the right presents an IR spectrometer or an MWR measuring the thermal emission of the atmosphere along the line of sight. The collected atmospheric radiation is measured from all heights at the same time so that range information is not initially available. However, the spectrum contains information concerning T and trace gases such as WV at different frequencies simultaneously, which can be used for the retrieval of profiles.

The satellite system on the right shows the STD raypath of a GNSS. Both the phase delay and the bending of the beam are indicated and contain information concerning atmospheric temperature and humidity. As in

Figure 7. Passive and active remote sensing methodologies. Left ground-based system: Lidar system using the inelastic Raman scattering effect for water vapor and temperature measurements. In the scattering volume, a photon is absorbed by a molecule, e.g., water vapor, oxygen, or nitrogen, which is excited to an upper vibronic or rotational level. The wavelength of the scattered radiation is shifted to the red due to the energy gap between the initial and the final energy level after the transition. The backscattered radiation is measured in dependence of traveling time so that a range-resolved measurement is possible. Middle ground-based system: Differential absorption lidar using the absorption of water vapor for range-resolved absolute humidity measurements. The absorbed photon is lost and extracted from the incident radiation field of the laser. This energy is transferred to the environment by collision with the surrounding molecules. Also here a range-resolved measurement can be performed. Right ground-based system: IR spectrometer or MWR measuring the thermal emission of the atmosphere along the line of sight. The collected atmospheric radiation is measured simultaneously from all heights so that range information is not initially available and can only be determined by the difference signal strengths at different wavelengths that span a range of optical depths. Right satellite system: GNSS using the STD raypath. The phase delay and the bending of the beam are both indicated and contain information concerning atmospheric temperature and humidity. As in passive remote sensing, the transmitted signal contains integrated but not range-resolved information.

passive remote sensing, the transmitted signal contains integrated but not range-resolved information. This bending can be detected between different satellites leading to the RO method or by ground-based receivers for measuring STD and ZTD, which are indicated here.

5.1. Passive Remote Sensing, Current Performance, and Future Potential

Commonly used passive remote sensing systems are based on radiometers detecting the radiation of the MW and IR absorption lines produced by the electromagnetic field interactions of atmospheric molecules such as oxygen, WV, carbon dioxide, and nitrous oxide. Their absorption/emission properties are used to infer WV and T profiles, as well as liquid and ice cloud properties. An example is depicted in Figure 7 showing on the right a ground-based passive remote sensing system with the brown cone of atmospheric emission reaching the receiver.

The basic RTE can be derived either for the geometry and configuration of a spaceborne or a ground-based passive remote sensing system. Contrary to the ground-based passive sounding of the atmosphere at MW and IR wavelengths, which is done against the cold space background, the passive sounding from satellites has to cope with a warm background, due to the thermal emission of the Earth's surface. The sounding of WV in the lower troposphere needs a contrast between surface and atmospheric emissions to enable the

measurement of atmospheric constituents, which poses a general limitation to WV retrievals from space in the thermal IR. Under conditions where an atmospheric mean layer temperature is equal to the brightness temperature of the surface, any WV in that atmospheric layer will not be measurable from space. This is frequently the case for the ABL in the IR, where the surface emissivity is close to unity. The situation looks better in the MW region, where the surface emissivity is usually far from unity, particularly over oceans, thus allowing for good thermal contrast between the surface and the atmosphere. Vertical resolution and accuracy go hand in hand with spectral and radiometric resolution, and progress is being made to increase both for better ABL soundings. Furthermore, the degrees of freedom for signal in a passive sounding depend strongly on the prior knowledge that is used to constrain the retrieval of T and WV profiles. Due to these current limitations of spaceborne passive remote sensing, we are mainly focusing on the performance of ground-based systems.

The ground-based sounding principle is based on the fact that channels which are closer to the center of absorption lines are more opaque and therefore more sensitive to radiation from layers directly above the instrument, while channels located away from the center of the absorption line are more transparent and therefore can provide information on the upper atmospheric layers integrated over the viewing path. This effect results in sharper weighting functions in contrast to spaceborne observations.

Common ground-based MW radiometers use the absorption lines produced by the magnetic field interaction of the oxygen molecule between 50 and 60 GHz and at 118 GHz as well as the electric field interaction of the water molecule at 22.2 GHz and 183.3 GHz [*Askne and Skoog*, 1983; *Askne and Westwater*, 1986]. Ground-based thermal IR spectrometers, such as the Atmospheric Emitted Radiance Interferometer (AERI) [*Knuteson et al.*, 2004a, 2004b], are passive radiometers that measure downwelling IR radiation at relatively high spectral resolution between typically 3 and 18 μm in wavelength. A large number of different molecules have absorption bands in this spectral region, with the primary molecules being WV, carbon dioxide, ozone, methane, nitrous oxide, carbon monoxide, and chlorofluorocarbons. While the absorption bands of many of these gases overlap in the thermal IR portion of the spectrum, thus making the separation of the contributions of the differing gas concentrations more difficult, careful selection of the spectral regions used for profiling applications can minimize these challenges.

A ground-based radiometer detects the radiation power at a given frequency per unit area and per unit solid angle (radiance) coming from atmospheric layers above it. The contribution reaching the Earth's surface is expressed by equation (2).

It relates the radiance measured by the radiometer at a given frequency to the atmospheric temperature once we know the properties of the gas responsible for the absorption. Likewise, if the temperature profile is known, then the radiance observations can be used to infer the abundance of the atmospheric gases that are emitting the radiation.

If we define a transmittance

$$\Gamma_v(0, z) = \exp\left\{-\int_0^z \alpha_v(z')\, dz'\right\} = \exp\{-\tau_v(z, 0)\} \tag{6}$$

for a vertical pointing system, where z is height above ground level (agl), the term $\alpha_v(z)\exp\{-\tau_v(z, 0)\}$ in equation (2) can be written as $\partial\Gamma/\partial z$. This last term is sometime called the weighting function and expresses the contribution from each atmospheric layer to the emitted radiation.

Spectrally resolved, ground-based MW and IR radiometers provide radiance observations from which T and WV profiles can be derived. With MWRs, T profiles are commonly retrieved from observations of a complex set of pressured-broadened oxygen absorption lines between 50 and 60 GHz, and at 118 GHz; the primary assumption is that the oxygen concentration as a function of height is known and the observed MW radiance in this spectral region is due only to variations in T as a function of height. Low-resolution WV profiles are commonly retrieved from observations of the WV resonance line centered at 22.2 GHz. These retrievals need either to use an assumed T profile or to simultaneously retrieve both TD profiles using observations that span both the WV absorption line and the oxygen absorption band. Recently new ground-based radiometers have been developed that use the stronger WV line centered at 183.3 GHz. Measurements at this frequency can provide improved humidity profiles in very dry regions such as the Arctic [*Cadeddu et al.*, 2007; *Cimini et al.*, 2009].

In the IR, the most commonly used spectral regions for T profiling are the 4.3 and 15.0 μm carbon dioxide bands (observations are typically used from 4.1 to 4.6 μm, 12.9 to 16.4 μm). Recent research efforts have also used the N_2O band near 4.5 μm for temperature profiling [*Crevoisier et al.*, 2014]. Similar to retrievals that use MW observations, the concentration of carbon dioxide or nitrous oxide with height is assumed to be known. WV retrievals use observations in both the long wavelength side of the 6.3 μm v_2 absorption band and the short wavelength side of the rotational band (observations from 7.4 to 8.0 μm and 17.0 to 18.6 μm, respectively) [*Smith et al.*, 1999].

From equations (2) and (6) it can be seen that the information on the vertical profiles of T and WV can be retrieved from the measured radiance by inverting a Fredholm integral equation of the first kind. The difficulties associated with the inversion are related to the nonuniqueness of the solution and to the presence of measurement noise. As pointed out by *Rodgers* [2000], the problem of finding the exact solution is replaced by the problem of finding the best estimate of the solution from all possible solutions of the Fredholm equation. The retrieval stability is usually achieved with the introduction of "a priori" knowledge of the atmospheric state. This a priori information is used to constrain the possible solutions toward statistically and physically acceptable solutions. Prior information fed into the retrieval consists of a mean profile and an associated error covariance matrix [e.g., *Löhnert et al.*, 2009; *Turner and Löhnert*, 2014], which is a crucial part of the retrieval process.

Usually a variational retrieval based on optimal estimation theory [*Rodgers*, 2000] is applied starting from a first guess and prescribing a background to constrain the subsequent iteration. In many instances both in the MW and IR range, the Levenberg-Marquardt technique is used to control the algorithm convergence. A cost function is minimized to achieve convergence according to specified criteria. The advantage of using variational retrievals is that the final retrieval product is accompanied by the computation of a posterior error covariance matrix or an averaging kernel matrix that provides information how much the measurement contributes to the retrieval. This information can be used, for example, to optimize the viewing/scanning geometry. Variational retrievals have been used, for example, in *Löhnert et al.* [2008], *Cimini et al.* [2010], and *Turner and Löhnert* [2014].

Based on these considerations, the following expectations with respect to bias and RMS errors can be derived focusing on variational retrievals. Variational retrieval methods are bias blind due to their design to correct random errors only, as pointed out by *Dee* [2005]. The posterior error covariance matrix $\boldsymbol{A}$ resulting from errors in the background and in the observations also includes errors in the observation operators used in the retrieval and reads

$$\boldsymbol{A} = \left(\boldsymbol{K}^T \boldsymbol{R}^{-1} \boldsymbol{K} + \boldsymbol{B}^{-1} \right)^{-1} \tag{7}$$

similar to the 3-DVAR analysis of an initial field in NWP DA in equation (5). Obviously, this analysis can be used to estimate the RMS error of the retrieval. Here $\boldsymbol{B}$ is the covariance of the a priori information, $\boldsymbol{K}$ is a matrix of weighting functions, and $\boldsymbol{R}$ is the measurement noise covariance. The first-guess profile is used neither in the computation of the RMS error nor in the posterior covariance.

This approach is valid, if both the first guess database and the observed radiances are bias free. Otherwise, any biases in the background, the observation, or the observation operator are linearly propagated through the variational retrieval. Additionally, situation-dependent biases can be introduced:

1. In case of a global background with related global covariance, any regional retrieval distant from the global mean will be biased toward the global mean. Similarly, seasonally varying biases can be introduced.
2. Observation operators consist of Fréchet derivatives of fast radiative transfer models. These are often truncated in not fully representing all variability in the radiance field due to precipitation, clouds, or aerosols. Correspondingly, biases will occur in situations where they are not properly detected.

While biases in the observations are usually well measured and can be corrected, the characterization of biases due to the background and the observation operators requires more effort. The error covariance matrix should give reasonable estimates of RMS errors, which, however, may be misinterpreted by undetected biases in the retrievals. Furthermore, the quality of RMS error determination depends critically on a reasonable choice of the a priori data set and the estimation of its background errors. Therefore, it is essential to study the combination of bias and RMS errors by extensive intercomparisons with coincident high-quality atmospheric profiles such as from radiosondes or accurate active remote sensing systems.
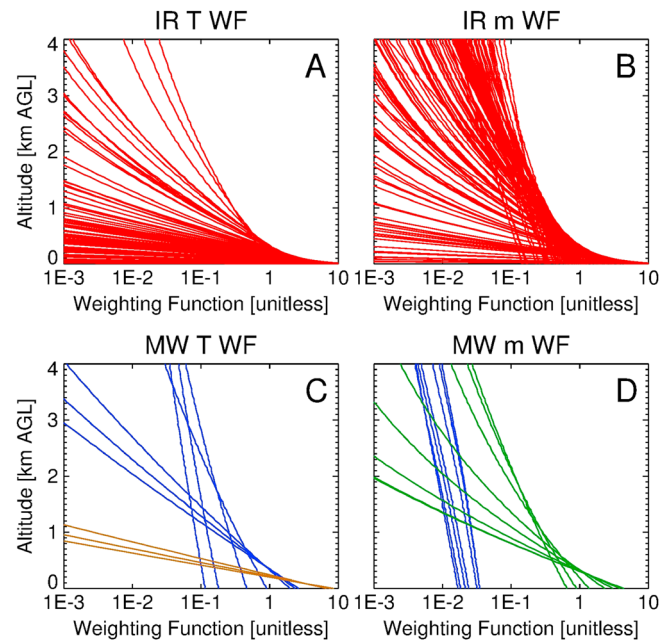
Figure 8. Weighting functions for typical zenith-pointing (a and b) IR spectrometers and (c and d) MWRs in dependence of altitude agl. These weighting functions were computed with radiative transfer models using the U.S. Standard Atmosphere as input. The IR radiometer has spectral channels in the 612–713 cm^{-1} band for T (Figure 8a), and 538–588 cm^{-1} and 1250–1350 cm^{-1} bands for WV (Figure 8b). The MWR used channels from 52–58 GHz for T (Figure 8c), and 22–31 GHz and 174–183.3 GHz for WV (Figure 8d), where channels in the latter band are indicated in green. MWRs are often scanned in elevation, and observations at the most opaque temperature channels are added to the zenith observations from all channels to improve the T retrieval. The brown lines in Figure 8c show the weighting functions that result when a scan of 15° above the horizon is included.

With respect to the resolution of the retrievals, the vertical information content of passive spectral observations depends strongly on the prior data set used to constrain the retrieval algorithm as well. Generally, the information that can be extracted from passive soundings is increasing with the quality of the background information. For TD profiles in clear-sky conditions, the IR information content is typically 2–3 times larger than in MW observations [*Löhnert et al.*, 2009]. This is due to the larger number of spectral channels, which cover a larger range of weighting functions in the IR versus the MW. The *Löhnert et al.* [2009] result applies for commonly available instruments like the Humidity and Temperature PROfiler (HATPRO) MWR [*Rose et al.*, 2005] and the AERI [*Knuteson et al.*, 2004b]; however, changes in the spectral resolution and number of view angles used in the retrieval can impact the information content. Nonetheless, in general, the IR spectrometer has higher information content than the MWR because the former is able to observe hundreds of absorption lines of varying optical depths that provides a larger number of unique weighting functions, which adds both additional information and helps the algorithm account for uncorrelated random error. However, the occurrence of clouds limits the performance of pure IR retrievals and MW soundings become more important. Therefore, IR and MW soundings are often combined in variational retrievals to cope with varying cloudiness and in order to extract and combine maximum information from both systems.

In the following, we are substantiating the performance of passive remote sensing retrievals by recent observations and analyses. Figure 8 presents an overview of the widths of weighting functions for a variety of channels available for IR spectrometers and MWR. Figures 8a and 8b show the width of the weighting functions in dependence of height for T (Figures 8a and 8c) and WV (Figures 8b and 8d) profiling using the IR. Figures 8c and 8d present the results for the MW. The vertical resolution of the profiles depends on the weighting functions that decay with altitude as shown in Figure 8. In spectral channels that have strong absorption, the weighting function decreases rapidly with height; however, the weighting function decreases more slowly with height in more transparent channels. Therefore, the resolution is highest near the surface and in the first few hundreds of meters and rapidly degrades with height. Typical resolution of T profiles retrieved from a ground-based MWR is a few 100 m in the first few hundreds of meters degrading to approximately 1 km above the first kilometer [*Westwater and Strand*, 1968; *Cadeddu et al.*, 2002], whereas WV profiles typically have resolutions of 500 m in the boundary layer degrading to 1 km above. Close to the surface, the vertical resolution of the T profiles retrieved from MWRs can be improved to ≈100 m by scanning low-elevation angles [*Kadygrov and Pick*, 1998; *Crewell and Löhnert*, 2007], which adds extra information to the retrieval (e.g., see the brown lines in Figure 8c).

As the IR spectrometer has much more channels than the MWR and as these channels sample strongly absorbing lines, there is a much higher number of weighting functions of various strengths (Figures 8a
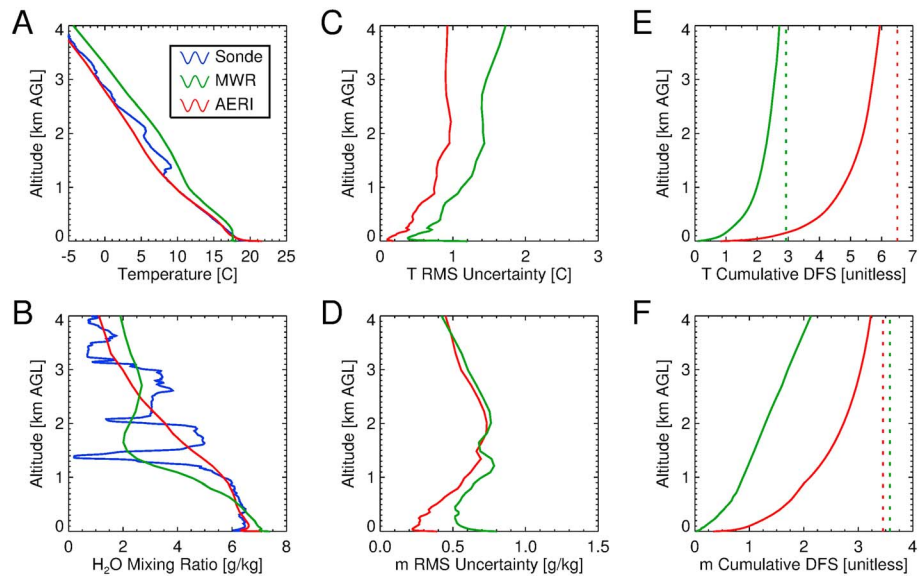
Figure 9. A comparison of MWR-retrieved (green) and AERI-retrieved (red) profiles of (a) T and (b) WV. The MWR and AERI observations were simulated using a radiative transfer model using the radiosonde-observed profile of temperature and humidity (blue) as input. The radiosonde observation occurred at 11:30 UTC on 21 September 2007 during the ARM Mobile Facility deployment in the Black Forest in southwest Germany. This example is indicative of the accuracy and information content of a retrieval, if the instrument is perfectly calibrated and there are no spectroscopic issues with the radiative transfer model. Both retrievals used the same optimal estimation-based framework as described in *Turner and Löhnert* [2014], using a prior data set derived from radiosonde profiles observed at the ARM site for a 9 month period. (c, d) The 1σ uncertainties and (e, f) the cumulative degrees of freedom of signal profiles, which are natural outputs from the optimal estimation technique, for both retrievals are also shown.

and 8b). This greatly improves the vertical resolution of retrieved T and WV profiles using IR observations, from order of 10–20 m and 50–100 m for T and WV, respectively, in the lowest few hundreds of meters of the atmosphere. However, like the MW retrieval, the vertical resolution decreases with height to about 1 km at the ABL top, albeit not quite as fast as the MW retrieval.

Typical temporal resolutions of vertical profiles from MW and IR radiometers are 5 min or better, depending on the frequency of calibration, integration time, and scanning sequence. Attempts to resolve turbulence at temporal resolutions of $\approx$10 s have not been successful yet and are likely not possible due to the increase of the bias and RMS errors [*Kalthoff et al.*, 2013].

Figure 9 shows a comparison of T and WV profiles retrieved from simulated MW and IR measurements. The simulated measurements were used to illustrate the maximum information content and accuracy that would result if all spectral channels had been used in the retrieval. This could be done because in this simulation we have assumed that the spectroscopy in the forward model is perfect and that the instrument is well calibrated. In this example and the one that follows, both the IR and the MW retrievals use the framework of *Turner and Löhnert* [2014], which allows for the same prior information to be used in both the MW and IR retrieval and thus permits a more equitable comparison to be made. This example assumes that the MWR made observations in the 22–31 GHz, 51–58 GHz, and 174–183.3 GHz regions— this is the equivalent to collocating a HATPRO [*Rose et al.*, 2005] and a G-band radiometer [e.g., *Cimini et al.*, 2009] side by side. The IR instrument made T observations in the 612–713 cm^{-1} band, and WV observations in the 538–588 and 1250–1350 cm^{-1} bands [*Feltz et al.*, 1998]. In this case of simulated observations, neither the AERI nor the MWR resolve the small elevated inversions aloft (Figure 9a); however, the AERI is more accurate in the lowest 1 km because of its additional information (Figures 9c and 9d), as expected from Figure 8, Figures 9a and 9b, by the larger number of weighting functions in this altitude range.

The distribution of information content as a function of height is illustrated in the profiles of cumulative degrees of freedom (DFS, Figures 9e and 9f), which shows that the AERI has nearly 5 DFS for T in the lowest
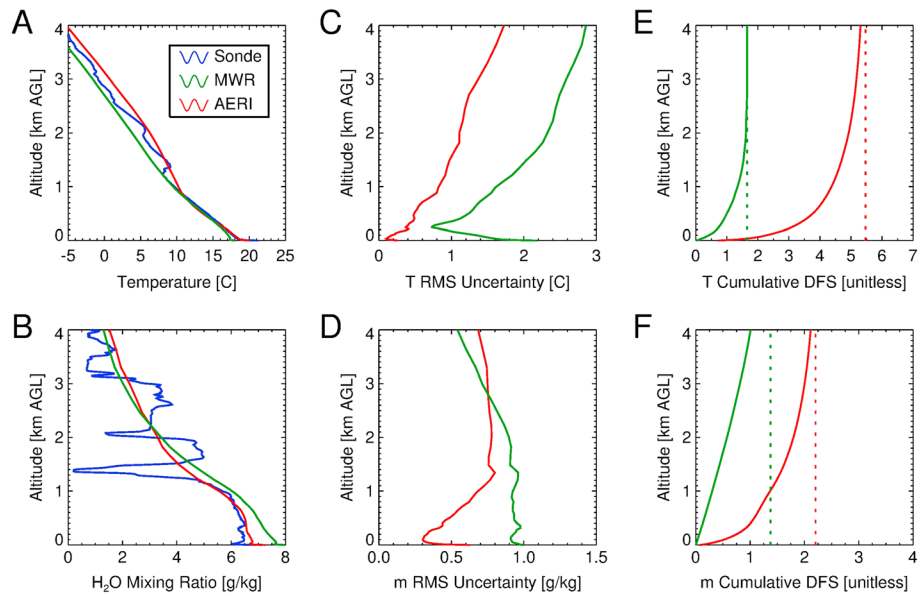
Figure 10. Similar to Figure 9, but using real AERI and MWR observations that were collected simultaneously with the radiosonde data in the Black Forest. Due to calibration and/or forward model inconsistencies, both the MWR and the AERI used only a subset of the frequencies used in the simulated observation example in Figure 9. See text for more details.

1 km, while the MWR has only 2 DFS even though additional elevation angles at 10, 20, 30, and 42° are included in the retrieval. The additional information results in the AERI's 1 sigma uncertainty being smaller than the MWRs at all altitudes (Figures 9c and 9d). The AERI also does a better job capturing the structure of WV in the lowest 1 km (Figure 9b); however, the MWR (using both 22–30 and 174–183 GHz channels) does a better job aloft. This is supported by the AERI having a smaller 1 sigma uncertainty than the MWR in the first kilometers but they are virtually the same above that (Figure 9d). Furthermore, the DFS profiles (Figures 9e and 9f) demonstrate that the AERI's information content for *T* and WV drops off relatively quickly with height, with nearly 90% of its total information in the lowest 4 km, whereas the MWR still has a significant amount of information in its data above 4 km.

However, in reality, there are uncertainties in both the forward model used in the retrieval and in the calibration of the instrument, and thus not all spectral channels are currently used. Figure 10 shows an example where real measurements from a MWR and AERI were used to retrieve the TD profiles. The observations were collected by a colocated HATPRO and AERI instrument that were deployed in the Black Forest region of southwestern Germany during COPS [*Wulfmeyer et al.*, 2011]. Due to inconsistencies in the calibration, the only MWR channels used were the 22–31 GHz and 56–58 GHz channels, although elevation data at 10, 20, 30, and 42° elevation from the latter band were included in the retrievals. Similarly, due to spectroscopic inconsistencies, only the 538–588 cm^{-1} and the 612–713 cm^{-1} bands were used from the AERI for the IR retrievals. Comparing the results from Figures 10, which used real observations, and 9, which used simulated observations (with similar viewing angles and noise levels), illustrates the impact on both the retrieval accuracy and information content when spectral channels are removed from the retrieval. The most obvious change is the decrease in the DFS (Figures 10e and 10f compared to Figures 9e and 9f), which results in an increase in the 1 sigma uncertainties (Figures 10c and 10d compared to Figures 9c and 9d). However, there is also an impact in the accuracy of the retrieved profile, especially aloft. This example illustrates behavior that is commonly seen when the spectral information used in the retrieval, and hence the information content, changes. The exact impact will depend on the atmospheric conditions, the prior data set used to constrain the retrieval, and the instrument characteristics (e.g., number of spectral channels, center frequency and band pass of each channel, noise levels, and scan angles).

Overviews of resulting RMS errors of radiometric retrievals have been discussed in several papers. These errors include noise not only in the detection of the signals but also in the retrieval. Generally, the performance of the retrievals will vary based on the environment and the calibration of the instrument. *Liljegren* [2004] reported a
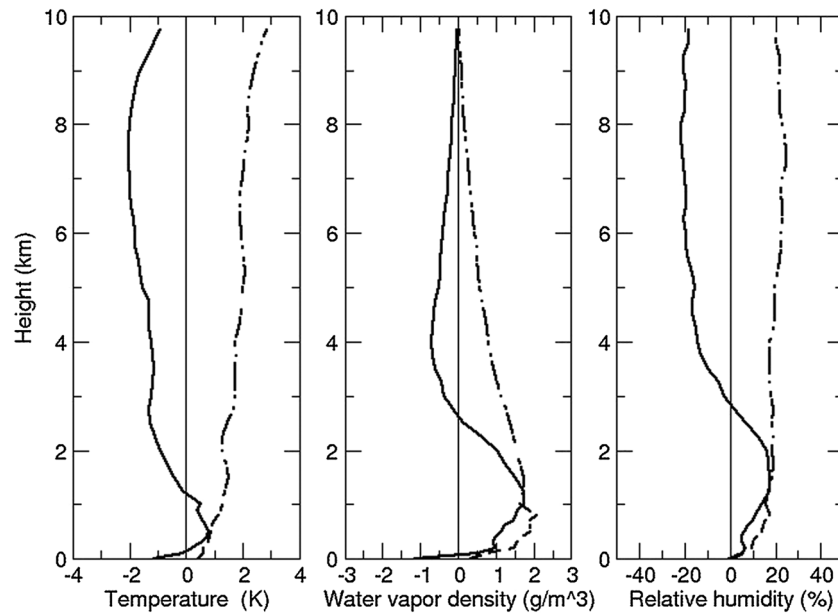
Figure 11. Mean bias (solid line) and standard deviation (dashed line) of the differences between MWR retrieved and radiosonde-measured profiles of temperature, absolute humidity, and relative humidity ($N = 112$). Data were collected in Graciosa Island (Azores) during a deployment of the ARM mobile facility in 2012 [from *Cadeddu et al.*, 2013].

maximum bias (standard deviation) of 1 (2) K for T and a bias (standard deviation) of less than 0.5 (1.5) g m^{-3} for humidity profiles using statistical retrievals (in the MW) at the SGP site in Oklahoma. The largest biases were reported between 0 and 1 km height. *Löhnert and Maier* [2012] retrieved T profiles from MW measurements with a statistical retrieval and reported an overall bias (standard deviation) of better than 0.5 (1.5) K throughout the profiles in Payerne, Switzerland from 3 years of observations. At different latitudes, *Cimini et al.* [2010] using a 1-D variational technique in the Arctic obtained a bias (standard deviation) of ≈ 1 (1) K for temperature and of 0.05 (0.1) g kg^{-1} for mixing ratio throughout the profile. An example of typical biases and RMS errors, obtained from operational MWRs at one of the ARM sites, is shown in Figure 11.

Although MWRs do not provide the highest vertical resolutions, they can achieve an acceptable compromise between cost/maintenance and the need for TD profiling with high temporal and low spatial resolution. They can provide continuous operations in a variety of weather conditions, and together with the vertical profiles, they also provide accurate estimates of integrated WV and liquid water. Recent simulations [*Steinke et al.*, 2014; *Meunier et al.*, 2015] show that 2-D tomography of WV can also be applied by combining several radiometers scanning in azimuth and elevation. However, the vertical resolution and accuracy will remain low due to the coarse information content in the signals.

Both the MW and IR techniques are sensitive to clouds in their fields of view. For many years, the MWR community has been able to simultaneously retrieve TD profiles and cloud properties [e.g., *Löhnert et al.*, 2004; *Löhnert et al.*, 2007; *Löhnert et al.*, 2008]. The ground-based IR technique was primarily limited to scenes when there was no cloud above the spectrometer [e.g., *Feltz et al.*, 2003], but a recently developed algorithm now allows TD profiles and cloud properties to be retrieved from ground-based IR spectrometers simultaneously [*Turner and Löhnert*, 2014]. A comparison of the accuracy of the AERI-retrieved temperature and humidity in clear skies over Norman, Oklahoma, USA, is shown in Figure 12 (top row), whereas a similar comparison in cloudy scenes is shown in Figure 12 (bottom row). For both cases, the T bias is ≈ 0.5 K in the lower troposphere and the RMS error < 1 K for cloud-free cases and < 2 K for cloud-covered cases, respectively. The corresponding WV bias is < 0.5 g kg^{-1} and < 0.8 g kg^{-1} whereas the RMS errors are ≈ 1 g kg^{-1}, respectively.

5.2. Active Remote Sensing, Current Performance, and Future Potential

Active remote sensing systems, which are transmitting a well-defined spectrum, can either measure range-resolved backscatter signals using time-of-flight analyses (lidar or radar), transmission (DOAS),
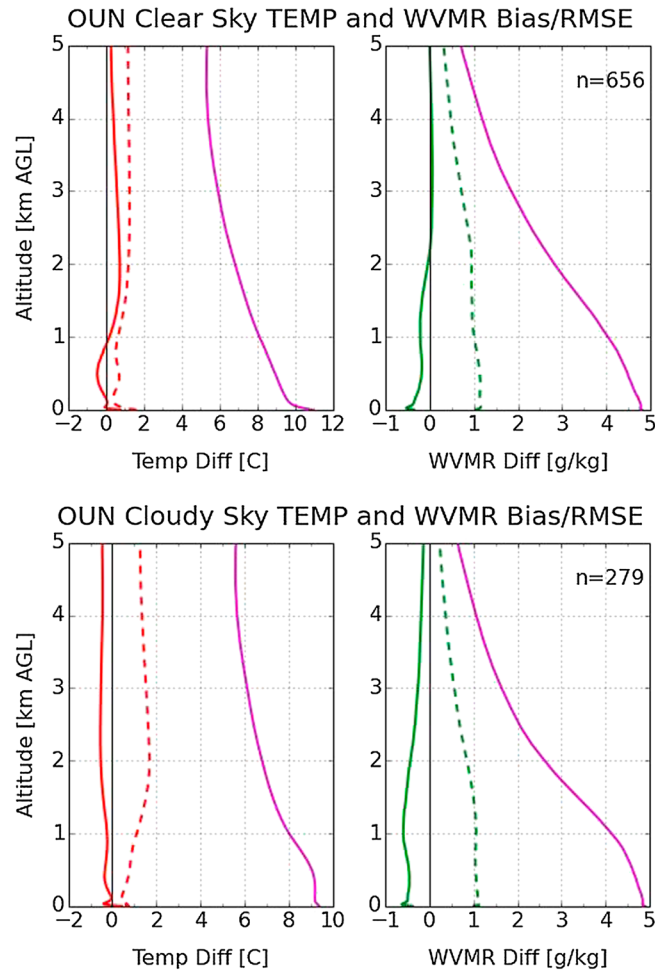
Figure 12. (top row) A comparison of AERI-retrieved (left) temperature and (right) water vapor mixing ratio with collocated radiosondes at Norman, Oklahoma, for data collected in clear-sky scenes in 2012–2013 using the algorithm by *Turner and Löhnert* [2014]. The solid red and green lines denote the bias (AERI minus sonde), while the dashed lines denote the RMS difference between them. The solid purple lines show the standard deviation of the radiosonde data from the mean conditions, which is essentially the uncertainty in the prior data set used in the retrieval. (bottom row) Same as Figure 12 (top row) but for cases where there is a cloud in the field of view of the AERI.

or phase delays of transmission (GNSS). We are considering techniques, which demonstrated quasi-operational performance and have the potential to derive or to retrieve TD profiles.

5.2.1. Radio Detection and Ranging

One field of investigation from the late 1980s and early 2000s was the promise of TD profiling with radar wind profilers. Ways to retrieve tropospheric temperature and in particular humidity profiles with the same high time and height resolution under all weather conditions as wind profile have been proposed.

For temperature, RASS have been developed where sound waves are sent out and tracked by the radar [*Matuura et al.*, 1986; *Tsuda et al.*, 1989; *Neiman et al.*, 1992; *Martner et al.*, 1993]. By measuring the propagation speed of sound as it travels upward in the atmosphere, it is possible to retrieve the virtual temperature profile, as the speed of sound is a function of it. For optimum backscatter, the acoustic waves usually span a range of frequencies such that their wavelengths at the various altitudes and temperatures covered will correspond to one half of the wind profiler electromagnetic wavelength. However, this technique suffers from poor altitude coverage at times, especially when high horizontal winds carry the sound waves outside of the radar beam, while particular care must also be provided to vertical wind and turbulence perturbations to the sound Doppler measurements [*Angevine and Ecklund*, 1994; *Angevine et al.*, 1994]. Nonetheless, RASS proved useful for boundary layer virtual temperature profiling. Typically, a T bias of < 1 K with a

noise error of < 0.5 K can be achieved with resolutions of 60 m and 10 min, respectively [*Wulfmeyer*, 1999a]. The range depends on the strength of the horizontal wind and the choice of ultrahigh or very high frequencies (UHF and VHF). Usually ranges of a few 100 m with 100 m resolution (UHF) or a few kilometers with 300 m resolutions (VHF) can be reached with errors of approximately 1 K. An important limitation is the emission of strong sound waves, which prevent the continuous operation of these systems in urban environments. RASS is typically used only during the daytime and equipped with a random phase flipping of the acoustic signal creating an acoustic signal that resembles white noise. Therefore, it is difficult to apply radar-RASS for routine operation in mesoscale networks.

Considering WV profiling with wind profilers, several studies have shown the possibility to estimate the humidity profile or at least ways to improve its measurement through a combined instrumentation approach [*Stankov et al.*, 1996; *Gossard et al.*, 1999; *Tsuda et al.*, 2001; *Furumoto et al.*, 2003; *Stankov et al.*, 2003]. The relevant variable extracted from the radar signal is the vertical profile of either the refractivity index

gradient [*Tsuda et al.*, 2001] or the potential refractive index [*Stankov et al.*, 2003]. In any case, the method consists in solving the humidity equation in the following form [*Tsuda et al.*, 2001]

$$q(z) = \theta^2 \left[\int_{z_0}^{z} \left(1.652 \frac{Pa}{K^2} \frac{T^2}{p} C + \frac{T}{7800\,K} \frac{v_B^2}{g} \right) \frac{1}{\theta^2}\, dz + \frac{q_0}{\theta_0^2} \right].$$
(8)

Here C is the refractive index gradient (in m^{-1}) and v_B is the Brunt-Vaisälä frequency. The specific humidity and the potential temperature at the boundary height are denoted with q_0 and θ_0, respectively. This humidity equation can only be solved when the temperature and the refractive index gradient profiles are known as well as the ground pressure and temperature, and humidity at a given range or over a given layer of the atmosphere. Although, as we have seen above, the wind profiler equipped with a RASS capability could provide the T profile, it is often limited in range; hence, the need for a combined instrumentation approach using, for example, a closely located MWR [*Klaus et al.*, 2006]. Furthermore, as only the absolute value of C can be determined using the radar Doppler spectrum, a sign ambiguity remains in equation (8) above. Indeed, C can become positive in 10 to 20% of the cases, but in most situations its sign changes with height has shown good correlation with v_B^2 becoming positive when v_B^2 is less than a given threshold [*Tsuda et al.*, 2001]. However, this rule might no longer be valid when horizontal advection becomes important [*Mapes and Zuidema*, 1996]. Hence, to alleviate this assumption, as well as to relax the radar calibration and the constant scale of turbulence with altitude constraints, further reference data on humidity should be used, such as the humidity at specific altitudes (usually zero at tropopause level or measurements at other available levels) or the humidity content over some vertical extent, e.g., by GNSS derived IWV.

As we have seen, wind profilers have the theoretical potential for TD profiling. Nonetheless, to be considered as key instruments for TD profiling for operational purposes and given the current state of the art in that field, they rely on too many assumptions and need supporting measurements, often from collocated instruments that can provide useful profile information themselves.

5.2.2. Global Navigation Satellite System

When GNSS signals propagate through the Earth's atmosphere, they are affected in a characteristic way due to the presence of matter in the atmosphere. The phase measurements by a receiver allow for estimating the signal travel time delays caused by the neutral atmosphere. These time delays for a station-satellite link depend on the atmospheric refractivity, which is a function of pressure, temperature, and humidity and is the basic observable in GNSS meteorology [*Bevis et al.*, 1992].

In a GPS RO event, the signals are received aboard an LEO satellite. A bending angle profile is derived, which can be inverted to the refractivity and (dry) T profile under the assumption of spherical symmetry [*Ware et al.*, 1996; *Kursinski et al.*, 1997; *Anthes*, 2011]. The refractivity profile $N(z)$ can be expressed by

$$N(z) = 0.776 \frac{K}{Pa} \frac{p(z)}{T(z)} + 6 \frac{K^2\,kg}{Pa\,g} \frac{m(z)\,p(z)}{T^2(z)}$$
(9)

where we neglected higher-order terms of the mixing ratio m. Therefore, a retrieval of m (in this equation given in $g\,kg^{-1}$) is only possible with additional information with respect to T and p. The vertical resolution is $\approx 100\,m$, and the horizontal footprint $\approx 100\,km$.

For DA, an inversion of equation (9) is not useful; either N or the bending angle are directly assimilated. This limb sounding technique provides very valuable input for NWP in the lower stratosphere down to the middle troposphere [*Wickert et al.*, 2004; *Cardinali and Healy*, 2014]. Therefore, the RO data are assimilated operationally at several NWP centers around the world, e.g., at ECMWF, UK Met Office, Météo-France, the National Center for Environmental Prediction (NCEP), the Japanese Meteorological Agency (JMA), and DWD (see section 2.5).

In the lower troposphere, the RO data are less accurate due to strong horizontal and vertical refractivity gradients. First, the bending angle (refractivity) profiles are derived under the assumption of a spherically layered atmosphere. Second, large bending angles due to strong vertical refractivity gradients must be retrieved from weak signals. Third, if the vertical refractivity gradient exceeds the critical refraction ($dN/dz < -160$ N-units km^{-1}), the retrieved refractivity is negatively biased by several percent [e.g., *Sokolovskiy*, 2001; *Xie et al.*, 2006; *Ao et al.*, 2009]. This effect often results from the combination of a sharp vertical gradient in moisture and a temperature

inversion frequently observed at the top of the ABL. Nevertheless, numerous studies have shown the feasibility of the RO technique to detect the ABL height [e.g., *Sokolovskiy et al.*, 2006; *Guo et al.*, 2011; *Ao et al.*, 2012]. With respect to the potential to observe TD profiles in the lower troposphere, RO retrievals are used in many regions down to 1 km [*Vergados et al.*, 2014, 2015].

Separate WV profiles are obtained from the retrieved refractivity and auxiliary temperature data (e.g., *T* from a global NWP analysis). Using equation (9) and assuming independent errors in *T*, *p*, and *N* the systematic error in mixing ratio can be estimated by

$$\Delta m \cong \sqrt{\left(m\frac{\text{kg}}{\text{g}} + 0.129\frac{T}{\text{K}}\right)^2\left[\frac{\Delta_N^2}{N^2} + \frac{\Delta_p^2}{p^2}\right] + \left(2m\frac{\text{kg}}{\text{g}} + 0.129\frac{T}{\text{K}}\right)^2\frac{\Delta_T^2}{T^2}}, \tag{10}$$

where *m* has to be inserted in g kg^{-1}. For instance, assuming a relative error of 3% for *N* and 2 K for *T*, the absolute error Δm increases nearly linearly from 1 to $2.5\,\text{g kg}^{-1}$ for *m* increasing from 5 to $30\,\text{g kg}^{-1}$. Further details are presented in *Kursinski and Hajj* [2001], *Sokolovskiy et al.* [2010], *Vergados et al.* [2014, 2015] where also the potential of these data to study WV on the global scale was highlighted. Further studies are required in the moist tropical troposphere below the ABL top (altitudes < 3 km) where the retrieved refractivity may be subject of further constraints due to critical refraction [*Xie et al.*, 2012]. Additionally, over the inhomogeneous land surface, it is not clear how to interpret a horizontal average of WV and/or *T* over hundreds of kilometers in the ABL. With regards to the use of GNSS to sense the small-scale variability of water vapor in the lower troposphere, in the following we are focusing on GNSS ZTD and STD observations.

The configuration of the GNSS measurement using a ground-based receiver measuring ZTDs or STDs is depicted on the right-hand side in Figure 7. Each GNSS satellite continuously transmits radio signals at two frequencies ($\nu_1 = 1575.42\,\text{MHz}$ and $\nu_2 = 1227.6\,\text{MHz}$). The observation equation of the carrier phase length L_{GNSS} can be written as [*Hoffmann-Wellenhof et al.*, 1992]

$$L_{\text{GNSS}} = l_{\text{GNSS}} + c\,(t_r - t_s) + n\lambda - I + \text{STD} + \varepsilon, \tag{11}$$

where l_{GNSS} denotes the geometric distance between the transmitter and the receiver, *c* is speed of light, t_s and t_r are the clock errors of the transmitter and the receiver, respectively, *n* is the integer ambiguity, λ is the wavelength, *I* is the ionospheric delay, and ε denotes measurement noise and multipath.

The signal travel time delay due to the neutral atmosphere, also known as STD, consists of a hydrostatic and nonhydrostatic component. In GNSS processing, the STD is approximated through

$$\text{STD} = M_h(\text{el})\,\text{ZHD} + M_w(\text{el})\{\text{ZWD} + \cot(\text{el})[G_n\cos(\text{az}) + G_e\sin(\text{az})]\} + \text{PoR}, \tag{12}$$

where el and az denote the elevation and azimuth angles of the station satellite link. The hydrostatic and nonhydrostatic mapping function M_h and M_w are based on a climatology [*Boehm et al.*, 2006] but also NWP fields can be taken. The zenith hydrostatic delay ZHD is computed using the Saastamoinen model [*Davis et al.*, 1985]. The zenith nonhydrostatic delay ZWD and the gradients in north and east direction G_n and G_e [*Davis et al.*, 1993] are estimated by a least squares adjustment. The postfit residual PoR takes into account the error of the parameterization in the least squares adjustment. The Zenith Total Delay (ZTD) is the sum of the zenith hydrostatic and nonhydrostatic delays.

At the Geoforschungszentrum (GFZ) in Potsdam, Germany, the Earth Parameter and Orbit determination System (EPOS) software [*Gendt et al.*, 2004] is used to estimate ZTD and STD. Once the ZTD is estimated, ZHD is subtracted to obtain the zenith nonhydrostatic delay which is directly related to the IWV [*Bevis et al.*, 1992] by

$$\text{IWV} = \Pi(T_m)\,\text{ZWD}. \tag{13}$$

Here Π depends on the atmospheric mean temperature T_m that is calculated from surface meteorological measurements. Currently, data of ≈300 stations in Germany are analyzed hourly at GFZ, and ZTD and IWV products are available with a delay of 30 min.

As shown in section 2.1, IWV can easily be transformed to PW. The bias error in GNSS PW appears to be less than 1 mm with an overall error of less than 5% under moist, tropical conditions. This estimate is based on comparisons with Very Long Baseline Interferometry, radiosonde, MWR, and lidar data [*Li et al.*, 2003;
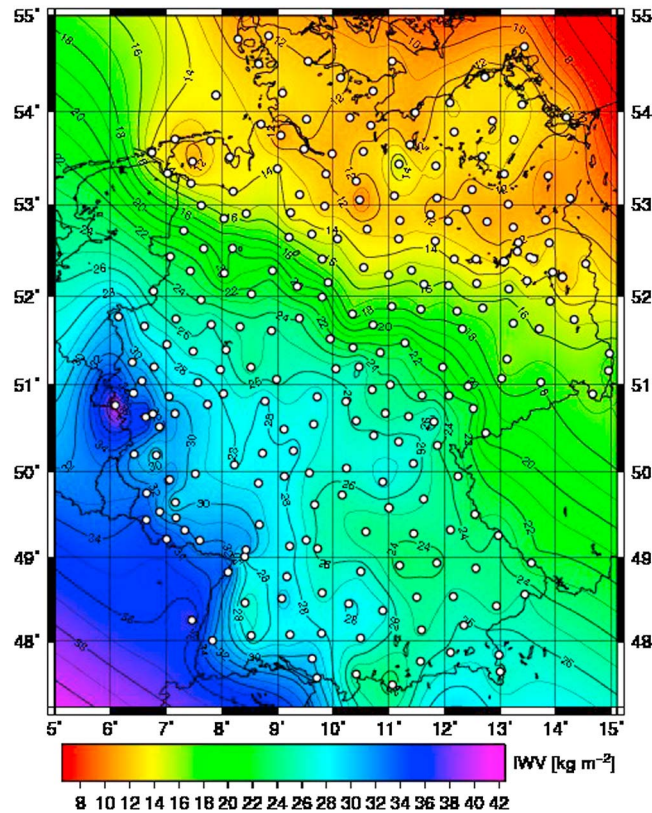
Figure 13. GNSS IWV map on 3 June 2012 at 12 UTC. White dots indicate the location of the ground-based stations.

Gendt et al., 2004; van Baelen et al., 2005; Teke et al., 2011; Ciesielski et al., 2014; Leblanc et al., 2011]. Hence, the IWV is recoverable with a random error of less than 1 mm and biases of less than 1 mm. This corresponds to a relative error in absolute humidity of 5% in a 2 km deep ABL with an absolute humidity of $10\,\mathrm{g\,m^{-3}}$, if the error comes from the ABL WV estimate only.

An example of an IWV map is shown in Figure 13. These maps are available with a temporal resolution of 15 min. The ZTD data are now assimilated operationally by several European NWP centers. Though they have some slight positive impact on the prediction skills, they are clearly of limited value as they do not contain information about horizontal (and vertical) refractivity gradients in the vicinity of a station.

The STDs contain additional information. Figure 14 shows the gradient in north and east direction estimated from artificial STDs (top) and real STDs (bottom). The artificial STDs were generated by point-to-point ray tracing [*Zus et al., 2012*] utilizing a NWP refractivity field (in this case a short range forecast of the Global Forecasting System). It is obvious that STDs carry the signature of the tropospheric asymmetry. Therefore, they are considered a valuable additional information source for NWP models [*Brenot et al., 2014*].

Whenever a dense network of GNSS stations is available, tomography is another way to make use of the information contained in the STDs, i.e., the particular delays along the line of site between the individual GNSS stations and the satellites in view at any given moment. To do so, the atmospheric volume above the network is partitioned into boxes, usually called voxels (standing for VOlume piXELs), while the various interleaving transmission rays between the GNSS stations and the satellites are distributed within those voxels which they cross. Likewise, as it is WV content, which is the desired estimate, the STDs are usually transformed into slant integrated WV (SIWV) before performing tomography. This step requests the knowledge of the pressure field and the atmospheric temperature in order to subtract the hydrostatic component of the slant delay and then the conversion of the retrieved slant wet delay into the water vapor content along the path.

Then, the tomography problem reduces to the inversion of the following equation:

$$d = \boldsymbol{G}\,\rho_{\mathrm{WV}}, \tag{14}$$

where d corresponds to the GNSS data available (i.e., the SIWVs), $\boldsymbol{G}$ is a length partitioning matrix of the receiver-to-satellite rays into the different voxels, i.e., our model, and ρ_{WV} corresponds to the water vapor density distribution, i.e., our result. The solution to this inverse problem is often given through a weighted least squares fit [*Menke*, 1989; *Tarantola*, 2005] according to

$$\rho_{\mathrm{est}} = \rho_0 + \left[\boldsymbol{G}^T\,\boldsymbol{W}_{\mathrm{GNSS}}\,\boldsymbol{G} + \mu\,\boldsymbol{B}\right] - \boldsymbol{G}^T\boldsymbol{W}_{\mathrm{GNSS}}\,[d - \boldsymbol{G}\rho_0], \tag{15}$$

where ρ_{est} is the estimated absolute humidity in each of the voxels of the domain and ρ_0 is an a priori solution or first guess. $\boldsymbol{W}_{\mathrm{GNSS}}$ corresponds to the inverse of the variance/covariance matrix of the data errors: $\boldsymbol{W}_{\mathrm{GNSS}} = \boldsymbol{R}_{\mathrm{GNSS}}{}^{-1}$, $\boldsymbol{B}$ is the model error background matrix of the a priori values, and μ is a weighting coefficient.
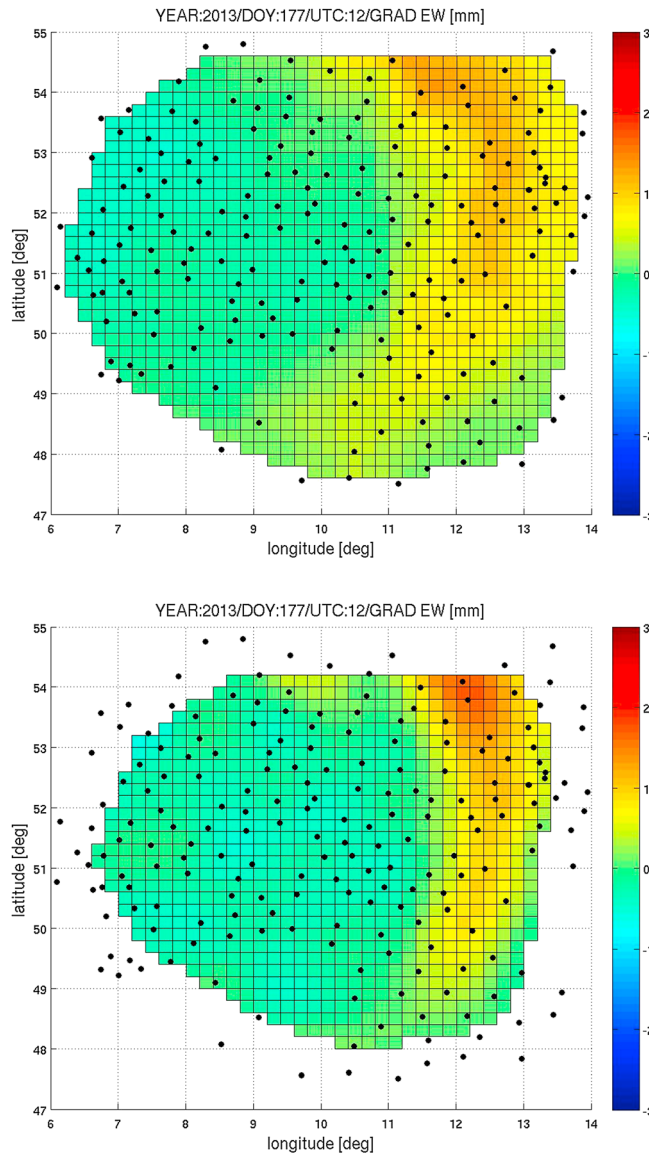
Figure 14. The gradients in east direction (mm) derived from (top) the NWP model and (bottom) the GNSS. The gradient at a specific station (black dot) represents the tropospheric asymmetry in the vicinity of that station.

Prerequisites for an accurate solution are the adequate distribution of rays within the different voxels, as well as a reasonable choice of the initial "first guess" solution ρ_0. This can be done with only the IWV retrieved at the network GNSS stations and accordingly adjusted standard atmospheric profiles [*Reverdy et al.*, 2009; *Van Baelen et al.*, 2011], complementary measurements such as radiosondes [*Champollion et al.*, 2005], MWRs [*MacDonald et al.*, 2002], and lidar systems, or by making use of model outputs available over the domain in order to introduce some trends of vertical resolution. Another difficult aspect of the inverse problem is the quantification of the variance/covariances matrices, as well as the weighting coefficient μ as, in theory, it allows putting more weight on either the data or the initial guess. Thus, this latter parameter is a quite sensitive matter and can produce singularities (i.e., nonphysical solutions due to numerical instabilities) as the tomography inversion problem is often largely underdetermined and must usually account for a large number of "empty" voxels, i.e., voxels with no ray crossing. Hence, the resolution that can be achieved by GNSS tomography is largely dictated by the network density and geometry. Particularly, one must consider that with a cutoff angle of 5° for the lowest elevations, most of the atmospheric WV below 2 to 3 km, which is a typical scale height, is seen under a cone where the lines of sight reach distances of 16 to 24 km from the site. Hence, a separation of less than about 20 km between stations is needed to provide a continuous coverage of WV. In case a better resolution is needed or if the lower layers of the atmosphere are under study, then the separation between stations must be reduced accordingly.

Although the end result of tomography is the 3-D distribution of WV density, its application is rather dedicated to case studies than to assimilation into NWP models. Indeed, it is the assimilation of STDs into NWP schemes which will be preferred and can be viewed as equivalent to tomography to retrieve the spatial anisotropy of WV but without the constraints of the necessary station network density and inversion problems.

Nonetheless, GNSS tomography has proven very useful to demonstrate the role of WV as a precursor and a major contributor to CI. For example, *Van Baelen et al.* [2011] have shown that within a frontal system with imbedded convection, the convective activity did develop preferably where there existed "hot spots" of humidity ahead of the frontal line. Likewise, in the case of orographically driven CI, they have identified that the difference between crest against lee side convection could be traced to the wind condition that would allow accumulation of water vapor toward the crest line or in contrary force it down the valleys to trigger

convection at convergence zones [*Van Baelen et al.*, 2011; *Hagen et al.*, 2011]. In very different studies, one over the great plains of central USA and the other in the context of orographic CI in the Vosges, France, *Champollion et al.* [2009] and *Labbouz et al.* [2013], respectively, have clearly identified WV convergence as the initial condition either leading to large-scale convection or triggering localized convective activity. Finally, the work of *Weckwerth et al.* [2014] has also demonstrated the good correspondence of the WV field evolution in agreement with dual Doppler winds as well as the localization of convection triggering over orography. However, it is still an important topic of future research to specify the errors of WV fields derived with GNSS tomography in dependence of spatial and temporal resolutions.

5.2.3. Light Detection and Ranging

Light detection and ranging (lidar) is an active remote sensing technique similar to radio detection and ranging (radar). In contrast to radar, laser pulses are transmitted at wavelengths ranging from 250 nm in UV to 10,000 nm (10 μm), thus several orders of magnitudes shorter than radar wavelengths. Therefore, the lidar signal becomes very sensitive to molecular and aerosol particle scattering and extinction so that measurements can be performed in clear air. For the same reason, lidar measurements are limited up to the edges of clouds and precipitation, if their optical thickness τ is larger than 2. Up to this range, measurements are possible with high temporal and spatial resolution, as the cloud and precipitation properties have negligible influence on the near-range clear air signal.

The two systems on the left in Figure 7 indicate a Raman lidar and DIAL, respectively, and present their signal propagation and detection processes. A temporally very short laser pulse is transmitted in the atmosphere with a duration of $\Delta t \cong 10\text{–}100$ ns, typically. This corresponds to a high raw resolution of the backscatter signals of $\Delta R = c\Delta t/2 \cong 1.5\text{–}15$ m. Along its path, the signal is attenuated due to atmospheric scattering and absorption. The backscattered radiation is proportional to the backscatter coefficient in the range cell. By a time-of-flight measurement, the backscatter signal is detected and recorded in dependence of time and, thus, of range.

The single-scattering lidar equation describes the power of the elastic backscatter signal P_S in dependence of range r and reads [*Wulfmeyer and Walther*, 2001a, 2001b]

$$P_{S,\nu_0}(r) = P_0 \, \xi_{\nu_0} \frac{c\,\Delta t}{2} \frac{A_{\text{tel}}}{r^2} O(r) \left\{ \beta_{\text{par},\nu_0}(r) + \beta_{\text{mol},\nu_0}(r) \right\} \Gamma_{\nu_0}^2(r) + P_{B,\nu_0}$$

$$\text{with} \quad \Gamma_{\nu_0}^2(r) = \exp\left\{ -2\int_0^r \left[\alpha_{\text{par},\nu_0}(r') + \alpha_{\text{mol},\nu_0}(r') + \alpha_{G,\nu_0}(r') \right] dr' \right\}, \tag{16}$$

where ν_0 is the laser frequency or wave number and ξ is the corresponding combined efficiency of the receiver-transmitter optics and the detector system. P_0 is the transmitter peak power, which can be derived from the laser pulse energy E_L and its pulse duration Δt by $E_L = P_0 \Delta t$. A_{tel} is the telescope area, O is the overlap function between laser transmitter beam and field of view of the telescope, and Γ is the transmission of the atmosphere due to the extinction of molecules and particles. The particle and molecular backscattering coefficients as well as the particle and molecular extinction coefficients are β_{par} and β_{mol} as well as α_{par} and α_{mol}, respectively. The absorption coefficient of a trace gas such as WV is $\alpha_{G,\nu}$. The background signal power due to atmospheric radiation and detector dark current is P_B.

Multiple scattering can be neglected because we are focusing on measurements outside of clouds here. Obviously, the backscatter power can be scaled by the average power of the laser transmitter and the size of the receiver. For an optimal SNR, direct detection of the backscatter signal is used leading to a strong dependence of range r. This results in a very high dynamic range of the signals and in a limitation of the near-range coverage by truncating the overlap function. The far range is also affected by the dynamic range due to digitizing errors or Poisson statistics if single photons are detected. In order to optimize the coverage of the signals from the surface to the lower troposphere either a sophisticated design of the receiver, e.g., using two telescopes or two channels with different sensitivities, or scanning are necessary. Further details are discussed in *Goldsmith et al.* [1998] and *Wulfmeyer and Walther* [2001a, 2001b].

In the case of Raman lidar, the lidar equation (16) has to be modified so that the Raman scattering process with respect to molecules is considered. Now, the signal power P_{Ram} at the Raman-shifted frequency reads

$$P_{\text{Ram},\nu_{\text{Ram}}}(r) = P_0 \, \xi_{\nu_0,\nu_{\text{Ram}}} \frac{c\,\Delta t}{2} \frac{A_{\text{tel}}}{r^2} O(r) \beta_{\text{Ram},\nu_0}(r) \Gamma_{\text{Ram},\nu_0,\nu_{\text{Ram}}}^2(r) + P_{B,\nu_{\text{Ram}}}$$

$$\text{with} \quad \Gamma_{\text{Ram},\nu_0,\nu_R}^2(r) = \exp\left\{ -\int_0^r \left[\alpha_{\text{par},\nu_0}(r') + \alpha_{\text{par},\nu_{\text{Ram}}}(r') + \alpha_{\text{mol},\nu_0}(r') + \alpha_{\text{mol},\nu_{\text{Ram}}}(r') \right] dr' \right\}. \tag{17}$$

Here v_{Ram} is frequency or wave number with $v_{Ram} = v_0 + \Delta v_{Ram}$ due to Raman scattering and Δv_{Ram} is the characteristic Raman shift of the molecule of interest. The frequency is chosen so that the absorption of any trace gas can be neglected. The key in Raman lidar methodology is that the Raman backscattering coefficient β_{Ram,v_0} is the product of the number density of the molecule of interest and the differential Raman scattering cross section per solid angle $d\sigma_{Ram}/d\Omega$ in backward direction (indicated by the index π), thus

$$\beta_{Ram,v_0}(r) = N_{mol}(r) \left(\frac{d\sigma_{Ram,v_0}}{d\Omega} \right)_\pi. \tag{18}$$

If a molecule is chosen with well-known volume mixing ratio such as nitrogen or oxygen, the signal can be related to the dependence of the scattering cross section on atmospheric temperature, which leads to the temperature rotational Raman lidar (TRRL) principle. If a molecule is chosen with unknown mixing ratio such as WV but the temperature dependence of the scattering cross section is low and well defined, the signal becomes directly proportional to the WV number density, as in WV Raman lidar (WVRL).

5.2.3.1. Water Vapor Raman Lidar

The Raman lidar technique for the determination of the WV mixing ratio profile $m(R)$ [*Melfi et al.*, 1969] has been extensively discussed in the literature (for a review, see *Whiteman* [2003a, 2003b] and *Wandinger* [2005]). The approach uses either the collection of vibrational Raman backscattered signals applying equations (17) and (18) to WV and nitrogen molecules. Alternatively, for the normalization of the WV channel, a combination of rotational Raman channels can be used [*Hammann et al.*, 2015].

In any case, $m(r)$ can be obtained from the ratio of the WV to the Raman signal used for both the normalization and the elimination of cross sensitivities to unknown quantities, which results in range-resolved derivation

$$m(r) = K_{WV} \frac{P_{Ram,v_{Ram,WV}}(r) - P_{B,v_{Ram,WV}}}{P_{Ram,v_{Ram,N_2}}(r) - P_{B,v_{Ram,N_2}}} \Delta\Gamma_{v_{Ram,WV},v_{Ram,N_2}}(r). \tag{19}$$

In this WVRL equation, K_{WV} is the lidar system calibration coefficient and $\Delta\Gamma_{v_{Ram,WV},v_{Ram,N_2}}(r) = \Gamma_{v_{Ram,N_2}}(r)\Gamma_{Ram,WV}^{-1}(r)$ is the differential transmission term, which accounts for the different atmospheric transmission at the two Raman frequencies $v_{Ram,WV}$ and v_{Ram,N_2} that are characterized by a fixed frequency shift ($\Delta v_{Ram,WV} = 3657\,cm^{-1}$ and $\Delta v_{Ram,N_2} = 2330\,cm^{-1}$ with respect to v_0. Raman lidar systems often make use of frequency-tripled neodymium-doped yttrium aluminum garnet (Nd:YAG) laser sources emitting UV laser pulses around 355 nm. When stimulated at this wavelength, the WV and nitrogen vibrational Raman signals are located near $\lambda_{WV} = 408\,nm$ and $\lambda_{N_2} = 387\,nm$, respectively.

Equation (19) forms also the basis for the estimation of systematic and noise errors in WVRL measurements. With respect to the bias, errors can be introduced by the calibration constant K_{WV} and the differential transmission term $\Delta\Gamma_{v_{Ram,WV},v_{Ram,N_2}}$. Obviously, the relative systematic error in mixing ratio is proportional to the relative errors in K_{WV} and $\Delta\Gamma_{v_{Ram,WV},v_{Ram,N_2}}$. Errors due to the latter are primarily caused by different strengths of Rayleigh scattering and the wavelength dependence of particle extinction. This effect is usually very small (1–2%) and determinable from lidar measurements of particle extinction at 355 nm [*Whiteman*, 2003b].

The daytime performance can be improved using narrowband interference filters for the selection of the WV and N_2 Raman signals. These are band-pass filters with high transmission for the received backscatter signals and high suppression of the radiation in other spectral regions otherwise. The use of narrowband interference filters imposes a proper accounting for the temperature dependence of WV and N_2 Raman scattering. A height-dependent correction term determined from simultaneous temperature lidar measurements or collocated independent temperature measurements from different sensors can be applied to remove this systematic effect, and the residual error after correction is expected to be not exceeding 0.5% [*Whiteman*, 2003a].

The calibration coefficient K_{WV} can be height dependent in the near range due to different overlap functions for the WV and N_2 Raman channels [*Whiteman et al.*, 1992]. The calibration can be performed based on the comparison between simultaneous and collocated WV mixing ratio profiles from the Raman lidar and radiosondes for an extended measurement sample. Further approaches to calibrate the water vapor Raman lidar measurements consider the comparison with other WV sensors, such as the MWR [*Turner and Goldsmith*, 1999; *Turner et al.*, 2002] or GNSS IWV [*Whiteman et al.*, 2006a].
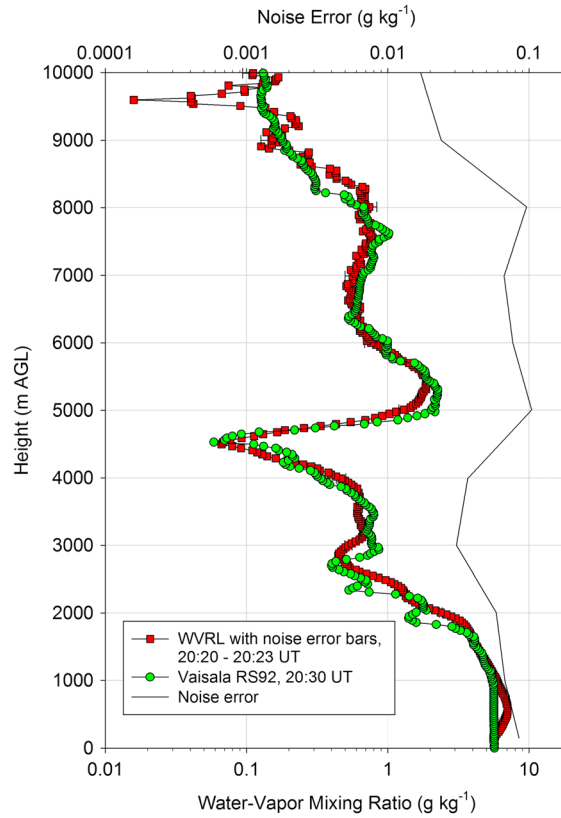
Figure 15. Comparison between mixing ratio measurements of the WVRL BASIL and a Vaisala RS92 radiosonde performed on 19 September 2012 at 20:20 UTC. The resolutions of the Raman lidar profile are 3 min and 150 m, respectively. Here BASIL was using 10 W power (0.5 J, 20 Hz) of the laser transmitter at 355 nm and a telescope diameter of 0.45 m.

Considering all these effects, theoretical analyses [*Whiteman*, 2003a, 2003b; *Whiteman et al.*, 2011] and extensive intercomparisons with in situ sensors and active remote sensing systems [*Soden et al.*, 2004; *Ferrare et al.*, 2004, 2006; *Whiteman et al.*, 2006a, 2006b; *Behrendt et al.*, 2007a, 2007b; *Leblanc and McDermid*, 2008; *Bhawar et al.*, 2011] demonstrated that a systematic error of < 5% can be achieved throughout the troposphere using IWV from GNSS or MWRs as calibration sources [*Turner et al.*, 2002]. This is substantiated by Figure 15, which shows a comparison between the BASIL WVRL and a Vaisala RS-92 radiosonde [*Di Girolamo et al.*, 2009a]. At the time of these measurements, BASIL was deployed in Candillargues (43°36′ 40.10″N, 4°4′15.80″E), Southern France, in the frame of the Special Observation Period 1 (September–November 2012) of Hydrological Cycle in the Mediterranean Experiment (HyMeX). The WVRL captures the detailed vertical structure of humidity from the lower to the middle troposphere including several layers and mixing ratio gradients.

Noise error propagation of the WVRL equation (19) provides estimations of the precision of each single profile. In case of data acquired in photon counting mode, the statistical uncertainty can be estimated through the application of Poisson statistics [e.g., *Whiteman*, 2003b].

*Wulfmeyer et al.* [2010] demonstrated that noise errors derived by Poisson statistics agree very well with noise error analyses using the autocovariance function of the mixing ratio time series. This results in the following, very useful dependence of the relative noise error to system parameters and mixing ratio

$$\frac{\sigma_m}{m} \approx \propto \frac{1}{\sqrt{m}} \frac{1}{\sqrt{A_{tel}\, E_L\, v_R\, \delta t\, \Delta R}} = \frac{1}{\sqrt{m}} \frac{1}{\sqrt{A_{tel}\, P_L\, \delta t\, \Delta R}} ,$$ (20)

where σ_m is the noise standard deviation of the signal after averaging over a certain number of range bins in the vertical and over a number of shots in time, v_R is the repetition rate of the laser transmitter, P_L is the laser average power, and δt is the averaging time. Obviously, under many atmospheric conditions, temporal and spatial resolution can be traded off with respect to the desired precision.

The vertical resolution ΔR of the derivation of WV profiles is usually not the raw resolution of the lidar signal measurement. Some vertical averaging of the signals by applying filter functions or box averaging is necessary to reduce the noise error to acceptable levels. The vertical resolution is clearly defined by the number of range bins used for vertical averaging as these can be considered as statistically independent.

Statistical errors for mixing ratio measurements for both nighttime and daytime operation are represented in Figure 16. Simulations have been performed based on mixing ratio, temperature, and pressure profiles from the same radiosonde observation in Figure 9 in combination with the ESA median particle backscatter profile [*Vaughan et al.*, 1998]. These results are based on an average power of 10 W (single-pulse energy of 500 mJ with a repetition rate of 20 Hz) at 355 nm and a receiver diameter of 0.8 m (FOV = 200 μrad). Vertical and temporal resolutions are 300 m and 10 min, respectively, and can be traded off to improve measurement precision in the near range according to equation (20). Generally, for nighttime operation,
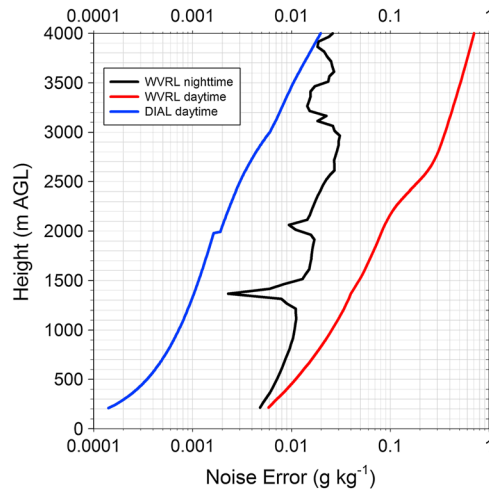
Figure 16. Noise error simulations of WVRL and WVDIAL using the same WV profile as in Figure 9 and resolutions of 10 min and 300 m, respectively. The average power and telescope diameter of the WVDIAL were set to 2 W and 0.4 m, respectively, whereas 10 W and 0.8 m were used for the WVRL.

the noise error is < 1% up to 3 km and < 10% up to 7 km. For daytime operation, the noise error amounts to < 10% up to 3 km and < 100% up to 4.5 km.

As a further example, Figure 17 presents the time evolution of the mixing ratio as measured by BASIL during the same deployment considered in Figure 15 over a time period of approximately 22 h from 16:42 UT on 25 September 2012 to 14:43 UT on 26 September 2012 during the passage of a squall line, which produced a cumulated precipitation of more than 100 mm in 24 h in the Cévennes area. Lidar measurements illustrated in this figure are based on a temporal and vertical resolution of 3 min and 150 m, respectively, and demonstrate the capability of WVRL for resolving the vertical structure and evolution of the WV field with high accuracy and resolution.

These results achieved with stationary, operational WVRL systems confirm the maturity of this technique for long-term, highly accurate WV profiling (D. D. Turner et al., submitted manuscript, 2014). However, the deployment and operation of these systems still requires significant maintenance efforts. Furthermore, measurements with high precision during daytime require large laser sources and telescopes. In the future, it is necessary to make these systems more compact, robust, and commercially available. If this is successful, WVRL has a great potential to be deployed in networks.

5.2.3.2. Temperature Rotational Raman Lidar

Temperature-dependent signals can be obtained with lidar via a number of spectroscopic principles. Consequently, many techniques for atmospheric T measurements have been proposed and tested in recent years (see *Behrendt* [2005] for an overview); however, only a few showed sufficient experimental success. As the temperature information is carried by molecular backscatter signals—not the backscatter signals of particles—the techniques can be classified by how well they can cope with the disturbing presence of particles in the heights where temperature measurements are desired. Obviously, elastic backscatter signals can only be used as long as the atmospheric particle content is negligible and the signal is only by molecules, e.g., in the aerosol- and cloud-free stratosphere. In this case, the integration technique provides T profiles based on elastic backscatter signals. As the molecular backscatter signal is proportional to the molecular number density, the lidar signal can be related to the temperature in a certain height if the pressure is known.
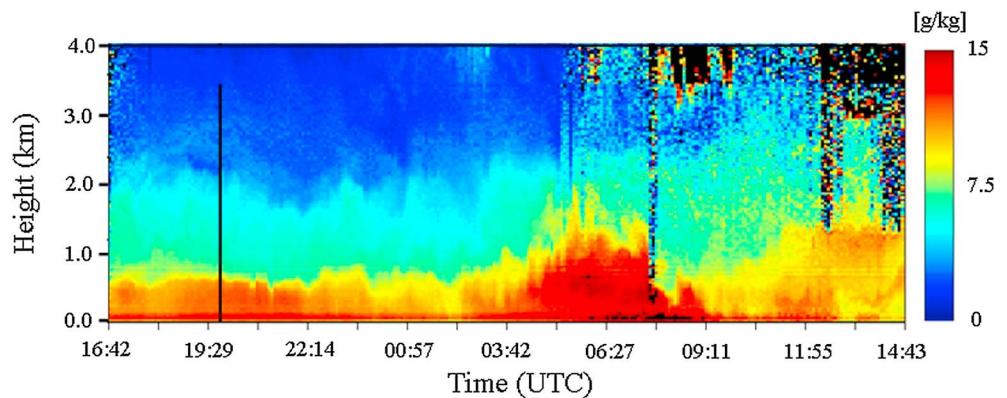
Figure 17. Time evolution of the mixing ratio as measured by BASIL over the time period from 16:42 UT on 25 September 2012 to 14:43 UT on 26 September 2012 during the passage of a squall line. The resolutions are 150 m in the vertical and 3 min in time, respectively. The black areas are due to the presence of clouds.

Assuming that the atmosphere is in hydrostatic equilibrium and initializing the algorithm in an upper starting height, the lidar profile can be used to derive stepwise the temperature also in lower altitudes [*Hauchecorne et al.*, 1992]. Initialization errors become exponentially smaller for data in lower altitudes and thus negligible from distances of about 10 km from the initialization altitude. A calibration is not required. Extension of the integration technique into the lower stratosphere with its higher aerosol content is possible by the Raman integration technique [*Fiocco et al.*, 1971], which uses inelastic vibrational nitrogen Raman signals instead of elastic signals.

In the troposphere, however, the particle content even in cloud-free situations is generally too large to apply the Raman integration technique. Furthermore, the integration Raman technique fails also in the stratosphere when polar stratospheric clouds or volcanic ash yield significant extinction. While the presence of atoms from elements like Na, K, Ca, and Fe allow for using resonance fluorescence effects for temperature measurements in the mesopause region (see *Abo* [2005] for an overview), this concept is not applicable in the troposphere either.

For lidar measurements in the troposphere, three techniques remain: DIAL, HSRL, and TRRL. Measurements with DIAL are based on the temperature dependency of molecular absorption, e.g., of oxygen with its constant mixing ratio in the dry atmosphere. Theoretical considerations and results of experimental studies, however, have shown that aerosol gradients cause strong systematic errors of several K [*Theopold and Bösenberg*, 1993], which are too large for most applications.

HSRL employs the temperature dependence of the shape of the Cabannes line for temperature measurements (here we follow the convention that Rayleigh scattering comprises both Cabannes scattering and rotational Raman scattering) [*Hair et al.*, 2001]. The comparatively high signal intensities of this technique are very attractive. However, difficulties in suppressing the elastic backscatter signals in the temperature-dependent molecular channels with sufficient performance are currently prohibiting applications of this technique beyond a clear atmosphere.
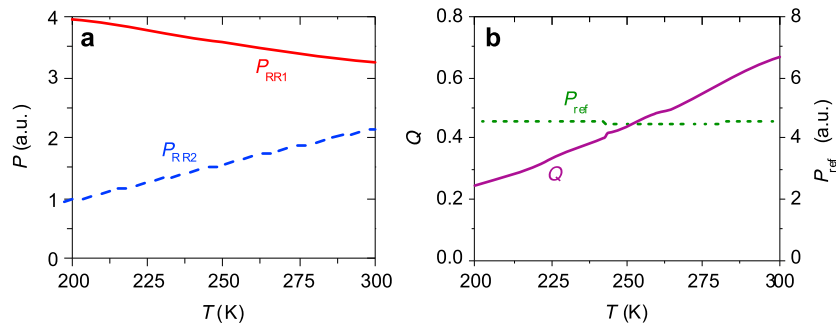
Rotational Raman lidar is presently the most accurate and precise lidar technique for tropospheric T profiling. This technique [*Cooney*, 1972] is based on the fact that the population of the rotational states of atmospheric molecules such as N_2 and O_2 depends on atmospheric temperature. Consequently, the intensity of different lines within the rotational Raman spectrum show different temperature dependences. While lines closer to the frequency of the exciting radiation become weaker with increasing temperature, lines farther away show the opposite effect and increase in intensity with increasing temperature. As the temperature dependency of the line intensities is already strong for the temperature range present in the Earth's atmosphere, it can be employed by TRRL.

For atmospheric temperature profiling with the rotational Raman technique, the ratio

$$Q(T,r) = \frac{P_{\mathrm{RR2}}(T,r) - P_{\mathrm{B,RR2}}}{P_{\mathrm{RR1}}(T,r) - P_{\mathrm{B,RR1}}} \tag{21}$$

is used. P_{RR1} and P_{RR2} stand for two pure-rotational Raman signals of opposite temperature dependence corrected for the background signals $P_{\mathrm{B,RR1}}$ and $P_{\mathrm{B,RR2}}$, respectively. For determining these signals, equations (17) and (18) are applied but now the rotational Raman scattering of gases with well-known partial pressure is used such as molecular oxygen and nitrogen. By taking this ratio Q, altitude-dependent factors of the lidar equation, unknown system parameters, and other atmospheric variables largely cancel. This requires the same overlap function for both channels, which is the case for well-aligned systems above a certain minimum height. Also, the atmospheric extinction of both signals is eliminated, as no molecular absorption lines are present within their range. The temperature dependence of the ratio Q is given by

$$Q(T,r) = K_T \frac{\sum\limits_{n=\mathrm{O_2,N_2}} \sum\limits_{i} \Gamma_{\nu_{\mathrm{RR,}i,n}}(r) \left(\dfrac{\mathrm{d}\sigma_{\mathrm{RR,}J_i,n}}{\mathrm{d}\Omega}\right)_{\pi} [T(r)]}{\sum\limits_{n=\mathrm{O_2,N_2}} \sum\limits_{k} \Gamma_{\nu_{\mathrm{RR,}k,n}}(r) \left(\dfrac{\mathrm{d}\sigma_{\mathrm{RR,}J_k,n}}{\mathrm{d}\Omega}\right)_{\pi} [T(r)]}. \tag{22}$$

Figure 18. (a) Typical intensities of the two pure-rotational Raman signals P_{RR1} and P_{RR2} as a function of temperature T [from *Behrendt et al.*, 2004]. (b) Signal ratio Q from which the atmospheric temperature is derived. P_{ref} is a temperature-independent Raman reference signal for measuring extinction and backscatter coefficients of aerosols and cloud particles [*Behrendt et al.*, 2002].

Here formulas for the Stokes or anti-Stokes differential Raman backscatter coefficients have to be inserted depending on which branch of the pure RR spectrum is used. These equations are very well known from molecular spectroscopy and are found in *Behrendt* [2005]. $\Gamma_{RR1,i,n}$ and $\Gamma_{RR2,i,n}$ are the transmissions of the lidar receiver at the frequencies $\nu_{RR,i,n}$ related to the rotational Raman line numbers J_i and the molecule type n, which are transmitted by the interference filters for the RR2 and RR1 channels. Similar to the WVRL, a system calibration coefficient is remaining which is called K_T. Figure 18 presents typical dependencies of the RR signals used for T profiling.

Different approaches of the inversion of equation (22) with respect to T have been proposed [*Behrendt*, 2005]. In theory, the calibration can be performed by characterizing the system parameters. This approach, however, can yield uncertainties of the order of a few K [*Vaughan et al.*, 1993]. The relationship, which turned out to be most accurate, reads

$$T(r) = \frac{1}{a \pm \sqrt{a^2 - 4b\left[f - \ln Q(T, r)\right]}}, \tag{23}$$
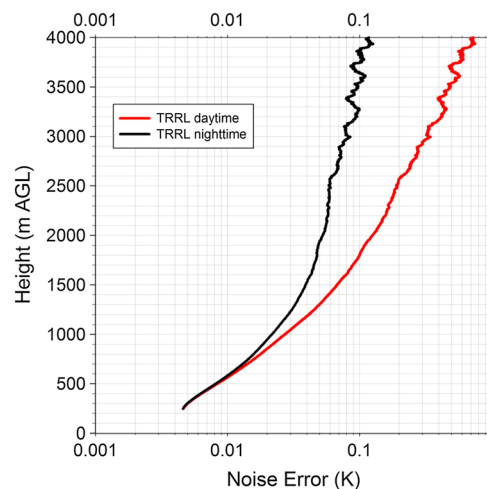
which requires the calibration of the T profile with respect to $Q(T,r)$ using three fit coefficients a, b, and f. In practice, TRRL data are calibrated by comparisons with other instruments such as local radiosondes similar to WVRL. For accurate measurements, crosstalk of the elastic signal into the Raman channels must be avoided, even in the presence of clouds. A blocking of at least 7 orders of magnitude is required for the elastic backscatter signal in the rotational Raman channels. This high blocking value at spectral distances of a few tens of wave numbers, however, can be realized with multicavity interference filters. Thus, accurate temperature measurements are even possible in aerosol layers and optically thin clouds [*Behrendt and Reichardt*, 2000]. Typically, the systematic errors of TRRL profiles are < 0.5 K throughout the troposphere where full overlap between the transmitter and the receiver is achieved.

Similar to the WVRL, the statistical uncertainty of the RRL temperature measurements can be determined from the number of photon counts using Poisson statistics. The noise error σ_T includes the contribution of the background signals in the two rotational Raman channels. Similar as for WVRL, the comparison of the noise errors calculated from the signal intensities with noise errors determined by autocovariance analyses of temperature fluctuations in the convective ABL shows close agreement [*Behrendt et al.*, 2015]. Furthermore, the dependence of the SNR on system parameters is basically the same as for WVRL (see equation (20)), which is very useful for the system design. Thus, the same considerations apply for the definition of the vertical resolution, which is given by the number of range bins used for vertical averaging. To illustrate the measurement performance, we use in the following the most recent data of the UHOH TRRL system [*Radlach et al.*, 2008; *Hammann et al.*, 2015]. This lidar consists of a frequency-tripled
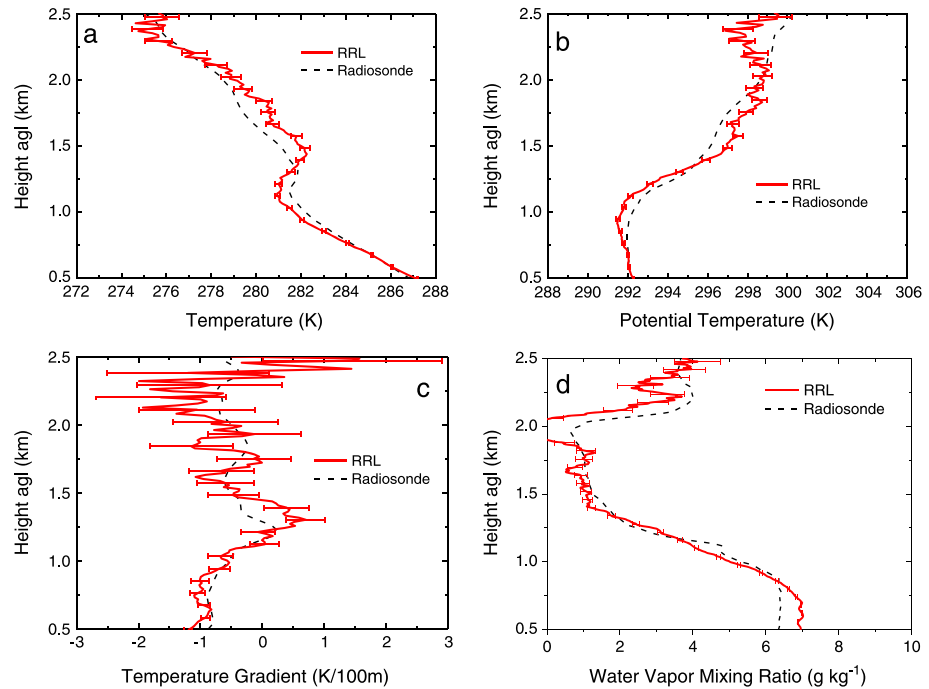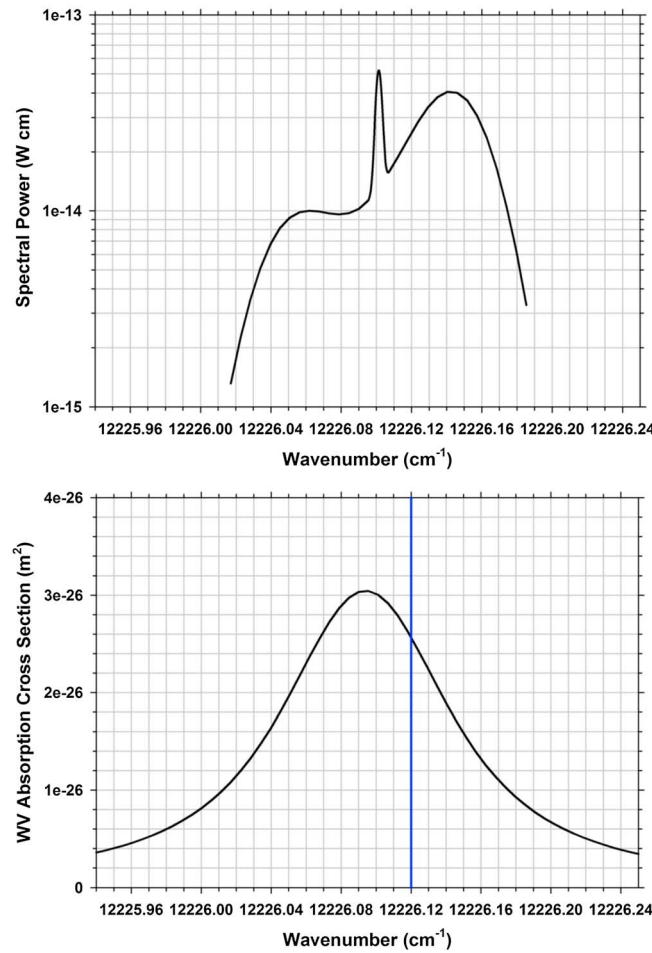
Figure 19. Measurements of the UHOH TRRL between 1300 and 1330 UTC on 19 May 2013 with data of a local radiosonde launched at 1300 UTC (dashed) for comparison. The vertical resolutions were 105 m for *T* and 154 m for WV, respectively. (a) *T*, (b) potential temperature, (c) temperature gradient, and (d) WV mixing ratio. Error bars show the noise errors of the lidar data. Altitudes below 500 m are affected by nontotal overlap yet and are therefore not shown [from *Hammann et al.*, 2015].

Nd:YAG laser at 355 nm with 10 W average power at 50 Hz, a two-mirror scanner, a 40 cm receiving telescope, and a highly efficient polychromator with cascading interference filters for separating four signals: the elastic backscatter signal, two rotational Raman signals with different temperature dependence, and the vibrational Raman signal of WV. The main measurement variable of the UHOH TRRL is temperature, and the system was optimized for this purpose. Thus, this system is truly a high-resolution, daytime TD profiler for WV, *T*, and relative humidity measurements.

Figure 19 shows an example of *T* and WV profiling with the UHOH RRL. The noise error of a 20 min temperature measurement of this instrument is lower than 0.1 K up to 1050 m agl at noontime; even for single 10 s temperature profiles, it is still smaller than 1 K up to 1000 m above ground [*Behrendt et al.*, 2015]. At other times of the day, the errors are lower, as noontime is the least favorable time of the day for TRRL measurements because the background light increases the statistical errors. Based on these results, it is possible to estimate the noise errors of a *T* measurement using the profile shown in Figure 9 (analog to Figure 16 for WVRL and WVDIAL). The results are illustrated in Figure 20. Using resolutions of 300 m and 10 min, during daytime the noise error is < 1 K and during nighttime even < 0.1 K up to 4 km. In the near range, combinations of considerable higher temporal-vertical resolutions are possible trading off the overall noise error.

Figure 20. Noise error simulations of TRRL using the same *T* profile as in Figure 9 and resolutions of 10 min and 300 m, respectively. The average power and telescope diameter of the TRRL were set to 10 W and 0.8 m.

Figure 21. (top) Simulation of an online backscatter signal spectrum from a range of 3 km. Clearly, the Mie backscatter peak on the molecular broadened signal is resolved. The return signal is asymmetric, as the online frequency of the laser transmitter was not centered on the absorption line. (bottom) WV absorption cross section in dependence of wave number at 3 km (black) and the location of the online wave number at 12226.12 cm^{-1} (blue).

In recent years, TRRLs reached the maturity to demonstrate routine T profiling by day and night. However, a couple of obstacles have still to be overcome, which are similar to that of WVRL: Corresponding systems are not commercially available yet and require strong laser sources and large receivers. Furthermore, long-term operation and stability of the calibration of TRRL still have to be confirmed. In combination with WVRL in one instrument, this makes Raman lidar a very interesting candidate to be operated in networks for combined WV, T, and RH profiling.

5.2.3.3. Water Vapor Differential Absorption Lidar

Differential absorption lidar (DIAL) measures the ratio between two elastic backscatter signals, the online signal, which is tuned to the center of a WV absorption line, and the offline signal, which is tuned to a nonabsorbed spectral region [*Schotland*, 1966]. Therefore, the DIAL signals have a larger SNR than the Raman signals. Taking the ratio of these signals and its logarithmic derivative, Beer's law can be applied and the resulting quantity is nearly proportional to differential optical thickness $\Delta\tau_W$ of WV in the range cell. Accordingly, with DIAL the range-resolved *WV number density* N_{WV} or the *absolute humidity* ρ_{WV} are determined. The relative statistical error is not only dependent on the noise characteristics of the backscatter signals but also inversely proportional

to the differential optical thickness in the range cell. Further details are discussed in *Wulfmeyer and Walther* [2001a, 2001b]. For the derivation of WV profiles, the spectral properties of the laser transmitter, the backscattered spectrum, and the absorption lines must be considered. In this case, the lidar equation reads

$$
\begin{aligned}
P_{S,v_0}(r) = {} & P_0\,\xi_{v_0}\frac{c\,\Delta t}{2}\frac{A_{\text{tel}}}{r^2}O(r)\,\Gamma^2_{\text{air},v_0}(r) \\
& \cdot\left\{ \begin{array}{l} \beta_{\text{par},v_0}(r)\displaystyle\int_{-\infty}^{\infty}S_L(v-v_0)\,\Gamma^2_{\text{WV}}(v,r)\,F_R(v)\,\mathrm{d}v\;+ \\[1em] \beta_{\text{mol},v_0}(r)\displaystyle\int_{-\infty}^{\infty}[[S_L(v-v_0)\,\Gamma_{\text{WV}}(v,r)]\times\text{DB}(v,r)]\,\Gamma_{\text{WV}}(v,r)\,F_R(v)\,\mathrm{d}v \end{array}\right\} + P_{B,v_0},
\end{aligned}
\tag{24}
$$

where S_L is the normalized laser transmitter spectrum at ground, F_R is the spectral transmission function of the receiver interference filter, and DB is the spectral broadening of the backscattered signal due to Rayleigh scattering. This equation demonstrates that spectral effects in the propagation of the laser radiation must be considered for an accurate determination of the signal. Just the weak frequency dependence of backscatter coefficients over the small spectral width of the transmission of F_R can be

neglected. As an example, Figure 21 presents the spectrally resolved backscatter signal of a lidar system operating on a WV absorption line in the 820 nm wavelength region and the corresponding WV absorption cross section. As the laser transmitter frequency is not centered on the absorption line, the spectrum is asymmetric. It consists of the Mie peak due to particle scattering and the spectrally broader Rayleigh scattering due to molecules. Please note that Rayleigh broadening always occurs even if the laser transmitter function is a delta distribution. The WV information is contained in its transmission, which is dependent on the WV number density and laser frequency. Obviously, a sophisticated knowledge in high-resolution spectral radiative transfer is necessary for the understanding and simulation of DIAL as in passive remote sensing.

By taking the ratio of the online and offline backscatter signals, the sensitivity with respect to system constants and molecular and particle backscatter and extinction is nearly eliminated. The next steps in the derivation of N_{WV} are dependent on the design of the laser transmitter. There are two approaches:

1. *Narrowband DIAL* with ultra narrowband operation of the laser transmitter. This is the approach currently used in all DIAL groups. In this case, equation (24) can be simplified by replacing the laser spectrum S_L by a delta distribution. If a very high frequency stability and spectral purity of the transmitter is realized, the resulting derivation is simple and nearly independent of the transmitter and receiver filter properties. Except at strong backscatter ratio gradients where a correction due to Rayleigh-Doppler broadening may be applied, this leads to a very high accuracy of the DIAL technique.
2. *Broadband DIAL* with a laser transmitter spectrum, which overlaps several water vapor absorption lines. In this case, it is not possible to simplify the DIAL equation with respect to the laser spectrum. However, a unique solution can still be derived. Furthermore, though this technique has not been applied yet, a reduction of systematic errors due to Rayleigh-Doppler broadening can be expected. Due to the lack of existing systems, we focus on narrowband DIAL in the following.

In case of narrowband WVDIAL, the laser spectrum S_L is considered as a delta distribution. Furthermore, over the narrow spectral range of the signals, the spectral transmission of the receiver can be considered as constant. In order to achieve this performance for the WVDIAL laser transmitter, extensive efforts are necessary with respect to laser frequency and bandwidth control [*Wulfmeyer et al.*, 1995; *Wulfmeyer and Bösenberg*, 1996].

Typically, the online frequency is located close to the center of the WV absorption line of interest and the offline laser frequency is located in an absorption minimum. Using equations (3) and (6) in combination with equation (24) and taking the derivative of the online and offline signal ratio leads to the following iterative solution with a unique result and no remaining calibration coefficient

$$N_{WV}(r) = \frac{1}{2\left[\sigma_{WV,\nu_{on}}(p,T) - \sigma_{WV,\nu_{off}}(p,T)\right]} \frac{d}{dr} \ln\left[\frac{P_{S,\nu_{off}}(r) - P_{B,\nu_{off}}}{P_{S,\nu_{on}}(r) - P_{B,\nu_{on}}}\right]$$

$$+ \frac{1}{2\left[\sigma_{WV,\nu_{on}}(p,T) - \sigma_{WV,\nu_{off}}(p,T)\right]} \frac{d}{dr} \ln\left[\frac{\beta_{par}(r) + \beta_{mol}(r)\,\Gamma_{WV,\nu_{on}}^{-1}(r) \int_{-\infty}^{\infty} \Gamma_{WV}(\nu,r)\,DB(\nu - \nu_{on},r)\,d\nu}{\beta_{par}(r) + \beta_{mol}(r)}\right]. \quad (25)$$

In equation (25), we omitted the frequency indices for the backscatter coefficients, as these can be considered as the same for the online and the offline frequencies. Obviously, at gradients of the backscatter ratio $\beta_{mol}/(\beta_{mol} + \beta_{par})$, a correction with the second term on the right-hand side of this equation becomes necessary. Whereas the molecular backscatter and extinction can easily be determined using standard atmospheric profiles, the particle backscatter profile must be determined by analytical inversion of the offline signal [e.g., *Di Girolamo et al.*, 2008]. *Späth et al.* [2015] demonstrate that the correction is strongly reduced, if the laser is not operated at the center of the WV absorption line but tuned to its wing.

In case of weak gradients of the backscatter ratio, this derivation can further be simplified to the well-known WVDIAL approximation

$$N_{WV}(r) = \frac{1}{2\left[\sigma_{WV,\nu_{on}}(p,T) - \sigma_{WV,\nu_{off}}(p,T)\right]} \frac{d}{dr} \ln\left[\frac{P_{S,\nu_{off}}(r) - P_{B,\nu_{off}}}{P_{S,\nu_{on}}(r) - P_{B,\nu_{on}}}\right]. \quad (26)$$

Systematic and noise errors of WVDIAL were derived by analytical [*Browell et al.*, 1979, 1991; *Ismail and Browell*, 1989; *Bösenberg*, 1998; *Wulfmeyer and Walther*, 2001a, 2001b] and end-to-end performance modeling
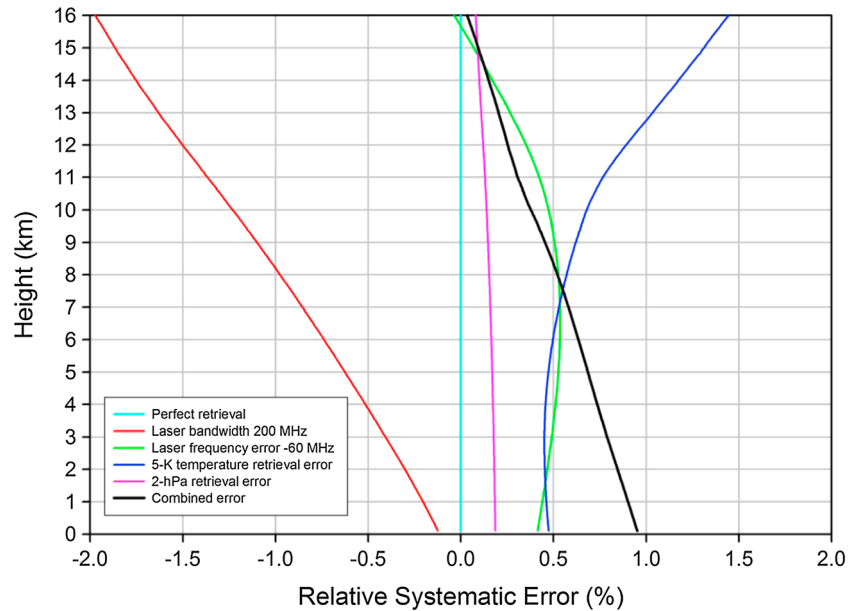
Figure 22. End-to-end simulation of WVDIAL systematic errors and their combination. The resulting overall systematic error is $< 1\%$. Online wave number: 12,226.1012 cm^{-1}, offline wavenumber: 12,227.63 cm^{-1}, U.S. Standard Atmosphere.

[*Di Girolamo et al.*, 2004b, 2004c; *Bauer et al.*, 2004; *Summa et al.*, 2004; *DLR*, 2005; *Di Girolamo et al.*, 2008]. The bias of a WVDIAL measurement can be estimated by systematic error propagation of equation (25), which reads

$$\frac{\Delta N_{WV}}{N_{WV}} \approx \frac{\Delta \sigma_{WV}}{\sigma_{WV}}. \qquad (27)$$

The error in σ_{WV} can be due to a variety of sources such as laser frequency instabilities, laser spectral impurity but also uncertainty of the WV absorption cross section by spectroscopic measurements in the laboratory and by its dependence on p and T [*Bösenberg*, 1998]. Recent advances in high- and low-power laser technology [*Wulfmeyer and Bösenberg*, 1996; *Nehrir et al.*, 2011; *Repasky et al.*, 2013; *Wagner et al.*, 2013a] demonstrated that these challenges with respect to laser performance can be overcome. Current properties of advanced laser transmitters for ground-based WVDIAL are causing systematic errors of $< 1\%$ [*Wagner et al.*, 2011, 2013a; *Metzendorf et al.*, 2015]. Spectroscopic errors are specified in the new HITRAN2012 database and are of the order of 2%. Errors due to the temperature and pressure dependence of σ_{WV} are $< 2\%$ as well [*Rothman et al.*, 2003, 2005; *Späth et al.*, 2014].

Using an end-to-end simulator, the combined system bias can be estimated [*Di Girolamo et al.*, 2004b, 2004c, 2008; *ESA*, 2004]. An example is presented in Figure 22. A vertically pointing WVDIAL was simulated operating in U.S. Standard Atmosphere with an ESA median particle backscatter profile [*Vaughan et al.*, 1998]. Single-error profiles were simulated and combined to an overall error budget. The figure shows that the combination of these errors is not obvious. In this case, the overall error is $< 1\%$ over the entire troposphere. With end-to-end simulators, also the combination of bias and noise errors is possible. By repeating derivations many times, a complete PDF of the inversion can be determined considering the combination of all specification of the transmitter and receivers [*Di Girolamo et al.*, 2004c, 2008]. It is one of the strengths of the WVDIAL technique that these estimations are theoretically possible. The results demonstrate that WVDIAL is an excellent candidate for a reference profiler.

The high accuracy of WVDIAL has been demonstrated by means of comparisons with radiosondes and within extended measurement campaigns [*Ferrare et al.*, 2004; *Bhawar et al.*, 2011]. The current state of the art of ground-based WVDIAL is represented by the UHOH system [*Behrendt et al.*, 2009; *Wagner et al.*, 2011, 2013a]. During a recent extensive verification campaign in fall 2013, about 30 comparisons with the Vaisala RS92 radiosonde were performed. Figure 23 presents an example of the comparisons performed on 3 October 2013 at 13:07 UTC using equation (26) without any correction for Rayleigh-Doppler broadening. The noise error bars for the DIAL profile correspond to resolutions of 20 min and 150 m, respectively. These can be determined online in dependence of all weather conditions using the autocovariance technique introduced in *Lenschow et al.* [2000]
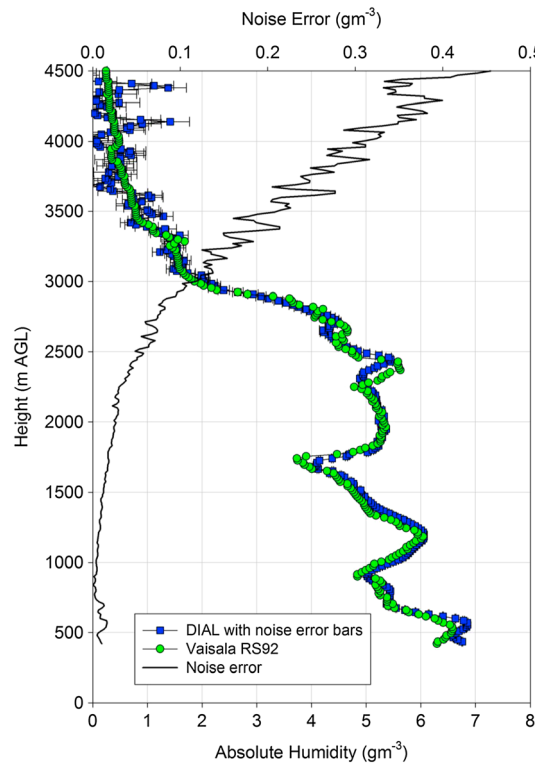
Figure 23. Comparison between UHOH WVDIAL and Vaisala RS92 radiosonde measurements performed on 3 October 2014 at 13:07 UTC. The resolutions of the DIAL profile are 20 min and 150 m, respectively. The noise errors of the DIAL profile are also shown.

and *Wulfmeyer et al.* [2010]. Excellent agreement is achieved, and the complex vertical structure of the lower troposphere is very well resolved. Further examples with similar performance are presented in *Späth et al.* [2014]. Generally, comparisons and theoretical analysis confirm a bias of $< 5\%$ of WVDIAL profiles throughout the troposphere.

For noise error analyses, sophisticated end-to-end performance models are not necessary but analytical models are sufficient. A corresponding model has been developed by *Wulfmeyer and Walther* [2001a, 2001b] and applied for scaling of ground-based, airborne, and spaceborne WVDIAL systems. These included ground-based vertical pointing and scanning operation, airborne operation downward and upward pointing operation at different height levels, and horizontal pointing from aircraft. They also demonstrated that their analyses are in very good agreement with real measurements of DIAL systems. As for WVRL and TRRL, the system noise can be derived by noise error propagation [*Wulfmeyer and Walther*, 2001a, 2001b]. However, the absorption measurement introduces an additional dependence of the system noise on range resolution. This results in a stronger noise averaging behavior with respect to the range resolution in comparison to Raman lidar because the relative error is also dependent on the differential optical thickness in the range cell $\Delta \tau_{WV}$. It follows

$$\frac{\sigma_{N_{WV}}}{N_{WV}} \propto \frac{1}{\Delta \tau_{WV}} \frac{1}{\sqrt{A_{tel} P_L \, \delta t \, \Delta R}} \propto \frac{1}{\sqrt{A_{tel} P_L \, \delta t \, \Delta R^3}} . \tag{28}$$

The comparison of equations (20) and (28) demonstrates that the relative error of WVRL degrades with smaller mixing ratio whereas in WVDIAL, the relative error can be kept nearly constant in all climate zones by adapting the differential optical thickness using WV absorption lines with different line strengths. Based on previous measurements and the simulations with analytical models, the expected noise error profile using the WV profile of Figure 9 can be estimated. The result is presented in Figure 16 together with the corresponding WVRL profiles. As expected, due to the higher SNR of the WVDIAL backscatter signals, a very low noise error is achieved, which is less than WVRL for both daytime and nighttime up to 4 km. Furthermore, the daytime and nighttime performance of WVDIAL is nearly the same so that only the daytime error profile is presented. Again, in the near range, considerably higher vertical-temporal resolution can be achieved using the trade-off of noise errors based on equation (28).

The high resolution and accuracy of WV profiling using the DIAL technique is demonstrated in Figure 24. Using resolutions of 10 s and 150 m for a single profile, a range-height-indicator (RHI) scan is presented with a scan speed of 0.1° s^{-1}. Thus, the angular resolution of each profile is 1°, and the 120° scan is completed in 20 min. Now, it is possible to study the horizontal structure of the ABL and clouds as well as the humidity around clouds up to a range of several kilometers.

These results indicate that monitoring of WV is possible with a compact system design using a low power of the WVDIAL transmitter and a small telescope. An example of the expected performance is presented in Figure 25. An average power of 0.1 W, a telescope diameter of 0.3 m, and filter bandwidth of 0.5 nm were considered using the same atmospheric conditions and system parameters as in *Wulfmeyer and Walther* [2001b]. Using an averaging time of 10 min and a vertical resolution of 300 m, accurate WV profiling with low noise in
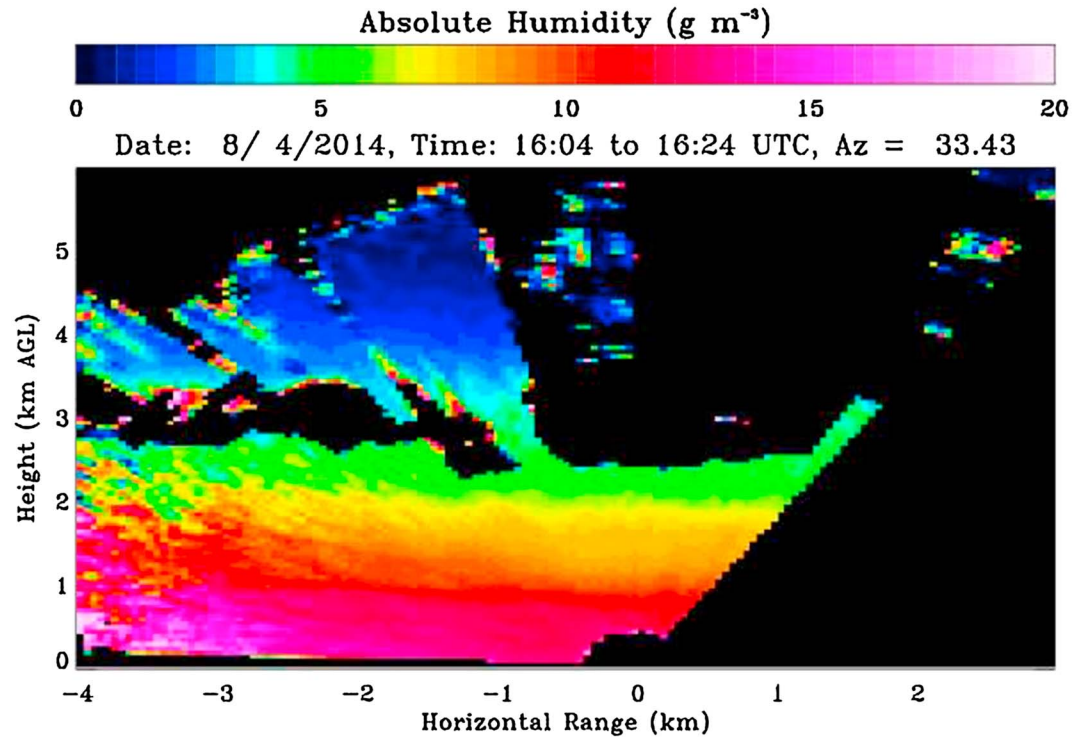
Figure 24. RHI scan of WV performed with the UHOH WVDIAL on 4 August 2014. The scan speed is $0.1°\,s^{-1}$, and the resolutions of the derived WV field are 10 s and 300 m, respectively. Over a range of several kilometers, the horizontal structure of the ABL and clouds (marked by black areas) can be investigated. Also, the humidity around clouds can be studied.
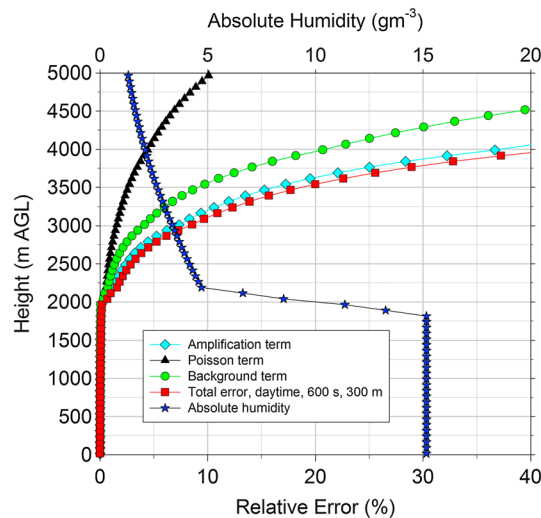
Figure 25. Expected performance of a ground-based, vertically steering DIAL in the ABL up to 5 km. The absolute humidity profile is also shown. The noise error profiles are determined for a DIAL operating at 820 nm with a low average power of 0.1 W and a receiver diameter of 0.3 m. The overall noise error (total error) is mainly caused by amplifier and detector noise (amplification term), daylight background (background term) but not by backscatter signal Poisson statistics (Poisson term). Even using this low average power of the transmitter, the noise error is negligible throughout the ABL.

the lower troposphere is possible. Figure 25 includes different error contributions; however, the dominant error sources are daylight background and detector-amplifier noise. The black curve shows the theoretical noise limit, if the errors are produced only due to Poisson statistics of the transmitter photon number.

This kind of low-power DIAL is capable of providing WV profiling with acceptable precision throughout the ABL fulfilling most of the requirements summarized in Table 1. The fine structure of the error profiles depends on the WV profile so that even a large range can be achieved, if the ABL depth is increasing. After initial work at NOAA [*Machol et al.*, 2004] and *Nehrir et al.* [2009, 2011], a suitable demonstrator has been developed and specified by *Repasky et al.* [2013] and *Spuler et al.* [2015].

Obviously, WVDIAL is a promising candidate for a low-power, compact WV remote sensing system to be deployed in networks. Both bias and precision can be well specified by theoretical analysis and have been confirmed experimentally by comparisons. The derivation of WV profiles is straightforward, simple, and fast; e.g., these could be even applied for DA in nowcasting NWP models.

Table 2. Overview of the Current Performance of Passive and Active Remote Sensing Systems With Respect to WV Profiling[a]

PERFORMANCE		PASSIVE REMOTE SENSING		ACTIVE REMOTE SENSING		
GROUND-BASED						
		IR	**MW**	**GNSS**	**WVRL**	**WVDIAL**
Average power, W		Not scalable		5	10	2
Receiver diameter , m				0.2	0.8	0.4
Vertical range , km	Daytime	4	4	Integral between receivers	6	8
	Nighttime				14	10
Vert. res. , m	Daytime	50-2000	100-3000	Integral between receivers	75-500	15-900
	Nighttime				30-500	
Time res. , s	Daytime	60	300	1	10-600	1-10 in LT
	Nighttime				10-600	10-60 in MT 60-900 in UT
Precision , %		10-20	10-20	1 mm in PW, tbd for tomography	1-10	1-10
Bias , %		< 10	< 10	< 1 mm in PW, tbd for tomography	< 5	2-5
SPACEBORNE						
		NEAR-IR	**IR**	**MW**	**GPS RO**[b]	**WVRL**	**WVDIAL**[c]
Average power , W		Not scalable			5	-	10
Receiver diameter , m					0.5	-	1.5
Range from space , km		Vertical integral	LT to LS		LT to UT	-	Ground to LS
Vertical resolution, m	Daytime	Vertical integral	2000	2000-4000	100	-	300
	Nighttime	n.a.					
Horizontal resolution / footprint , km	Daytime	1-2	20	50	100-200	-	100
	Nighttime	n.a.					
Precision , %		10-20	10-20	10-20	10-20	-	10-20
Bias , %		< 20	< 20	< 20	5-10	-	< 5

[a]LT: lower troposphere, MT: middle troposphere, UT: upper troposphere, LS: lower stratosphere, tbd: still to be determined, NA: not available.
[b]Derived from refractivity using auxiliary data such as from model analyses [e.g., *Vergados et al.*, 2014].
[c]Simulated [*ESA*, 2004; *Wulfmeyer et al.*, 2005; *Di Girolamo et al.*, 2006].

Table 3. Overview of the Current Performance of Passive and Active Remote Sensing Systems With Respect to *T* Profiling

PERFORMANCE		PASSIVE REMOTE SENSING		ACTIVE REMOTE SENSING	
				GROUND-BASED	
		IR	**MW**	**GNSS**[a]	**TRRL**
Average power, W		Not scalable		5	10
Receiver diameter , m				0.2	0.8
Vertical range , km	Daytime	4	4	-	4
	Nighttime				20
Vert. res. , m	Daytime	30-2000	100-3000	-	60-300
	Nighttime				30-150
Time res. , s	Daytime	60	300	-	10-600
	Nighttime				10-300
Precision , K		0.2 – 1	0.5 – 1.5	-	1
Bias , K		< 0.5	< 0.5	-	< 0.5
				SPACEBORNE	
		IR	**MR**	**GNSS RO**[b]	**TRRL**[c]
Average power, W		Not scalable		5	10
Receiver diameter , m				0.5	1.5
Range from space , km		LT to LS		UT to LS	Entire troposphere
Vertical reso-lution, m	Daytime	1000- 2000	2000	100	300
	Nighttime				
Horizontal resolution / footprint , km	Daytime	20	50	100-200	100
	Nighttime				
Precision , K		1	1	0.5	1
Bias , K		< 1	< 1	< 0.2	< 1

[a]The product of ground-based GNSS networks is IWV.
[b]The product of RO in the LT-UT is humidity using auxiliary temperature data from other sources (see Table 2).
[c]Only by simulations [*Di Girolamo et al.*, 2006].

However, to realize the development and deployment, several obstacles have still to be overcome. The current systems are still in experimental mode and have not been designed for continuous and routine operation. The laser technology required for frequency control has just recently been developed. Further extensive tests of laser and optical components are required. Consequently, corresponding systems are still not commercially

available. Additionally, most of the current laser systems are operating in a non-eye-safe spectral domain so that care has to be taken during laser operation by limiting the laser power, setting up a safety zone for aviation around the laser operating region, incorporation of safety radars, etc. It is important to overcome these hurdles in order to take advantage of this unique WV remote sensing technique, for instance, by extending the laser technology to the eye-safe region > 1450 nm. A first attempt has been demonstrated in *Petrova-Mayor et al.* [2008] where also several suitable absorption lines for WVDIAL were identified.

5.3. Comparison of Remote Sensing Techniques and Proposed Sensor Synergy

Tables 2 and 3 summarize the performance of passive and active remote sensing systems, which demonstrated maturity for TD profiling. In the following, these results are discussed with respect to the requirements given in Table 1. For the sake of completeness, also spaceborne remote sensing including the potential of future active remote sensing systems is considered. It is evident that passive remote sensing systems from space are close to the requirements with respect to bias and noise error. However, the vertical resolution of passive IR and MW remote sensing is limited by the widths of the weighting functions close to the ground; these widths are 1–2 km. With near-IR remote sensing, only IWV can be retrieved. Therefore, spaceborne passive remote sensing systems do not fulfill the needs of lower tropospheric TD profiling with respect to the vertical resolution. Potential systems from space may be WVDIAL and TRRL due to their high vertical resolution as well as scalability of power and receiver size.

For lower tropospheric TD profiling, it is necessary to complement the spaceborne passive remote sensing systems by GNSS ROs and by networks of ground-based passive or active TD profilers. Ground-based passive remote sensing systems are less complicated than active systems because they do not require a transmitter. IR spectrometers are slightly more complex than MWRs because of the use of an interferometer to sample the IR spectrum, whereas MWRs use either a filter bank (for simultaneous detection of the downwelling microwave radiance in all frequency channels) or a tunable frequency synthesizer (for serial detection). However, IR spectrometers use two well-characterized blackbodies that are able to maintain the instrument's calibration to better than 1% of the ambient radiance automatically [*Knuteson et al.*, 2004a], whereas MWRs require periodic views of liquid nitrogen cooled blackbodies, which is a manual process, in order to calibrate its internal reference target [e.g., *Maschwitz et al.*, 2013]. Both IR and MWR sensors are all-weather remote sensing systems with compact and very stable setups able for long-term operation and with low power consumption.

Whereas IR retrievals are possible up to the cloud base, MW retrievals are possible through nonprecipitating clouds. The SNR of both systems is limited by the performance of the detector material, the strength of the atmospheric radiation in the frequency range of interest, and the integration time. A further increase of the SNR of the radiance measurements may be possible by using larger receiver areas in combination with sophisticated imaging systems.

Other options are GPS RO measurements and retrievals of WV fields using networks of ground-based GNSS receiver. With respect to RO measurements, recent progress in signal tracking [*Sokolovskiy*, 2001; *Beyerle et al.*, 2006] and retrieval algorithms [*Sokolovskiy et al.*, 2009, 2010] provided a considerable extension of coverage and vertical extent down to 1 km in many regions with a vertical resolution of ≈100 m. Based on the results of *Kursinski and Hajj* [2001] and *Vergados et al.* [2014], the bias of the retrieved WV profiles is 5–10% and the RMS error 10–20%. These results make GPS RO very interesting for all applications mentioned in section 4. However, it is necessary to investigate the accuracy of the inversion of the RO refractivities into lower tropospheric WV profiles in regions with strong refractivity gradients and to specify their error characteristics. Furthermore, the information content of these measurements with respect to the mesoscale variability of WV and *T* fields needs to be explored considering their horizontal footprint of not less than 100 km. Networks of ground-based GNSS receivers are a very interesting option for deriving WV fields by means of tomography or by the assimilation of SIWV in mesoscale models. IWV and STD fields can be derived routinely, which provide important information for comparisons with models and DA. However, only a few studies have attempted to recover the vertical structure of WV fields. Some studies appeared successful [i.e., *Champollion et al.*, 2009] whereas others suggest that tomographic retrievals have very limited information content on the vertical distribution of water vapor [*Meunier et al.*, 2015]. Currently, it is not clear what 3-D resolution and accuracy can be achieved with a specific density and coverage of GNSS receivers. There are different possibilities to provide first guess fields for the retrievals, e.g., from soundings, remote sensing systems, or models. It is urgently necessary to

explore this potential either by impact studies with advanced DA systems using existing networks or by OSSEs simulating artificial GNSS networks.

WVRL and TRRL require high-power laser transmitters operating in the UV and large receiver optics. Thus, the power consumption is significantly higher than that of passive remote sensing. The system setup is more complex, and it is more challenging to realize stable long-term operation. Furthermore, high-power lasers used in Raman lidar systems typically are flash lamp pumped requiring manual intervention approximately monthly as the flash lamps have limited lifetimes; this demands trained operators that are capable of this task. Fortunately, it is possible to replace these lasers by fully diode laser-pumped systems [*Metzendorf et al.*, 2015] with significantly higher efficiency and longer life time but these are expensive.

Even more challenging is the design of laser transmitters for WVDIAL [*Wagner et al.*, 2013a]. However, because of the use of the much stronger elastic scattering signal in DIAL systems, the laser transmitter can operate with an order of magnitude less power to achieve a similar performance as WVRL during the daytime (see Figures 16 and 25). This allows DIAL systems to use low-power, diode-pumped lasers, which have much longer lifetimes than flash lamps and hence less manual intervention [*Spuler et al.*, 2015]. Furthermore, the SNR of lidar measurements can be scaled by increasing laser transmitter power and receiver area leading to higher precision and resolution (see equation (28)).

For realizing compact and operational Raman lidar and DIAL systems, more research and technical development is necessary on laser technology, high-power laser optics, and detector systems. A particular gap is the availability of efficient and compact laser sources in the UV for Raman lidar and in the eye-safe wavelength region > 1450 nm for WVDIAL. Only by overcoming these obstacles and by making these lidar systems commercially available such as is the case for Doppler wind lidar systems, we will be able to realize the potential to deploy these TD lidar systems in large mesoscale networks.

Lidar systems can be set up for all-weather routine operation like ceilometers. However, their range is limited by optically thick clouds and precipitation so that their coverage of meteorological conditions is similar to that of an IR spectrometer. Thus, a combination of lidar and MWR is reasonable for extending the vertical range.

With respect to the vertical resolution, ground-based IR spectrometers are superior to MWR and have the potential to resolve WV and T gradients close to the Earth's surface due to the IR spectrometer's larger information content. A combination of IR and MW is reasonable for extending the IR measurements through clouds. However, both techniques degrade in vertical resolution to 1 km at the ABL top so that WV gradients and T inversion layers can hardly be resolved. The vertical range to get meaningful results is ≈4 km. There are some initial efforts to combine ground-based and space-based passive IR observations in a single retrieval algorithm and hence provide a TD profile throughout the troposphere in cases that are clear sky or have a single cloud layer.

In contrast, Raman lidar and DIAL systems maintain a high vertical resolution of the order of 100 m throughout the lower troposphere. By means of scanning applications a very high vertical resolution can be achieved close to the surface as well. The vertical range of WVDIAL and WVRL as well as TRRL covers the entire troposphere as long as no optically think clouds are limiting the measurements.

The temporal resolution of passive retrievals is typically 5 min. Retrievals at a temporal resolution of 30 s are possible for IR spectrometers whereas MWRs typically use elevation scanning to improve the information content [*Crewell and Löhnert*, 2007], which takes more time. At 5 min resolution and the respective vertical resolution given above, the RMS error of IR and passive remote sensing is 10–20% for WV and ≈1 K for T. The bias can only be disentangled and specified by comparisons with other reference sensors such as high-quality in situ radiosondes and lidar systems. Generally, it has been demonstrated that the bias is $< 10\%$ for WV and < 0.5 K for T profiles. However, not much is known yet concerning the long-term stability of the bias and its dependence on meteorological conditions. In any case, current IR spectrometers and MWRs are able to fulfill most of the needs summarized in Table 1.

For active remote sensing, it is possible to derive the bias by means of systematic error propagation. The results have been confirmed by extensive intercomparisons. For WVDIAL and WVRL, the bias is $< 5\%$ with excellent long-term stability. Theoretically, it should be even $< 2\%$ for WVDIAL [*Späth et al.*, 2014]; however, basically no other reference sensor exists to confirm this performance. The bias for TRRL is < 1 K, but more long-term measurements are still needed in order to investigate its stability.

The precision of WVDIAL and WVRL measurements for the laser transmitter power and receiver areas as well as for the vertical resolutions given in Table 2 is 5–10%. This precision can be realized with temporal averages down to 1–10 s in the daytime CBL. The same holds for TRRL and its capability to resolve T fluctuations and inversions in the CBL. Thus, WVDIAL, WVRL, and TRRL can fulfill basically all requirements summarized in Table 1.

An extension of coverage and long-term operation as well as an increase of network density for TD profiling in all climate regions over land and the oceans is technologically feasible now. A remaining gap is the routine operation of passive and active remote sensing systems on buoys and shipborne platforms. The installation of remote sensors on these platforms is challenging due to a variety of technical problems. Among others, pitching and rolling of ships or buoys may alter the pointing stability of these sensors, affecting their performances. The implementation of motion compensation techniques may therefore be required. These can be realized by vertical gyros continuously measuring the orientation and motion of the platforms in combination with a computer-controlled actively stabilized scanning mechanism [*Hooper and James*, 2000]. Pointing accuracies of 0.1° were achieved in shipborne lidar system for wave heights in the range 3–7 m range, with rolls reaching 20° and pitches reaching 7° [*James and Hooper*, 1995]. The implementation of remote sensing systems on offshore platforms, ships, or buoys has to also face with a faster degradation of some of the optical components included in the transmitting and receiving systems.

Furthermore, it is necessary to explore more in depth the synergy between in situ measurements and observations with remote sensing systems. This will also lead to a technological redundancy for operational purposes. For instance, the combined use of radio soundings, IR and MW passive retrievals, WV and T profiling with lidar, and GNSS RO can contribute to an improved calibration of the sensors and a more robust specification of the bias in the TD profiles [e.g., *Ho et al.*, 2010]. The combination of FTIR and lidar with MWR and GNSS can extend the vertical range in the presence of clouds. A combination of ground-based and spaceborne remote sensing will also contribute to an extension of the vertical range. These examples can be explored based on the methodologies and on the results presented in section 5 as well as Tables 2 and 3.

6. Summary and Outlook

This review article presents an in-depth overview of the current understanding, simulations, and observations of the TD structure of the lower troposphere, which is a key component of the water and energy cycles. Particularly, this review contains a thorough methodological analysis of both passive and active remote sensing of TD profiles with respect to almost all aspects of system performances.

An overview of the importance of high-resolution WV and T profiling is given focusing on (1) radiative transfer as well as water and energy cycles, (2) LSA exchange and feedback, (3) convection initiation, and (4) data assimilation (DA). It is demonstrated that the observations must cover LSA exchange and feedback processes in the ABL including entrainment at the top of the daytime convective boundary layer. Furthermore, the observations must be accurate enough for characterizing the preconvective environment, convection initiation, and the thermodynamic environment of convective systems. The lack of TD profiles with high temporal and vertical resolutions limits progress in all these areas, which affects not only weather and climate research but also various related disciplines such as soil, hydrological, and agricultural sciences.

The greatest challenge is the observation of the WV and T variability at the meso-beta to the meso-gamma scale to address recent advances in Earth system modeling. Over the entire range of nowcasting to short- and medium-range forecasting, the trend in NWP goes toward a considerable increase in model resolution down to the grey zone. This requires the development of new observational capabilities capturing the variability of the WV and T fields with high temporal and vertical resolutions from the surface to the lower troposphere and covering large geographical areas down to the meso-gamma scale. For seasonal to decadal climate processes and simulations, these observations are essential for improving process understanding, measurements of weather statistics, and model verification. This is substantiated by a thorough analysis of the state of the art of weather and climate modeling.

DA of TD profiles has a great potential for pushing numerical weather prediction (NWP) results in the nowcasting range. For optimal impact, the characterization of the observing error covariance matrix under the corresponding meteorological conditions is necessary. Further key challenges are the representation of the

thermodynamic structure of the ABL and the model imbalance at initial time. Both can be addressed by the DA of TD profiles with mesoscale coverage and short latency. Particularly, a well-designed synergy of TD and radar networks will likely lead to a substantial improvement of the impact of pure radar data, as the model imbalance will be reduced by the optimization of the TD environment around convective systems. It is expected that this approach will lead to a substantial extension of the forecast range to initial time with improved forecast skill.

Currently, the TD observations are too sparse to address these issues. A detailed overview of the current observational capabilities is given, and it is confirmed that severe gaps in the measurement of the 3-D WV and T fields exist. Most of the observations are based on passive remote sensing from satellites which have limited vertical resolution and accuracy particularly close to the ground. Active remote sensing techniques based on the GNSS use either RO or retrievals of WV fields using ground-based networks. RO measurements are possible now down to the LT with high vertical but coarse horizontal resolutions. GNSS tomography using ground-based networks or the assimilation of STDs has a very interesting potential to recover 3-D WV fields; however, more research is necessary to understand and to specify the resulting resolutions and accuracies.

Networks of ground-based passive and active remote sensing systems operating in the optical, IR, and MW spectral regions have the potential to close major gaps with respect to lower tropospheric TD profiling. However, these are extremely sparse to date. Potential instruments are passive IR spectrometers, MWRs, and three active remote sensing systems, the WVRL, the WVDIAL, and the TRRL. By means of scanning, both the passive and the active remote sensing systems are able to measure from the Earth's surface to the troposphere. Whereas IR spectrometers provide accurate, vertically resolved retrievals up to cloud bases or 4 km in clear air, MWRs can reach a range of 4 km even in the presence of nonprecipitating clouds. Lidar systems can measure TD profiles with high accuracy as well as higher temporal and vertical resolutions throughout the troposphere in the preconvective environment and the environment around convective systems. Consequently, all these techniques are able to close significant gaps with respect to high-resolution TD profiling in the lower troposphere.

What requirements are needed for a future ground-based network of WV and T observing systems in order to produce a significant impact? This is outlined in an overview of the most important applications of observing systems in Earth system sciences, which can be separated in four areas: (1) Monitoring, (2) verification and calibration, (3) DA, and (4) process studies. The requirements identified are (1) compact setup in combination with low cost for purchase and maintenance, (2) capability of operating these systems in networks, (3) possibility of routine operation in different climate regions, (4) simple data analysis with well-defined error estimates, (5) low bias ($<$2–5% systematic error in WV and <0.5 K in T), and (6) profiling capability with high temporal (10 min) and spatial resolution (a few 100 m) in the ABL up to about 3–4 km with a noise error of $<10\%$.

Particularly, it is important to determine not only mean profiles but also their gradients in the lower troposphere, e.g., for getting accurate estimates of the ABL depth, inversion layers, and combined variables such as the relative humidity or the convection inhibition.

What measurement methodologies have the potential to fulfill all these needs? This is one of the central topics of this review article. It is clear that only remote sensing methods (active and passive) are applicable, as profiles of WV and T must be measured with high temporal and vertical resolution, accuracy, and spatial coverage. The various methodologies are discussed, and it is distinguished between *retrievals* from passive systems and *derivations* from active systems. The resulting temporal and spatial resolutions of the profiles as well as the range are presented.

With respect to GNSS, both GPS RO and ground-based GNSS tomography are solutions for WV profiling in the lower troposphere. WV profiles retrieved with RO are possible down to $\approx$1 km with global coverage but require additional information provided by others sources such as NWP-based temperature and pressure analyses. Except regions with strong refractivity gradients, the quality of the retrievals seems to be high enough to permit measurements of WV profiles with small bias and RMS errors. The vertical resolution is high ($\approx$100 m) but the horizontal footprint is relatively coarse ($\approx$100 km). Networks of ground-based GNSS receivers were also considered particularly taking advantage of STDs where profile information may be retrieved by tomographic techniques or by reanalyses using DA systems.

An extensive analysis of ground-based FTIR, MWR, and lidar methodologies is presented. It turns out that both passive and active remote sensing technologies fulfill most of the requirements. A smaller bias is

realized with lidar techniques because they derive WV and *T* profiles by the unique inversion of the lidar equation. Calibration of TRRL and WVRL is still necessary but an adequate system design will ensure a high reproducibility and stability. WVDIAL does not require a calibration making this technique ideal as reference system. Close to the surface, the vertical resolution of both passive and active remote sensing is very high; however, in passive remote sensing it degrades close to the ABL top. The vertical and temporal resolutions of active remote sensing are higher from the ABL to the middle troposphere. Both passive and active techniques provide a characterization of the error covariance matrix in real time. However, due to the lower bias of active remote sensing, its characterization and separation of the precision may be more meaningful. In passive remote sensing, an analysis error covariance matrix is provided as well but the resulting RMS error can contain a bias, which depends on the choice of the first guess database and the meteorological conditions. Extensive research is still necessary with respect to the comparison of the performance of passive and active remote sensing systems in different climate regions and under different meteorological conditions and their synergy.

It is extremely urgent to develop and to apply new observational TD profiling capabilities. Considering the costs for setup, operation, and maintenance, ground-based networks with high density and large coverage are most promising to accelerate our knowledge of energy and water cycles from regional to global scales. Synergetic networks of passive and active remote sensing systems calibrated by TRRL, WVRL, and WVDIAL are the starting point. Whereas both IR spectrometers and MWRs are commercially available now for use in operational networks, lidar systems require some additional investment to advance their operational readiness and make them commercially available. However, an optimal design of future networks of remote sensing systems that accounts not only for the setup, operation, and maintenance but also for the expected impact based on measurement resolutions and accuracies as well as density and coverage is still lacking.

This critical situation demands the following:

1. A strong impulse to the development of low-cost TD profilers both for operation on the land surface and over the oceans also on shipborne platforms and buoys. Networks fulfilling the requirements derived in section 4 provide *T* and WV profiles that can be applied (a) as reference for monitoring as well as for verification of other sensors and for calibration of satellite data and (b) for DA with very short latency with minimum requirements set to background information (including their error covariance matrices) in dependence of different atmospheric conditions.
2. Execution of extensive OSEs and OSSEs for network design and impact studies using existing profiler data and potential future networks. These studies are fundamental for detecting critical locations of maximum impact for DA (mesoscale targeting) and to investigate its dependence of network coverage and density. Furthermore, an optimized network design with respect to representative measurements in complex terrain will be very beneficial for climate research such as monitoring and model verification.
3. Research on the synergetic use of remote sensing systems with respect to coverage, spatial and temporal resolution, error characterization, and technological redundancy as well as with respect to their synergy with other observing systems.

It is highly recommended to start a joint activity of NWP, space, and research centers to actively support these developments because they will be the most important partners for the design and long-term operation of these networks and the biggest beneficiary of their products.

Appendix A: Error Definitions

Based on the ISO 5725 standard, we define accuracy as the combination of the bias (systematic error or trueness) and the noise error (precision) of a measurement with respect to the true value (see Figure A1). The bias refers to the closeness of the mean of the measurement to the truth. This systematic deviation cannot be removed by averaging. The bias can be derived by theoretical analyses, e.g., by end-to-end simulation of the measurement process. In this case, the bias is constrained to a specified range but typically not to its sign. The bias can also be specified by comparisons with a reference standard, which existence we assume in the following. Here the comparison of a set of reference profiles with the remote sensing measurements is used to derive the RMS error of the observations.
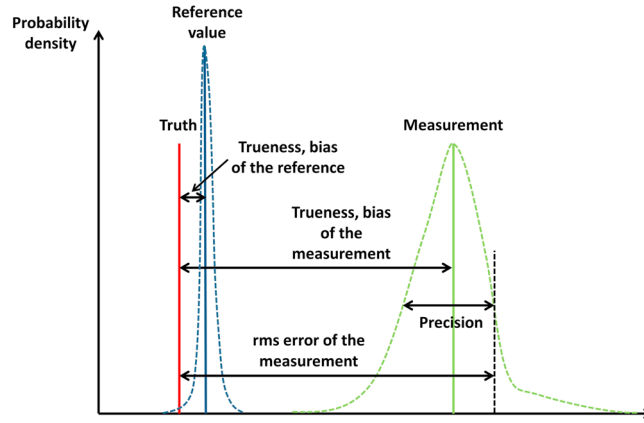
Figure A1. Definition of measurement variables and errors used throughout this work for an appropriate comparison or the performance of different TD sensors. The dashed lines indicate the shapes of the PDFs of the measurements.

The RMS error of a passive remote sensing retrieval can be approximated by the analysis error covariance matrix of the variational retrieval [*Rodgers*, 2000]. This assumes both a Gaussian error distribution of the first guess database as well as of the noise error of the measured radiances and the radiative transfer forward operator.

The noise error is given by the shape of the probabilistic density function (PDF) of the measurement process (see Figure A1). The width of the PDF is often estimated by the noise error standard deviation. The estimation of the noise error covariance matrix is not only essential for retrieval characterizations but also for DA applications.

In contrast to the bias, the noise error can be reduced by improving the SNR of the measured signals. For active remote sensing, the noise error can be estimated theoretically, e.g., by noise error propagation. Furthermore, by means of temporal or spectral analyses of the measured time series, the noise error of single profiles measured with active remote sensing can be estimated [*Lenschow et al.*, 2000; *Wulfmeyer et al.*, 2010]. For passive remote sensing retrievals it seems to be challenging—if not impossible—to separate noise errors and bias on a routine basis, if comparisons with reference sensors are not available. Generally, we can write

$$q_{\text{ref}} = q_{\text{tr}} + B_{\text{ref}} + \varepsilon_{\text{ref}} \tag{A1}$$

and

$$q_m = q_{\text{tr}} + B_m + \varepsilon_m, \tag{A2}$$

where q_{ref} is the mean of the reference measurement, q_{tr} is the true value, B_{ref} is the bias (trueness), and ε_{ref} is the noise contribution. The corresponding definitions hold for the measurement q_m. The bias of measurement can be estimated by taking the difference Δ between the reference and the measurement:

$$\Delta = q_{\text{ref}} - q_m = B_{\text{ref}} - B_m + \varepsilon_{\text{ref}} - \varepsilon_m$$
$$\Delta \approx -B_m, \quad \text{if} \quad |B_{\text{ref}}|, |\varepsilon_{\text{ref}}|, |\varepsilon_m| << |B_m|. \tag{A3}$$

Thus, the bias of a single TD profile can be determined, if the noise errors of the reference and the measurements are negligible. This is possible with special, low-noise in situ sensors and active remote sensing systems. Usually a bias statistics is derived using a large set of comparisons under different meteorological conditions. In this case

$$\overline{\Delta} = \overline{q}_{\text{ref}} - \overline{q}_m = \overline{B}_{\text{ref}} - \overline{B}_m + \overline{\varepsilon}_{\text{ref}} - \overline{\varepsilon}_m \cong \overline{B}_{\text{ref}} - \overline{B}_m \approx -\overline{B}_m, \quad \text{if} \quad |B_{\text{ref}}| << |B_m|. \tag{A4}$$

This demonstrates the importance of the development of reference standards for TD profiling.

By a statistical analysis of the intercomparison data also the RMS error $\sqrt{\sigma_\Delta^2}$ can be estimated:

$$\sigma_\Delta^2 \equiv \frac{1}{N}\sum_i (\Delta_i)^2 = \frac{1}{N}\sum_i \left(B_{\text{ref},i} - B_{m,i} + \varepsilon_{\text{ref},i} - \varepsilon_{m,i}\right)^2$$

$$\sigma_\Delta^2 = \frac{1}{N}\sum_i \left[\left(B_{\text{ref},i} - B_{m,i}\right)^2 + 2\left(B_{\text{ref},i} - B_{m,i}\right)\left(\varepsilon_{\text{ref},i} - \varepsilon_{m,i}\right) + \left(\varepsilon_{\text{ref},i} - \varepsilon_{m,i}\right)^2\right] \tag{A5}$$

$$\sigma_\Delta^2 \approx \left(\overline{B}_{\text{ref}} - \overline{B}_m\right)^2 + \sigma_{\text{ref}}^2 + \sigma_m^2 \approx \overline{B}_m^2 + \sigma_m^2, \quad \text{if} \quad |B_{\text{ref}}|, \sigma_{\text{ref}} << |B_m|, \sigma_m.$$

The last expression holds, if the noise errors of the reference and the measurement are uncorrelated, which should generally be the case. This expression also confirms that the RMS error, which is only defined for a large intercomparison data set, is a combination of bias and precision. If the last relation in (A5) is valid

$$\sigma_\Delta^2 \approx \overline{\Delta}^2 + \sigma_m^2 \quad ; \text{ hence,} \quad \sigma_m^2 \approx \sigma_\Delta^2 - \overline{\Delta}^2 \tag{A6}$$

so that a separation of bias and noise errors is possible by combining the results of equations (A4) and (A5).

8. List of Acronyms

2-D, 3-D, 4-D	two-dimensional, three-dimensional, four-dimensional
3-DVAR	three-dimensional variational analysis
4-DVAR	four-dimensional variational analysis
ABL	atmospheric boundary layer
AERI	atmospheric emitted radiance interferometer
agl	above ground level
AIRS	Atmospheric Infrared Sounder
AMSR-E	Advanced Microwave Scanning Radiometer–EOS
AMSU-A	Advanced Microwave Sounding Unit-A
AMV	atmospheric motion vector
ARM	Atmospheric Radiation Measurement Program
AROME	limited area weather forecast model of Météo-France
ATMS	Advanced Technology Microwave Sounder
AVHRR	advanced very high resolution radiometer
BASIL	Università della Basilicata
BERTHA	Backscatter, Extinction, lidar Ratio, Temperature and Humidity profiling Apparatus
BLUE	Best Linear Unbiases Estimator
CAMEX	Convection and Moisture Experiment
CBL	Convective Atmospheric Boundary Layer
CEOS	Committee on Earth Observations Satellites
CHAMP	Challenging Mini-satellite Payload
CI	convection initiation
CMC	Canadian Meteorological Center
CMIP5	Coupled Model Intercomparison Project Phase 5
CM-SAF	Satellite Application Facility on Climate Monitoring
CNRS	Centre National de la Recherche Scientifique
COPS	Convective and Orographically-induced Precipitation Study
CORDEX	COordinated Regional climate Downscaling EXperiment
COSMIC	Constellation Observing System for Meteorology, Ionosphere and Climate
CrIS	Cross-Track Infrared Sounder
CSIP	Convective Storm Initiation Project
DA	data assimilation
DIAL	differential absorption lidar
DICE	Diurnal Coupling Experiment
DLR	German Aerospace Center (Deutsches Zentrum für Luft- und Raumfahrt)
DMSP	Defense Meteorological Satellite Program
DOAS	differential optical absorption spectroscopy
D-PHASE	Demonstration of Probabilistic Hydrological and Atmospheric Simulation of flood Events in the Alpine region
DWD	German Meteorological Service (Deutscher Wetterdienst)
EARLINET	European Aerosol Research Lidar Network
ECMWF	European Centre for Medium-Range Weather Forecasts
E-GVAP	EUMETNET GNSS Water Vapor Program

EKF	extended Kalman filter
En3-DVAR	ensemble three-dimensional variational analysis
En4-DVAR	ensemble four-dimensional variational analysis
EnKF	ensemble Kalman filter
ENVISAT	Environmental Satellite
EOS	Earth Observing System
EPOS	Earth Parameter and Orbit determination System
ERA-40	ECMWF Re-Analysis of 40 years
ERA-Interim	ECMWF-Interim
ESA	European Space Agency
EU	European Union
EUMETNET	European Meteorological Network
EUMETSAT	European Organisation for the Exploitation of Meteorological Satellites
FSU	Florida State University
FTIR	IR Fourier transform spectrometer
GABLS	GEWEX Atmospheric Boundary Layer Study
GCM	general circulation model
GCOM-W	Global Change Observation Mission-Water
GCOS	Global Climate Observing System
GDAP	GEWEX Data and Assessment Panel
GEO	Group on Earth Observations
GEOSS	Global Earth Observing System of Systems
GEWEX	Global Energy and Water Exchanges Project
GFZ	Geoforschungszentrum Potsdam
GLASS	Global Land/Atmosphere System Study
GMI	Global Microwave Imager
GNSS	Global Navigation Satellite System
GOES	Geostationary Operational Environmental Satellite
GOS	Global Observing System
GPM	Global Precipitation Mission
GPS	Global Positioning System
GRACE	Gravity Recovery and Climate Experiment
GRUAN	GCOS Reference Upper Air Network
GSFC	Goddard Space Flight Center
GTS	Global Telecommunication System
GVaP	Global Water Vapor Project
HATPRO	Humidity and Temperature PROfiler
HIRLAM	HIgh Resolution Limited Area Model
HIRS	High Resolution Infrared Radiation Sounder
HOAPS	Hamburg Ocean Atmosphere Parameters and Fluxes from Satellite Data
HSB	Humidity Sounder for Brazil
HSRL	High-spectral Resolution Lidar
HyMeX	Hydrological Cycle in the Mediterranean Experiment
IASI	Infrared Atmospheric Sounding Interferometer
IfT	Leibniz Institute for Tropospheric Research
IGBP	International Geosphere-Biosphere Program
IHOP_2002	International H_2O Project
IL	interfacial layer
iLEAPS	Integrated Land Ecosystem - Atmosphere Processes Study
IOP	Intensive Observations Period
IPCC	Intergovernmental Panel on Climate Change
IPM	Institute of Physics and Meteorology, University of Hohenheim, Stuttgart, Germany
IR	infrared
JAXA	Japan Aerospace Exploration Agency

JMA	Japan Meteorological Agency
JWGFVR	Joint Working Group on Forecast Verification Research
KF	Kalman filter
KIT	Karlsruhe Institute for Technology
LASE	Laser Atmospheric Sensing Experiment
LEO	Lower Earth Orbiting
LES	large-eddy simulation
lidar	light detection and ranging
LoCo	local coupling
LSA	land-surface-atmosphere
LS	lower stratosphere
LT	lower troposphere
MERIS	Medium Resolution Imaging Spectrometer Instrument
MetOp	Meteorological Operational satellite
MHS	Microwave Humidity Sounder
MM4	Mesoscale Model 4
MM5	Mesoscale Model 5
MODIS	Moderate Resolution Imaging Spectroradiometer
MPI	Max Planck Institute
MSG	Meteosat Second Generation
MSU	Microwave Sounding Unit
MT	middle troposphere
MTG	Meteosat Third Generation
MW	microwave
MWR	microwave radiometer
NASA	National Aeronautics and Space Administration
NCAR	National Center for Atmospheric Research, Boulder, CO, USA
NCDC	National Climatic Data Center
NCEP	National Center for Environmental Prediction
NDACC	Network for the Detection of Atmospheric Composition Change
Nd:YAG	neodymium-doped yttrium aluminum garnet
NMS	National Meteorological Service
NOAA	National Oceanic and Atmospheric Administration, Boulder, CO, USA
NOAH-MP	National Centers for Environmental Prediction (NCEP) - Oregon State University (Dept of Atmospheric Sciences) - Air Force - Hydrology Lab of the National Weather Service – Multi-Physics land surface model
NPP	National Polar-orbiting Partnership
NWP	Numerical Weather Prediction
OLCI	Ocean and Land Colour Imager
OSE	Observing System Experiment
OSSE	Observing System Simulation Experiment
PDF	probability density function
POES	Polar Orbiting Environmental Satellite
QPF	Quantitative Precipitation Forecasting
Radar	radio detection and ranging
RALMO	Raman Lidar for Meteorological Observations
RAMSES	Raman Lidar for Atmospheric Moisture Sensing
RASC	Raman Lidar Japan
RASS	radio acoustic sounding system
RHI	range-height indicator
RMS	root-mean-square
RO	radio occultation
RR	rotational Raman
RRL	rotational Raman lidar

RTE	Radiative Transfer Equation
RUC	Rapid Update Cycle
SAC-C	Scientific Application Satellite-C
SAF	Satellite Application Facilities
SAR	Synthetic Aperture Radar
SCOPE-CM	Sustained and Coordinated Processing of Environmental Satellite Data for Climate Monitoring
SEVIRI	Spinning Enhanced Visible and Infrared Imager
SGP	Southern Great Plains
SRL	Scanning Raman Lidar
SSM	Special Sensor Microwave
SSM/I	Special Sensor Microwave Imager
SSMIS	Special Sensor Microwave Imager Sounder
T	temperature
TD	thermodynamic
TIROS	Television Infrared Observational Satellite Program
TRRL	temperature rotational Raman lidar
UHF	ultrahigh frequency
UHOH	University of Hohenheim
UK	United Kingdom
UKMO	UK Met Office
US	United States
UT	upper troposphere
UV	ultraviolet
VAR	Variational
VHF	very high frequency
Voxel	VOlume pixel
WACMOS	Water Cycle Multi-mission Observation Strategy
WACMOS-ET	WACMOS Evapotranspiration
WALES	WAter vapour Lidar Experiment in Space
WALI	Water vapour and Aerosol Lidar
WCRP	World Climate Research Program
WMO	World Meteorological Organization
WRF	Weather Research and Forecasting Model
WV	water vapor
WVDIAL	Water-Vapor Differential Absorption Lidar
WVRL	water vapor Raman lidar
WWRP	World Weather Research Program
WWW	World Weather Watch

9. List of Variables and Constants

A	Analysis error covariance matrix of a DA system or a retrieval
A_{tel}	Telescope area
a	TRRL fit coefficient
az	GNSS azimuth angle
B	Model error covariance matrix
B_{ref}, B_m	Biases of a reference and standard measurements
B_v	Planck's function
b	TRRL fit coefficient
C	Refractive index gradient of air
c	Speed of light

c_p	Specific heat capacity of dry air
DFS	Cumulative degrees of freedom
DB	Scattering Doppler broadening function
d	GNSS data sample
$d\sigma_{Ram}/d\Omega$	Differential Raman scattering cross section
E_L	Lidar laser transmitter single-shot pulse energy
ET	Evapotranspiration
el	GNSS signal elevation angle
F_N	Net radiation absorbed by the surface and the canopy layer
F_s	Downward flux of energy at the surface
F_R	Lidar receiver filter function
F_{TOA}	Net radiation at the top of the atmosphere
f	TRRL fit coefficient
$\boldsymbol{G}$	GNSS length partitioning matrix
G	Ground heat flux
G_n, G_e	GNSS signal gradient functions
g	Acceleration due to gravity
h	Planck's constant
$\boldsymbol{H}$	Model forward observation operator
H	Heat storage in the soil-canopy layer
HS	Surface sensible heat flux
I	Ionospheric delay of GNSS signal
I_ν	Radiative power in dependence of frequency ν
IWV	Integrated water-vapor content
J	Rotational quantum number
$\boldsymbol{K}$	Weighting matrix
K_{WV}, K_T	WVRL and TRRL system calibration coefficients
k	Boltzmann's constant
L	Latent heat of evaporation
L_{GNSS}	GNSS carrier phase length
l_{GNSS}	Geometric distance between GNSS transmitter and receiver
$\boldsymbol{M}$	Model forward operator
M_h, M_w	Hydrostatic and wet GNSS mapping function
m	Water-vapor mixing ratio
N_{mol}, N_{WV}	Molecular and water-vapor number densities
n, i, k	Integers
O	Overlap function
P	Precipitation
PW	Precipitable water
P_0, P_L	Lidar transmitter peak power and average power
$P_S, P_{Ram}, P_{Ram, WV}, P_{Ram, N2}$	Lidar backscatter signal power, Raman lidar signal power, Raman lidar water-vapor and nitrogen signal powers
P_B	Lidar background signal power
PoR	Postfit residual
p, p_0	Pressure, surface pressure
$\vec{Q}$	Vertically integrated water-vapor flux
Q	Rotational Raman lidar signal ratio
q	Specific humidity
q_{ref}, q_m	Values of reference and standard measurements
q_{tr}	True value of measurement
$\boldsymbol{R}$	Observation error covariance matrix
RH	Relative humidity
r	Range
$\vec{R}_0$	Surface water runoff

S	Moisture storage in the soil-canopy layer
SNR	Signal-to-noise ratio
STD	GNSS slant total delay
SIWV	Slant integrated water vapor
S_L	Normalized laser spectrum
T, T_M	Temperature, atmospheric mean temperature
TOA	Top of the atmosphere
t, t_r, t_s	Time as well as GNSS receiver and transmitter clock errors
$\vec{V}$	Horizontal wind vector
$\boldsymbol{W}_{\text{GNSS}}$	Matrix related to GNSS errors
w'	Vertical wind fluctuation
z	height agl
ZHD	GNSS zenith hydrostatic delay
ZTD	GNSS zenith total delay
ZWD	GNSS zenith wet delay
α_{v}, α_v	Extinction coefficient of species i and overall extinction coefficient in dependence of frequency v
$\alpha_{\text{mol},v}$, $\alpha_{\text{par},v}$	Atmospheric extinction coefficient, separated in molecular and particle extinction coefficients in dependence of frequency v
$\alpha_{G,v}$, $\alpha_{\text{WV},v}$	Absorption coefficient of a gas or WV in dependence of frequency v
β_{v}, $\beta_{\text{mol},v}$, $\beta_{\text{par},v}$	Lidar backscatter coefficient, separated in molecular and particle backscatter in dependence of frequency v
$\beta_{\text{Ram},v}$	Raman backscatter coefficient in dependence of frequency v
Δ	Bias between measurements or between a measurement and the true value
ΔR	Range resolution
Δt	Laser transmitter pulse duration
Δv_{Ram}	Frequency shift due to Raman scattering
$\Delta\tau_{\text{WV}}$	Optical thickness of WV between online and offline frequencies in range cell ΔR
δt	Averaging time
ε, ε_{ref}, ε_m	Noise error as well as noise errors of reference and standard measurements
λ	Wavelength
λE	Surface latent heat flux
μ	Weighting coefficient for GNSS tomographic retrieval
v	Electromagnetic wave frequency
v_0, v_R	Lidar laser transmitter frequency and repetition rate
v_{Ram}	Raman-shifted frequency of laser transmitter
v_B	Brunt-Vaisälä frequency
ξ	Lidar system efficiency
Π	Function of atmospheric mean temperature
ρ_{WV}, ρ_{WV}', ρ_0	Water-vapor density and its fluctuation, and first guess water-vapor density field for GNSS tomography
ρ_{est}	GNSS water-vapor density estimate
ρ_{LW}	Density of liquid water
σ, σ_m, σ_{NWV}	Noise error standard deviation, noise error of mixing ratio or water-vapor number density measurement
$\sigma_{\text{WV},v}$	WV absorption cross section in dependence of frequency v
$\sigma_{\text{Ram},v}$, $\sigma_{RR,Ji,n}$	Raman backscattering cross section in dependence of frequency v, rotational Raman backscattering cross section in dependence of rotational quantum number J_i and molecule type n
τ_v	Optical thickness in dependence of frequency v
θ	Potential temperature
Φ	Potential energy of the atmosphere
Ω	Solid angle
Γ_v	Transmittance is dependence of frequency v

References

Abo, M. (2005), Resonance scattering lidar, in *Lidar: Range-Resolved Optical Remote Sensing of the Atmosphere*, edited by C. Weitkamp, Springer, New York.

Ackerman, T. P., and G. M. Stokes (2003), The atmospheric radiation measurement program—To predict reliably what increased greenhouse gases will do to global climate, we have to understand the crucial role of clouds, *Phys. Today*, 56, 38–46.

Adam, S., T. Schwitalla, E. Hammann, A. Behrendt, and V. Wulfmeyer (2015), First assimilation of rotational Raman lidar temperature data, 27th International Laser Radar Conference, New York, 5–10 Jul.

Adams, D. K., et al. (2011), A dense GNSS meteorological network for observing deep convection in the Amazon, *Atmos. Sci. Lett.*, 12, 207–212, doi:10.1002/asl.312.

Adams, D. K., S. I. Gutman, K. L. Holub, and D. S. Pereira (2013), GNSS observations of deep convective time scales in the Amazon, *Geophys. Res. Lett.*, 40, 2818–2823, doi:10.1002/grl.50573.

Alexander, L. V., et al. (2006), Global observed changes in daily climate extremes of temperature and precipitation, *J. Geophys. Res.*, 111, D05109, doi:10.1029/2005JD006290.

Althausen, D., D. Müller, A. Ansmann, U. Wandinger, H. Hube, E. Clauder, and S. Zörner (2000), Scanning 6-wavelength 11-channel aerosol lidar, *J. Atmos. Oceanic Technol.*, 17, 1469–1482.

Amato, U., and C. Serio (2000), Remote sensing of the atmosphere from high spectral resolution infrared radiation, *Recent Res. Dev. Geophys.*, 3, 17–36.

Andersson, A., K. Fennig, C. Klepp, S. Bakan, H. Grassl, and J. Schulz (2010), The Hamburg Ocean Atmosphere Parameters and Fluxes from Satellite Data—HOAPS-3, *Earth Syst. Sci. Data*, 2, 215–234, doi:10.5194/essd-2-215-2010.

Andersson, E., et al. (2005), Assimilation and modeling of the atmospheric hydrological cycle in the ECMWF forecasting system, *Bull. Am. Meteorol. Soc.*, 86, 387–402.

Angevine, W. M., and W. L. Ecklund (1994), Errors in radio acoustic sounding of temperature, *J. Atmos. Oceanic Technol.*, 11, 837–842.

Angevine, W. M., W. L. Ecklund, D. A. Carter, K. S. Gage, and K. P. Moran (1994), Improved radio acoustic sounding techniques, *J. Atmos. Oceanic Technol.*, 11, 42–49.

Anthes, R. A. (2011), Exploring Earth's atmosphere with radio occultation: Contributions to weather, climate, and space weather, *Atmos. Meas. Tech.*, 4, 1077–1103, doi:10.5194/amt-4-1077-2011.

Anthes, R. A., et al. (2008), The COSMIC/FORMOSAT-3 mission: Early results, *Bull. Am. Meteorol. Soc.*, 89, 313–333, doi:10.1175/BAMS-89-3-313.

Ao, C. O., G. A. Hajj, T. K. Meehan, D. Dong, B. A. Iijima, A. Mannucci, and E. R. Kursinski (2009), Rising and setting GPS occultations by use of open-loop tracking, *J. Geophys. Res.*, 114, D04101, doi:10.1029/2008JD010483.

Ao, C. O., D. E. Waliser, S. K. Chan, J.-L. Li, B. Tian, F. Xie, and A. J. Mannucci (2012), Planetary boundary layer heights from GPS radio occultation refractivity and humidity profiles, *J. Geophys. Res.*, 117, D16117, doi:10.1029/2012JD017598.

Apituley, A., K. M. Wilson, C. Potma, H. Volten, and M. de Graaf (2009), Performance assessment and application of Caeli—A high-performance Raman lidar for diurnal profiling of water vapour, aerosols and clouds. Proceedings of the 8th International Symposium on Tropospheric Profiling, Delft, Netherlands, 19–23 Oct.

Arshinov, Y., S. Bobrovnikov, I. Serikov, A. Ansmann, U. Wandinger, D. Althausen, I. Mattis, and D. Müller (2005), Daytime operation of a pure rotational Raman lidar by use of a Fabry-Perot interferometer, *Appl. Opt.*, 44, 3593–3603, doi:10.1364/AO.44.003593.

Askne, J. I. H., and B. G. Skoog (1983), Atmospheric water-vapor profiling by ground-based radiometry at 22 and 183 GHz, *IEEE Trans. Geosci. Remote Sens.*, GE-21, 320–323.

Askne, J. I. H., and E. R. Westwater (1986), A review of ground-based remote sensing of temperature and moisture by passive microwave radiometers, *IEEE Trans. Geosci. Remote Sens.*, GE-24, 340–352.

August, T., D. Klaes, P. Schlüssel, T. Hultberg, M. Crapeau, A. Arriaga, and X. Calbet (2012), IASI on Metop-A: Operational level 2 retrievals after five years in orbit, *J. Quant. Spectros. Radiat. Transfer*, 113, 1340–1371.

Aumann, H. H., et al. (2003), AIRS/AMSU/HSB on the Aqua mission: Design, science objectives, data products, and processing systems, *IEEE Trans. Geosci. Remote Sens.*, 41, 253–264.

Barbosa, H. M. J., B. Barja, T. Pauliquevis, D. A. Gouveia, P. Artaxo, C. G. Cirino, R. M. N. Santos, and A. B. Oliveira (2014), A permanent Raman lidar station in the Amazon: Description, characterization, and first results, *Atmos. Meas. Tech.*, 7, 1745–1762, doi:10.5194/amt-7-1745-2014.

Barker, D., et al. (2012), The Weather Research and Forecasting model's community variational/ensemble data assimilation system: WRFDA, *Bull. Am. Meteorol. Soc.*, 93, 831–843, doi:10.1175/BAMS-D-11-00167.1.

Bastin, S., C. Champollion, O. Bock, P. Drobinski, and F. Masson (2005), On the use of GPS tomography to investigate water vapor variability during a Mistral/sea breeze event in southeastern France, *Geophys. Res. Lett.*, 32, L05808, doi:10.1029/2004GL021907.

Bauer, H., H.-S. Bauer, V. Wulfmeyer, M. Wirth, B. Mayer, G. Ehret, D. Summa, and P. Di Girolamo (2004), End-to-end simulation of the performance of WALES: Forward module, Proceedings of the 22nd International Laser Radar Conference, ESA SP-561, 1011–1014.

Bauer, H.-S., V. Wulfmeyer, T. Schwitalla, F. Zus, and M. Grzeschik (2011), Operational assimilation of GPS slant path delay measurements into the MM5 4DVAR system, *Tellus A*, 63, 263–282, doi:10.1111/j.1600-0870.2010.00489.x.

Bauer, P. (2009), 4D-Var assimilation of MERIS total column water-vapour retrievals over land, *Q. J. R. Meteorol. Soc.*, 135, 1852–1862, doi:10.1002/qj.509.

Behrendt, A. (2005), Temperature measurements with lidar, in *Lidar: Range-Resolved Optical Remote Sensing of the Atmosphere, Springer Series in Optical Sciences*, vol. 102, edited by C. Weitkamp, pp. 273–305, Springer, New York.

Behrendt, A., and J. Reichardt (2000), Atmospheric temperature profiling in the presence of clouds with a pure rotational Raman lidar by use of an interference-filter-based polychromator, *Appl. Opt.*, 39, 1372–1378.

Behrendt, A., T. Nakamura, M. Onishi, R. Baumgart, and T. Tsuda (2002), Combined Raman lidar for the measurement of atmospheric temperature, water vapor, particle extinction coefficient, and particle backscatter coefficient, *Appl. Opt.*, 41, 7657–7666.

Behrendt, A., T. Nakamura, and T. Tsuda (2004), Combined temperature lidar for measurements in the troposphere, stratosphere, and mesosphere, *Appl. Opt.*, 43, 2930–2939.

Behrendt, A., et al. (2007a), Intercomparison of water vapor data measured with lidar during IHOP_2002. Part 1: Airborne to ground-based lidar systems and comparisons with chilled-mirror hygrometer radiosondes, *J. Atmos. Oceanic Technol.*, 24, 3–21, doi:10.1175/JTECH1924.1.

Behrendt, A., et al. (2007b), Intercomparison of water vapor data measured with lidar during IHOP_2002. Part 2: Airborne to airborne systems, *J. Atmos. Oceanic Technol.*, 24, 22–39, doi:10.1175/JTECH1925.1.

Behrendt, A., V. Wulfmeyer, A. Riede, G. Wagner, S. Pal, H. Bauer, M. Radlach, and F. Späth (2009), 3-dimensional observations of atmospheric humidity with a scanning differential absorption lidar, in *Remote Sensing of Clouds and the Atmosphere XIV, SPIE Conf. Proc.*, vol. 7475, edited by R. H. Picard et al., SPIE, Berlin, doi:10.1117/12.835143.

Behrendt, A., et al. (2011), Observation of convection initiation processes with a suite of state-of-the-art research instruments during COPS IOP8b, *Q. J. R. Meteorol. Soc.*, *137*, 81–100, doi:10.1002/qj.758.

Behrendt, A., V. Wulfmeyer, E. Hammann, S. K. Muppa, and S. Pal (2015), Profiles of second- to third-order moments of turbulent temperature fluctuations in the convective boundary layer: First measurements with rotational Raman lidar, *Atmos. Chem. Phys.*, *15*, 5485–5500, doi:10.5194/acp-15-5485-2015.

Bengtsson, L., K. I. Hodges, and S. Hagemann (2004), Sensitivity of the ERA40 reanalysis to the observing system: Determination of the global atmospheric circulation from reduced observations, *Tellus A*, *56*, 456–471, doi:10.1111/j.1600-0870.2004.00079.x.

Bennartz, R., and J. Fischer (2001), Retrieval of columnar water vapour over land from backscattered solar radiation using the Medium Resolution Imaging Spectrometer, *Remote Sens. Environ.*, *78*, 274–283.

Bennitt, G. V., and A. Jupp (2012), Operational assimilation of GPS zenith total delay observations into the Met Office numerical weather prediction models, *Mon. Weather Rev.*, *140*, 2706–2719, doi:10.1175/MWR-D-11-00156.1.

Best, M. (2014), Initial results from the Diurnal Land/Atmosphere Coupling Experiment (DICE), 7th International Scientific Conference on the Global Water and Energy Cycle, Den Haag, Netherlands, 14–17 Jul.

Bevis, M., S. Businger, T. A. Herring, C. Rocken, R. A. Anthes, and R. Ware (1992), GPS meteorology: Remote sensing of atmospheric water vapor using the Global Positioning System, *J. Geophys. Res.*, *97*, 15,787–15,801, doi:10.1029/92JD01517.

Beyerle, G., T. Schmidt, J. Wickert, S. Heise, M. Rothacher, G. König-Langlo, and K. B. Lauritsen (2006), Observations and simulations of receiver-induced refractivity biases in GPS radio occultation, *J. Geophys. Res.*, *111*, D12101, doi:10.1029/2005JD006673.

Bhawar, R., et al. (2011), The water vapour intercomparison effort in the framework of the convective and orographically-induced precipitation study: Airborne-to-ground-based and airborne-to-airborne lidar systems, *Q. J. R. Meteorol. Soc.*, *137*, 325–348, doi:10.1002/qj.697.

Bielli, S., M. Grzeschik, E. Richard, C. Flamant, C. Champollion, C. Kiemle, M. Dorninger, and P. Brousseau (2012), Assimilation of water-vapour airborne lidar observations: Impact study on the COPS precipitation forecasts, *Q. J. R. Meteorol. Soc.*, *138*, 1652–1667, doi:10.1002/qj.1864.

Blackwell, W. J., L. J. Bickmeier, R. V. Leslie, M. L. Pieper, J. E. Samra, C. Surussavadee, and C. A. Upham (2011), Hyperspectral microwave atmospheric sounding, *IEEE Trans. Geosci. Remote Sens.*, *49*, 128–142, doi:10.1109/TGRS.2010.2052260.

Bluestein, H. B., B. A. Albrecht, R. M. Hardesty, W. D. Rust, D. Parsons, R. Wakimoto, and R. M. Rauber (2001), Meeting summary: Ground-based mobile instrument workshop summary, 23–24 February 2000, Boulder, Colo., *Bull. Am. Meteorol. Soc.*, *82*, 681–694, doi:10.1175/1520-0477(2001)082<0681:MSGMIW>2.3.CO;2.

Bluestein, H. B., J. B. Houser, M. M. French, J. C. Snyder, G. D. Emmitt, I. PopStefanija, C. Baldi, and R. T. Bluth (2014), Observations of the boundary layer near tornadoes and in supercells using a mobile, collocated, pulsed Doppler lidar and radar, *J. Atmos. Oceanic Technol.*, *31*, 302–325, doi:10.1175/JTECH-D-13-00112.1.

Bock, O., E. Doerflinger, F. Masson, A. Walpersdorf, J. Van Baelen, J. Tarniewicz, M. Troller, A. Somieski, A. Geiger, and B. Buerki (2004), GPS water vapor tomography: Description and first results of the ESCOMPTE field experiment, *Phys. Chem. Earth*, *29*, 149–157, doi:10.1016/j.atmosres.2004.04.003.

Bodine, D., D. Michaud, R. D. Palmer, P. L. Heinselman, J. Brotzge, N. Gasperoni, B. L. Cheong, M. Xue, and J. Gao (2011), Understanding radar refractivity: Sources of uncertainty, *J. Appl. Meteorol. Climatol.*, *50*, 2543–2560, doi:10.1175/2011JAMC2648.1.

Boehm, J., A. Niell, P. Tregoning, and H. Schuh (2006), Global Mapping Function (GMF): A new empirical mapping function based on numerical weather model data, *Geophys. Res. Lett.*, *33*, L07304, doi:10.1029/2005GL025546.

Boniface, K., C. Champollion, J. Chery, V. Ducrocq, C. Rocken, E. Doerflinger, and P. Collard (2012), Potential of shipborne GPS atmospheric delay data for prediction of Mediterranean intense weather events, *Atmos. Sci. Lett.*, *13*, 250–256, doi:10.1002/asl.391.

Bösenberg, J. (1998), Ground-based differential absorption lidar for water-vapor profiling: Methodology, *Appl. Opt.*, *37*, 3845–3860.

Brenot, H., V. Ducrocq, A. Walpersdorf, C. Champollion, and O. Caumont (2006), GPS zenith delay sensitivity evaluated from high resolution NWP simulations of the 8–9th September 2002 flashflood over southeastern France, *J. Geophys. Res.*, *111*, D15105, doi:10.1029/2004JD005726.

Brenot, H., A. Walpersdorf, M. Reverdy, J. van Baelen, V. Ducrocq, C. Champollion, F. Mas-son, E. Doerflinger, P. Collard, and P. Giroux (2014), A GPS network for tropospheric tomography in the framework of the Mediterranean hydrometeorological observatory Cévennes-Vivarais (southeastern France), *Atmos. Meas. Tech.*, *7*, 553–578, doi:10.5194/amt-7-553-2014.

Brocard, E., R. Philipona, A. Haefele, G. Romanens, A. Mueller, D. Ruffieux, V. Simeonov, and B. Calpini (2013), Raman Lidar for Meteorological Observations, RALMO—Part 2: Validation of water vapor measurements, *Atmos. Meas. Tech.*, *6*, 1347–1358.

Brosseau, P., L. Berre, F. Bouttier, and G. Desroziers (2011), Background-error covariances for a convective-scale data-assimilation system: AROME–France 3D-Var, *Q. J. R. Meteorol. Soc.*, *137*, 409–422, doi:10.1002/qj.750.

Browell, E. V., T. D. Wilkerson, and T. J. Illrath (1979), Water vapor differential absorption lidar development and evaluation, *Appl. Opt.*, *18*, 3474–3483.

Browell, E. V., S. Ismail, and B. E. Grossmann (1991), Temperature sensitivity of differential absorption lidar measurements of water vapor in the 720-nm region, *Appl. Opt.*, *30*, 1517–1524.

Browell, E. V., et al. (1996), LASE validation experiment, in *Advances in Atmospheric Remote Sensing With Lidar*, edited by A. Ansmann et al., pp. 289–295, Springer, Berlin.

Browning, K. A., et al. (2007), The Convective Storm Initiation Project, *Bull. Am. Meteorol. Soc.*, *88*, 1939–1955, doi:10.1175/BAMS-88-12-1939.

Cadeddu, M. P., G. E. Peckham, and C. Gaffard (2002), The vertical resolution of ground-based microwave radiometers analyzed through a multiresolution wavelet technique, *IEEE Trans. Geosci. Remote Sens.*, *40*, 531–540.

Cadeddu, M. P., J. C. Liljegren, and A. Pazmany (2007), Measurements and retrievals from a new 183-GHz water vapor radiometer in the Arctic, *IEEE Trans. Geosci. Remote Sens.*, *45*, 2759–2777.

Cadeddu, M. P., J. C. Liljegren, and D. D. Turner (2013), The atmospheric radiation measurement (ARM) program network of microwave radiometers: Instrumentation, data, and retrievals, *Atmos. Meas. Tech.*, *6*, 2359–2372, doi:10.5194/amt-6-2359-2013.

Capelle, V., A. Chédin, E. Péquignot, P. Schlüssel, S. M. Newman, and N. A. Scott (2012), Infrared continental surface emissivity spectra and skin temperature retrieved from IASI observations over the tropics, *J. Appl. Meteorol. Climatol.*, *51*, 1164–1179.

Cardinali, C., and S. Healy (2014), Impact of GPS radio occultation measurements in the ECMWF system using adjoint-based diagnostics, *Q. J. R. Meteorol. Soc.*, *140*, 2315–2320, doi:10.1002/qj.2300.

Cayla, F.-R. (1993), IASI infrared interferometer for operations and research, in *High Spectral Resolution Infrared Remote Sensing for Earth's Weather and Climate Studies*, *NATO ASI Ser.*, vol. 19, edited by A. Chédin, M. T. Chahine, and N. A. Scott, pp. 9–19, Springer, Berlin.

Cess, R. D. (2005), Water vapor feedback in climate models, *Science*, *310*, 795–796.

Champollion, C., F. Masson, M.-N. Bouin, A. Walpersdorf, E. Doerflinger, O. Bock, and J. Van Baelen (2005), GPS water vapour tomography: Preliminary results from the ESCOMPTE field experiment, *Atmos. Res.*, *74*, 253–274, doi:10.1016/j.atmosres.2004.04.003.

Champollion, C., C. Flamant, O. Bock, F. Masson, D. D. Turner, and T. Weckwerth (2009), Mesoscale GPS tomography applied to the 12 June 2002 convective initiation event of IHOP_2002, *Q. J. R. Meteorol. Soc.*, *135*, 645–662, doi:10.1002/qj.386.

Chazette, P., F. Marnas, and J. Totems (2013), The mobile Water vapor Aerosol Raman LIdar and its implication in the frame of the HyMeX and ChArMEx programs: Application to a dust transport process, *Atmos. Meas. Tech. Discuss.*, *6*, 10,653–10,698, doi:10.5194/amtd-6-10653-2013.

Chédin, A., M. T. Chahine, and N. A. Scott (Eds) (1993), *High Spectral Resolution Infrared Remote Sensing for Earth's Weather and Climate Studies*, *NATO ASI Ser.*, vol. 19, Springer, Berlin.

Ching, J., R. Rotunno, M. LeMone, A. Martilli, B. Kosovic, P. A. Jimenez, and J. Dudhia (2014), Convectively induced secondary circulations in fine-grid mesoscale numerical weather prediction models, *Mon. Weather Rev.*, *142*, 3284–3302, doi:10.1175/MWR-D-13-00318.1.

Ciesielski, P. E., et al. (2014), Quality-controlled upper-air sounding dataset for DYNAMO/CINDY/AMIE: Development and corrections, *J. Atmos. Oceanic Technol.*, *31*, 741–764, doi:10.1175/JTECH-D-13-00165.1.

Cimini, D., F. Nasir, E. R. Westwater, V. H. Payne, D. D. Turner, E. J. Mlawer, M. L. Exner, and M. P. Cadeddu (2009), Comparison of ground-based millimeter-wave observations and simulations in the Arctic winter, *IEEE Trans. Geosci. Remote Sens.*, *47*, 3098–3106.

Cimini, D., E. R. Westwater, and A. J. Gasiewski (2010), Temperature and humidity profiling in the arctic using ground-based millimeter-wave radiometry and 1DVAR, *IEEE Transact. Geosci. Remote Sens.*, *48*, 1381–2010.

Cimini, D., et al. (2012), An international network of ground-based microwave radiometers for the assimilation of temperature and humidity profiles into NWP model, 9th International Symposium on Tropospheric Profiling (ISTP), L'Aquila, Italy, Abstract P45, 3–7 Sept.

Cimini, D., et al. (2014), A data assimilation experiment of temperature and humidity profiles from an international network of ground-based microwave radiometers, Proc. Microrad 2014, Pasadena, 24–27 March, 2014.

Clayton, A. M., A. C. Lorenc, and D. M. Barker (2013), Operational implementation of a hybrid ensemble/4D-Var global data assimilation system at the Met Office, *Q. J. R. Meteorol. Soc.*, *139*, 1445–1461, doi:10.1002/qj.2054.

Collard, A. D., and A. P. McNally (2009), Assimilation of infrared atmospheric sounding interferometer radiances at ECMWF, *Q. J. R. Meteorol. Soc.*, *135*, 1044–1058.

Cooney, J. (1972), Measurement of atmospheric temperature profiles by Raman backscatter, *J. Appl. Meteorol.*, *11*, 108–112.

Corsmeier, U., et al. (2011), Driving processes for deep convection over complex terrain: A multi-scale analysis of observations from COPS-IOP 9c, *Q. J. R. Meteorol. Soc.*, *137*, 137–155, doi:10.1002/qj.754.

Crevoisier, C., et al. (2014), Towards IASI-New Generation (IASI-NG): Impact of improved spectral resolution and radiometric noise on the retrieval of thermodynamic, chemistry and climate variables, *Atmos. Meas. Tech.*, *7*, 4367–4385, doi:10.5194/amt-7-4367-2014.

Crewell, S., and U. Löhnert (2007), Accuracy of boundary layer temperature profiles retrieved with multifrequency multiangle microwave radiometry, *IEEE Trans. Geosci. Remote Sens.*, *45*, 2195–2201.

Crewell, S., et al. (2004), The BALTEX Bridge Campaign: An integrated approach for a better understanding of clouds, *Bull. Am. Meteorol. Soc.*, *85*, 1565–1584.

Crook, N. A. (1996), Sensitivity of moist convection forced by boundary layer processes to low-level thermodynamic fields, *Mon. Weather Rev.*, *124*, 1767–1785.

Cucurull, L., J. C. Derber, R. Treadon, and R. J. Purser (2007), Assimilation of global positioning system radio occultation observations into NCEP's global data assimilation system, *Mon. Weather Rev.*, *135*, 3174–3193, doi:10.1175/MWR3461.1.

Dai, A. G. (2006), Recent climatology, variability, and trends in global surface humidity, *J. Clim.*, *19*, 3589–3606.

Dailey, P. S., and R. G. Fovell (1999), Numerical simulation of the interaction between the sea-breeze front and horizontal convective rolls. Part I: Offshore ambient flow, *Mon. Weather Rev.*, *127*, 858–878.

Davis, J. L., T. A. Herring, I. I. Shapiro, A. E. Rogers, and G. Elgered (1985), Geodesy by radio interferometry: Effects of the atmospheric modelling errors on estimates of baseline length, *Radio Sci.*, *20*, 1593–1607, doi:10.1029/RS020i006p01593.

Davis, J. L., G. Elgered, A. E. Niell, and C. E. Kuehn (1993), Ground-based measurement of gradients in the "wet" radio refractivity of air, *Radio Sci.*, *28*, 1003–1018, doi:10.1029/93RS01917.

Dee, D. P. (2005), Bias and data assimilation, *Q. J. R. Meteorol. Soc.*, *131*, 3323–3343.

Dee, D. P., et al. (2011), The ERA-Interim reanalysis: Configuration and performance of the data assimilation system, *Q. J. R. Meteorol. Soc.*, *137*, 553–597, doi:10.1002/qj.828.

Demory, M.-E., P. L. Vidale, M. J. Roberts, P. Berrisford, J. Strachan, R. Schiemann, and M. S. Mizielinski (2013), The role of horizontal resolution in simulating drivers of the global hydrological cycle, *Clim. Dyn.*, *42*, 2201–2225, doi:10.1007/s00382-013-1924-4.

Demoz, B. B., D. Starr, K. D. Evans, A. R. Lare, D. N. Whiteman, G. Schwemmer, R. A. Ferrare, J. E. M. Goldsmith, and S. E. Bisson (2005), The cold front of 15 April 1994 over the central United States. Part I: Observations, *Mon. Weather Rev.*, *133*, 1525–1543.

Demoz, B., et al. (2006), The dryline on 22 May 2002 during IHOP-2002: Convective-scale measurements at the profiling site, *Mon. Weather Rev.*, *134*, 294–310.

Dessler, A. E. (2010), A determination of the cloud feedback from climate variations over the past decade, *Science*, *330*, 1523–1527, doi:10.1126/science.1192546.

Dessler, A. E., and S. C. Sherwood (2009), A matter of humidity, *Science*, *323*, 1020–1021.

Dessler, A. E., Z. Zhang, and P. Yang (2008), Water-vapor climate feedback inferred from climate fluctuations, *Geophys. Res. Lett.*, *35*, L20704, doi:10.1029/2008GL035333.

Di Girolamo, P., R. Marchese, D. N. Whiteman, and B. B. Demoz (2004a), Rotational Raman lidar measurements of atmospheric temperature in the UV, *Geophys. Res. Lett.*, *31*, L01106, doi:10.1029/2003GL018342.

Di Girolamo, P., D. Summa, H. Bauer, V. Wulfmeyer, A. Behrendt, B. Mayer, M. Wirth, and C. Kiemle (2004b), Simulation of the performance of WALES based on an end-to-end model, 22nd International Laser Radar Conference, Matera, Italy, 12–12 Jul.

Di Girolamo, P., D. Summa, V. Wulfmeyer, H. Bauer, H. S. Bauer, A. Behrendt, M. Wirth, and B. Mayer (2004c), Development of an end-to-end model to simulate the performances of a water vapour DIAL system in space, Final Report, ESA ESTEC Contract No. 16993/03/NL/FF.

Di Girolamo, P., A. Behrendt, and V. Wulfmeyer (2006), Spaceborne profiling of atmospheric temperature and particle extinction with pure rotational Raman lidar and of relative humidity in combination with differential absorption lidar: Performance simulations, *Appl. Opt.*, *45*, 2474–2494, doi:10.1364/AO.45.002474.

Di Girolamo, P., A. Behrendt, C. Kiemle, V. Wulfmeyer, H. Bauer, D. Summa, A. Dörnbrack, and G. Ehret (2008), Simulation of satellite water vapour lidar measurements: Performance assessment under real atmospheric conditions, *Remote Sens. Environ.*, *112*, 1552–1568, doi:10.1016/j.rse.2007.08.008.

Di Girolamo, P., D. Summa, and R. Ferretti (2009a), Multiparameter Raman lidar measurements for the characterization of a dry stratospheric intrusion event, *J. Atmos. Oceanic Technol.*, *26*, 1742–1762, doi:10.1175/2009JTECHA1253.1.

Di Girolamo, P., D. Summa, R. F. Lin, T. Maestri, R. Rizzi, and G. Masiello (2009b), UV Raman lidar measurements of relative humidity for the characterization of cirrus cloud microphysical properties, *Atmos. Chem. Phys.*, *9*, 8799–8811, doi:10.5194/acp-9-8799-2009.

Dierer, S., M. Arpagaus, A. Seifert, E. Avgoustoglou, R. Dumitrache, F. Grazzini, P. Mercogliano, M. Milelli, and K. Starosta (2009), Deficiencies in quantitative precipitation forecasts: Sensitivity studies using the COSMO model, *Meteorol. Z.*, *18*, 631–645, doi:10.1127/0941-2948/2009/0420.

Dinoev, T., V. Simeonov, Y. Arshinov, S. Bobrovnikov, P. Ristori, B. Calpini, M. Parlange, and H. van den Bergh (2013), Raman Lidar for Meteorological Observations, RALMO—Part 1: Instrument description, *Atmos. Meas. Tech.*, *6*, 1329–1346, doi:10.5194/amt-6-1329-2013.

DLR (2005), Requirement definition for future DIAL instruments, Final Report. Gerhard Ehret, and Christoph Kiemle (Eds.), ESA RFQ/3-10880/03/NL/FF.

Doherty, S. J., et al. (2009), Lessons learned from IPCC AR4: Scientific developments needed to understand, predict, and respond to climate change, *Bull. Am. Meteorol. Soc.*, *90*, 497–513, doi:10.1175/2008BAMS2643.1.

Donlon, C., et al. (2012), The Global Monitoring for Environment and Security (GMES) Sentinel-3 mission, *Remote Sens. Environ.*, *120*, 37–57, doi:10.1016/j.rse.2011.07.024.

Ducrocq, V., D. Ricard, J. P. Lafore, and F. Orain (2002), Storm-scale numerical rainfall prediction for five precipitating events over France: On the importance of the initial humidity field, *Weather Forecasting*, *17*, 1236–1256.

Ebert, E., et al. (2013), Progress and challenges in forecast verification, *Meteorol. Appl.*, *20*, 130–139, doi:10.1002/met.1392.

Ehret, G., K. P. Hoinka, J. Stein, A. Fix, C. Kiemle, and G. Poberaj (1999), Low stratospheric water vapor measured by an airborne DIAL, *J. Geophys. Res.*, *104*, 31,351–31,360, doi:10.1029/1999JD900959.

Ehret, U., E. Zehe, V. Wulfmeyer, K. Warrach-Sagi, and J. Liebert (2012), HESS Opinions—Should we apply bias correction to global and regional climate model data?, *Hydrol. Earth Syst. Sci.*, *16*, 3391–3404, doi:10.5194/hess-16-3391-2012.

Ertel, K., H. Linné, and J. Bösenberg (2005), Injection-seeded pulsed Ti: Sapphire laser with novel stabilization scheme and capability of dual wavelength operation, *Appl. Opt.*, *44*, 5120–5126.

European Space Agency (ESA) (2001), WALES—WAter Vapour Lidar Experiment in Space, The Five Candidate Earth Explorer Core Missions, European Space Agency, Report for Assessment, ESA SP-1257, vol. II.

European Space Agency (ESA) (2004), WALES—The WAter vapour Lidar Experiment in Space, European Space Agency, Report for Mission Selection, ESA SP-1279, vol. III.

Fabry, F., C. Frush, I. Zawadzki, and A. Kilambi (1997), On the extraction of near-surface index of refraction using radar phase measurements from ground targets, *J. Atmos. Oceanic Technol.*, *14*, 978–987.

Feltz, W. F., W. L. Smith, R. O. Knuteson, H. E. Revercomb, H. M. Woolf, and H. B. Howell (1998), Meteorological applications of temperature and water vapor retrievals from the ground-based Atmospheric Emitted Radiance Interferometer (AERI), *J. Appl. Meteorol.*, *37*, 857–875.

Feltz, W. F., W. L. Smith, H. B. Howell, R. O. Knuteson, H. Woolf, and H. E. Revercomb (2003), Near-continuous profiling of temperature, moisture, and atmospheric stability using the Atmospheric Emitted Radiance Interferometer (AERI), *J. Appl. Meteorol.*, *42*, 584–597.

Ferrare, R. A., et al. (2004), Characterization of upper-troposphere water vapor measurements during AFWEX using LASE, *J. Atmos. Oceanic Technol.*, *21*, 1790–1808.

Ferrare, R. A., et al. (2006), Evaluation of daytime measurements of aerosols and water vapor made by an operational Raman lidar over the Southern Great Plains, *J. Geophys. Res.*, *111*, D05S08, doi:10.1029/2005JD005836.

Fiocco, G., G. Beneditti-Michelangeli, K. Maischberger, and E. Madonna (1971), Atmospheric temperature from scattered laser light, *Nature*, *229*, 78.

Flentje, H., A. Dörnbrack, G. Ehret, A. Fix, C. Kiemle, G. Poberaj, and M. Wirth (2005), Water vapor heterogeneity related to tropopause folds over the North Atlantic revealed by airborne water vapor differential absorption lidar, *J. Geophys. Res.*, *110*, D03115, doi:10.1029/2004JD004957.

Flores, A., G. Ruffini, and A. Rius (2000), 4D tropospheric tomography using GPS slant wet delays, *Ann. Geophys.*, *18*, 223–234, doi:10.1007/s00585-000-0223-7.

Fujita, M., F. Kimura, K. Yoneyama, and M. Yoshizaki (2008), Verification of precipitable water vapor estimated from shipborne GPS measurements, *Geophys. Res. Lett.*, *35*, L13803, doi:10.1029/2008GL033764.

Furumoto, J., K. Kurimoto, and T. Tsuda (2003), Continuous observations of humidity profiles with the MU radar-RASS combined with GPS and radiosonde measurements, *J. Atmos. Oceanic Technol.*, *20*, 23–41.

Gao, B. C., and Y. J. Kaufman (2003), Water vapor retrievals using Moderate Resolution Imaging Spectroradiometer (MODIS) near-infrared channels, *J. Geophys. Res.*, *108*(D13), 4389, doi:10.1029/2002JD003023.

Gayler, S., J. Ingwersen, E. Priesack, T. Wöhling, V. Wulfmeyer, and T. Streck (2013), Assessing the relevance of subsurface processes for the simulation of evapotranspiration and soil moisture dynamics with CLM3.5: Comparison with field data and crop model simulations, *Environ. Earth Sci*, *69*, 415–427, doi:10.1007/s12665-013-2309-z.

Gayler, S., T. Wöhling, M. Grzeschik, J. Ingwersen, H.-D. Wizemann, H. Petra, S. Attinger, T. Streck, and V. Wulfmeyer (2014), Incorporating dynamic root growth enhances the performance of Noah-MP ensemble simulations at two contrasting winter wheat field sites, *Water Res. Res.*, *50*, 1337–1356, doi:10.1002/2013WR014634.

Gendt, G., G. Dick, C. Reigber, M. Tomassini, Y. Liu, and M. Ramatschi (2004), Near real time GPS water vapor monitoring for numerical weather prediction in Germany, *J. Meteor. Soc. Jpn.*, *82*, 361–370.

Gérard, E., D. G. H. Tan, L. Garand, V. Wulfmeyer, G. Ehret, and P. Di Girolamo (2004), Major advances foreseen in humidity profiling from WALES (Water Vapour Lidar Experiment in Space), *Bull. Am. Meteorol. Soc.*, *84*, 237–251.

Giez, A., G. Ehret, R. L. Schwiesow, K. J. Davis, and D. H. Lenschow (1999), Water vapor flux measurements from ground-based vertically pointed water vapor differential absorption and Doppler lidars, *J. Atmos. Oceanic Technol.*, *16*, 237–250.

Giorgi, F., C. Jones, and G. R. Asrar (2009), Addressing climate information needs at the regional level: The CORDEX framework, *WMO Bull.*, *58*, 175–183.

Goldsmith, J. E. M., F. H. Blair, S. E. Bisson, and D. D. Turner (1998), Turn-key Raman lidar for profiling atmospheric water vapor, clouds, and aerosols, *Appl. Opt.*, *37*, 4979–4990.

Gossard, E. E., D. E. Wolfe, and B. B. Stankov (1999), Measurement of humidity profiles in the atmosphere by the global positioning system and radar wind profilers, *J. Atmos. Oceanic Technol.*, *16*, 156–164.

Grzeschik, M., H.-S. Bauer, and V. Wulfmeyer (2008), Four-dimensional variational analysis of water-vapor Raman lidar data and their impact on mesoscale forecasts, *J. Atmos. Oceanic Technol.*, *25*, 1437–1453, doi:10.1175/2007JTECHA974.1.

Guerova, G., J.-M. Bettems, E. Brockmann, and C. Matzler (2006), Assimilation of COST 716 near-real time GPS data in the nonhydrostatic limited area model used at MeteoSwiss, *Meteorol. Atmos. Phys.*, *91*, 149–164, doi:10.1007/s00703-005-0110-6.

Guidard, V., N. Fourrié, P. Brousseau, and F. Rabier (2011), Impact of IASI assimilation at global and convective scales and challenges for the assimilation of cloudy scenes, *Q. J. R. Meteorol. Soc.*, *137*, 1975–1987, doi:10.1002/qj.928.

Guo, P., Y.-H. Kuo, S. V. Sokolovskiy, and D. H. Lenschow (2011), Estimating atmospheric boundary layer depth using COSMIC radio occultation data, *J. Atmos. Sci.*, *68*, 1703–1713, doi:10.1175/2011JAS3612.1.

Gutman, S. I., S. R. Sahm, S. G. Benjamin, B. E. Schwarz, K. L. Holub, J. Q. Stewart, and T. L. Smith (2004), Rapid retrieval and assimilation of ground based GPS precipitable water observations at the NOAA Forecast Systems Laboratory: Impact on weather forecasts, *J. Meteorol. Soc. Jpn.*, *82*, 351–360.

Haddeland, I., et al. (2011), Multimodel estimate of the global terrestrial water balance: Setup and first results, *J. Hydrometeorol.*, *12*, 869–884.

Hagemann, S., B. Machenhauer, R. Jones, O. B. Christensen, M. Déqué, D. Jacob, and P. L. Vidale (2004), Evaluation of water and energy budgets in regional climate models applied over Europe, *Clim. Dyn.*, *23*, 547–567.

Hagen, M., J. van Baelen, and E. Richard (2011), Influence of the wind profile on the initiation of convection in mountainous terrain, *Q. J. R. Meteorol. Soc.*, *137*, 224–235, doi:10.1002/qj.784.

Hair, J. W., L. M. Caldwell, D. A. Krueger, and C.-Y. She (2001), High-spectral-resolution lidar with iodine-vapor filters: Measurement of atmospheric-state and aerosol profiles, *Appl. Opt.*, *40*, 5280–5294.

Hammann, E., A. Behrendt, F. Le Mounier, and V. Wulfmeyer (2015), Temperature profiling of the atmospheric boundary layer with rotational Raman lidar during the HD(CP)[2] Observational Prototype Experiment, *Atmos. Chem. Phys.*, *15*, 2867–2881, doi:10.5194/acp-15-2867-2015.

Han, Y., et al. (2013), Suomi NPP CrIS measurements, sensor data record algorithm, calibration and validation activities, and record data quality, *J. Geophys. Res. Atmos.*, *118*, 12,734–12,748, doi:10.1002/2013JD020344.

Harding, R., et al. (2011), WATCH: Current knowledge of the terrestrial global water cycle, *J. Hydrometeorol.*, *12*, 1149–1156.

Harnisch, F., M. Weissmann, C. Cardinali, and M. Wirth (2011), Experimental assimilation of DIAL water vapour observations in the ECMWF global model, *Q. J. R. Meteorol. Soc.*, *137*, 1532–1546, doi:10.1002/qj.851.

Hartung, D. C., J. A. Otkin, R. A. Petersen, D. D. Turner, and W. F. Feltz (2011), Assimilation of surface-based boundary layer profiler observations during a cool-season weather event using an observing system simulation experiment. Part II: Forecast assessment, *Mon. Weather Rev.*, *139*, 2327–2346.

Hauchecorne, A., M. L. Chanin, P. Keckhut, and D. Nedeljkovic (1992), Lidar monitoring of the temperature in the middle and lower atmosphere, *Appl. Phys. B*, *55*, 29–34.

Healy, S., J. Wickert, G. Michalak, T. Schmidt, and G. Beyerle (2007), Combined forecast impact of GRACE-A and CHAMP GPS radio occultation bending angle profiles, *Atmos. Sci. Lett.*, *8*, 43–50, doi:10.1002/asl.149.

Held, I. M., and B. J. Soden (2000), Water vapor feedback and global warming, *Annu. Rev. Energy Environ.*, *25*, 441–475.

Hennemuth, B., A. Weiss, J. Bösenberg, D. Jacob, H. Linné, G. Peters, and S. Pfeifer (2008), Quality assessment of water cycle parameters in REMO by radar-lidar synergy, *Atmos. Chem. Phys.*, *8*, 287–308.

Hilton, F., N. C. Atkinson, S. J. English, and J. R. Eyre (2009), Assimilation of IASI at the Met Office and assessment of its impact through observing system experiments, *Q. J. R. Meteorol. Soc.*, *135*, 495–505, doi:10.1002/qj.379.

Hilton, F., et al. (2012), Hyperspectral Earth observation from IASI: Five years of accomplishments, *Bull. Am. Meteorol. Soc.*, *93*, 347–370, doi:10.1175/BAMS-D-11-00027.1.

Ho, S.-P., X. Zhou, Y.-H. Kuo, D. Hunt, and J.-H. Wang (2010), Global evaluation of radiosonde water vapor systematic biases using GPS radio occultation from COSMIC and ECMWF analysis, *Remote Sens.*, *2*, 1320–1330.

Hofmann-Wellenhof, B., H. Lichtenegger, and J. Collins (1992), Global Positioning System. Theory and Practice, Springer, Wien.

Hohenegger, C., P. Brockhaus, C. S. Bretherton, and C. Schär (2009), The soil moisture-precipitation feedback in simulations with explicit and parameterized convection, *J. Clim.*, *22*, 5003–5020.

Holtslag, A. A. M., et al. (2013), Stable atmospheric boundary layers and diurnal cycles: Challenges for weather and climate models, *Bull. Am. Meteorol. Soc.*, *94*, 1691–1706.

Hooper, W. P., and J. E. James (2000), Lidar observations of ship spray plumes, *J. Atmos. Sci.*, *57*, 2649–2655, doi:10.1175/1520-0469.

Hua, D., M. Uchida, and T. Kobayashi (2005), Ultraviolet Rayleigh-Mie lidar with Mie-scattering correction by Fabry-Perot etalons for temperature profiling of the troposphere, *Appl. Opt.*, *44*, 1305–1314, doi:10.1364/AO.44.001305.

Huang, H. L., W. L. Smith, and H. M. Woolf (1992), Vertical resolution and accuracy of atmospheric infrared sounding spectrometers, *J. Appl. Meteorol.*, *31*, 265–274.

Huntington, T. G. (2006), Evidence for intensification of the global water cycle: Review and synthesis, *J. Hydrol.*, *319*, 83–95.

International Geosphere-Biosphere Program (2006), Science plan and implementation strategy, IGBP Report No. 55. IGBP Secretariat, Stockholm, 76 pp.

Integrated Land Ecosystem-Atmosphere Processes Study (2005), Science plan and implementation strategy, IGBP Report No. 54. IGBP Secretariat, Stockholm, 52 pp.

Intergovernmental Panel on Climate Change (2013), Climate Change 2013: The physical science basis, in *5th Assessment Report IPCC WGI AR5*, edited by T. F. Stocker et al., Cambridge Univ. Press, Cambridge, U. K.

Intergovernmental Panel on Climate Change (2014), Climate Change 2014: Impacts, adaptation, and vulnerability, 5th Assessment Report IPCC WGII AR5 Technical Summary. Coordinating Lead Authors: C. Field, V. Barros, K. Mach, and M. Mastrandrea, download from: [Available at http://www.ipcc.ch/report/ar5/wg2, Geneva, Switzerland.]

Ismail, S., and E. V. Browell (1989), Airborne and spaceborne lidar measurements of water vapor profiles: A sensitivity analysis, *Appl. Opt.*, *28*, 3603–3614.

James, J. E., and W. P. Hooper (1995), *Beam Pointing Stabilization for a Shipboard Volume Imaging Lidar*, Naval Research Laboratory, Washington, D. C., 20375–5320, NRL/MR/7220-95-7646.

Jarvinen, H., R. Eresma, H. Vedel, K. Salonen, S. Niemel, and J. de Vries (2007), A variational data assimilation system for ground-based GPS slant delays, *Q. J. R. Meteorol. Soc.*, *133*, 969–980, doi:10.1002/qj.79.

Jiménez, P. A., J. Dudhia, J. F. González-Rouco, J. Navarro, J. P. Montávez, and E. García-Bustamante (2012), A revised scheme for the WRF surface layer formulation, *Mon. Weather Rev.*, *140*, 898–918.

Joo, S., J. Eyre, and R. Marriott (2013), The impact of Metop and other satellite data within the Met Office global NWP system using adjoint-based sensitivity method, *Mon. Weather Rev.*, *141*, 3331–3342.

Kadygrov, E. N., and D. R. Pick (1998), The potential for temperature retrieval from an angular-scanning single-channel microwave radiometer and some comparisons with in situ observations, *Meteorol. Appl.*, *5*, 393–404.

Kalthoff, N., K. Träumner, B. Adler, S. Späth, A. Behrendt, A. Wieser, J. Handwerker, F. Madonna, and V. Wulfmeyer (2013), Dry and moist convection in the boundary layer over the Black Forest—A combined analysis of in situ and remote sensing data, *Meteorol. Z.*, *22*, 445–461.

Kamineni, R., T. N. Krishnamurti, R. A. Ferrare, S. Ismail, and E. V. Browell (2003), Impact of high resolution water vapor cross-sectional data on hurricane forecasting, *Geophys. Res. Lett.*, *30*(5), 1234, doi:10.1029/2002GL016741.

Kamineni, R., T. N. Krishnamurti, S. Pattnaik, E. V. Browell, S. Ismail, and R. A. Ferrare (2006), Impact of CAMEX-4 datasets for hurricane forecasts using a global model, *J. Atmos. Sci.*, *63*, 151–174.

Kawabata, T., T. Kuroda, H. Seko, and K. Saito (2011), A c-Resolving 4DVAR assimilation experiment for a local heavy rainfall event in the Tokyo metropolitan area, *Mon. Weather Rev.*, *139*, 1911–1931, doi:10.1175/2011MWR3428.1.

Kawabata, T., Y. Shori, H. Seko, and K. Saito (2013), A numerical study on a mesoscale convective system over a subtropical island with 4D-Var assimilation of GPS slant total delays, *J. Meteorol. Soc. Jpn.*, *91*, 705–721.

Kawabata, T., K. Ito, and K. Saito (2014a), Recent progress of the NHM-4DVAR towards a super-high resolution data assimilation, *Sci. Online Lett. Atmos.*, *10*, 145–149, doi:10.2151/sola.2014-030.

Kawabata, T., H. Iwai, H. Seko, Y. Shoji, K. Saito, S. Ishii, and K. Mizutani (2014b), Cloud-resolving 4D-Var assimilation of Doppler wind lidar data on a meso-gamma-scale convective system, *Mon. Weather Rev.*, *142*, 4484–4498, doi:10.1175/MWR-D-13-00362.1.

Keil, C., A. Röpnack, G. C. Craig, and U. Schumann (2008), Sensitivity of quantitative precipitation forecast to height dependent changes in humidity, *Geophys. Res. Lett.*, *35*, L09812, doi:10.1029/2008GL033657.

Kiehl, J. T., and K. E. Trenberth (1997), Earth's annual global mean energy budget, *Bull. Am. Meteorol. Soc.*, *78*, 197–208.

Kiemle, C., M. Kästner, and G. Ehret (1995), The convective boundary layer structure from lidar and radiosonde measurements during the EFEDA '91 campaign, *J. Atmos. Oceanic Technol.*, *12*, 771–782.

Kiemle, C., G. Ehret, A. Giez, K. J. Davis, D. H. Lenschow, and S. P. Oncley (1997), Estimation of boundary layer humidity fluxes and statistics from airborne differential absorption lidar (DIAL), *J. Geophys. Res.*, *102*, 29,189–29,204, doi:10.1029/97JD01112.

Kingsmill, D. E. (1995), Convection initiation associated with a sea-breeze front, a gust front, and their collision, *Mon. Weather Rev.*, *123*, 2913–2933.

Klaus, V., L. Bianco, C. Gaffard, M. Matabuena, and T. J. Hewison (2006), Combining UHF radar wind profiler and microwave radiometer for the estimation of atmospheric humidity profiles, *Meteorol. Z.*, *15*, 87–97.

Kleespies, T. J. (2007), Relative information content of the Advanced Technology Microwave Sounder and the combination of the Advanced Microwave Sounding Unit and the Microwave Humidity Sounder, *IEEE Trans. Geosci. Remote Sens.*, *45*, 2224–2227.

Knuteson, R. O., et al. (2004a), Atmospheric emitted radiance interferometer. Part I: Instrument design, *J. Atmos. Oceanic Technol.*, *21*, 1763–1776.

Knuteson, R. O., et al. (2004b), Atmospheric emitted radiance interferometer. Part II: Instrument performance, *J. Atmos. Oceanic Technol.*, *21*, 1777–1789.

Knutti, R., and J. Sedláček (2013), Robustness and uncertainties in the new CMIP5 climate model projections, *Nat. Clim. Change*, *3*, 369–373, doi:10.1038/nclimate1716.

Köpken, C., G. Kelly, and J.-N. Thépaut (2004), Assimilation of Meteosat radiance data within the 4D-Var system at ECMWF: Assimilation experiments and forecast impact, *Q. J. R. Meteorol. Soc.*, *130*, 2277–2292, doi:10.1256/qj.02.230.

Kotlarski, S., et al. (2014), Regional climate modeling on European scales: A joint standard evaluation of the EURO-CORDEX RCM ensemble, *Geosci. Model Dev.*, *7*, 1297–1333, doi:10.5194/gmd-7-1297-2014.

Kuo, Y.-H., Y.-R. Guo, and E. R. Westwater (1993), Assimilation of precipitable water measurements into a mesoscale numerical model, *Mon. Weather Rev.*, *121*, 1215–1238, doi:10.1175/1520-0493(1993)121<1215:AOPWMI>2.0.CO;2.

Kursinski, E. R., and G. A. Hajj (2001), A comparison of water vapor derived from GPS occultations and global weather analyses, *J. Geophys. Res.*, *106*, 1113–1138, doi:10.1029/2000JD900421.

Kursinski, E. R., G. A. Haji, K. R. Hardy, J. T. Schofield, and R. Linfield (1997), Observing Earth's atmosphere with radio occultation measurements using the Global Positioning System, *J. Geophys. Res.*, *102*, 23,429–23,465, doi:10.1029/97JD01569.

Labbouz, L., J. Van Baelen, F. Tridon, M. Reverdy, M. Hagen, M. Bender, G. Dick, T. Gorgas, and C. Planche (2013), Precipitation on the lee side of the Vosges Mountains: Multi-instrumental study of one case from the COPS campaign, *Meteorol. Z.*, *4*, 413–432.

Le Marshall, J., et al. (2006), Improving global analysis and forecasting with AIRS, *Bull. Am. Meteorol. Soc.*, *87*, 891–894, doi:10.1175/BAMS-87-7-891.

Leblanc, T., and I. S. McDermid (2008), Accuracy of Raman lidar water vapor calibration and its applicability to long-term measurements, *Appl. Opt.*, *47*, 5592–5603.

Leblanc, T., et al. (2011), Measurements of Humidity in the Atmosphere and Validation Experiments (MOHAVE)-2009: Overview of campaign operations and results, *Atmos. Meas. Tech.*, *4*, 2579–2605, doi:10.5194/amt-4-2579-2011.

Lee, B. D., R. D. Farley, and M. R. Hjelmfelt (1991), A numerical case-study of convection initiation along colliding convergence boundaries in northeast Colorado, *J. Atmos. Sci.*, *48*, 2350–2366.

LeMone, M. A., E. J. Zipser, and S. B. Trier (1998), The role of environmental shear and thermodynamic conditions in determining the structure and evolution of mesoscale convective systems during TOGA COARE, *J. Atmos. Sci.*, *55*, 3493–3518.

Lenschow, D. H., V. Wulfmeyer, and C. Senff (2000), Measuring second-through fourth-order moments in noisy data, *J. Atmos. Oceanic Technol.*, *17*, 1330–1347, doi:10.1175/1520-0426(2000)017<1330:MSTFOM>2.0.CO;2.

Li, J., W. W. Wolf, W. P. Menzel, W. Zhang, H.-L. Huang, and T. H. Achtor (2000), Global soundings of the atmosphere from ATOVS measurements: The algorithm and validation, *J. Appl. Meteorol.*, *39*, 1248–1268.

Li, Z., J.-P. Muller, and P. Cross (2003), Comparison of precipitable water vapor derived from radiosonde, GPS, and Moderate-Resolution Imaging Spectroradiometer measurements, *J. Geophys. Res.*, *108*(D20), 4651, doi:10.1029/2003JD003372.

Liepert, B. G., and M. Previdi (2009), Do models and observations disagree on the rainfall response to global warming?, *J. Clim.*, *22*, 3156–3166.

Liljegren, J. C. (2004), Improved retrievals of temperature and water vapor profiles with a twelve-channel radiometer, Eighth Symposium on Integrated Observing and Assimilation Systems for Atmosphere, Oceans, and Land Surface (IOAS-AOLS), Am. Meteorol. Soc., Seattle, Washington, 11–15 Jan.

Lima, M. A., and J. W. Wilson (2008), Convective storm initiation in a moist tropical environment, *Mon. Weather Rev.*, *136*, 1847–1864.

Linné, H., B. Hennemuth, J. Bösenberg, and K. Ertel (2007), Water vapour flux profiles in the convective boundary layer, *Theor. Appl. Climatol.*, *87*, 201–211.

Löhnert, U., and O. Maier (2012), Operational profiling of temperature using ground-based microwave radiometry at Payerne: Prospects and challenges, *Atmos. Meas. Tech.*, *5*, 1121–1134.

Löhnert, U., S. Crewell, and C. Simmer (2004), An integrated approach toward retrieving physically consistent profiles of temperature, humidity, and cloud liquid water, *J. Appl. Meteorol.*, *43*, 1295–1307.

Löhnert, U., E. van Meijgaard, H. K. Baltink, S. Gross, and R. Boers (2007), Accuracy assessment of an integrated profiling technique for operationally deriving profiles of temperature, humidity, and cloud liquid water, *J. Geophys. Res.*, *112*, D04205, doi:10.1029/2006JD007379.

Löhnert, U., S. Crewell, O. Krasnov, E. O'Connor, and H. Russchenberg (2008), Advances in continuously profiling the thermodynamic state of the boundary layer: Integration of measurements and methods, *J. Atmos. Oceanic Technol.*, *25*, 1251–1266, doi:10.1175/2007JTECHA961.1.

Löhnert, U., D. D. Turner, and S. Crewell (2009), Ground-based temperature and humidity profiling using spectral infrared and microwave observations. Part I: Simulated retrieval performance in clear-sky conditions, *J. Appl. Meteorol. Climatol.*, *48*, 1017–1032, doi:10.1175/2008JAMC2060.1.

Lucarini, V., and F. Ragone (2011), Energetics of climate models: Net energy balance and meridional enthalpy transport, *Rev. Geophys.*, *49*, RG1001, doi:10.1029/2009RG000323.

MacDonald, A., Y. Xie, and R. Ware (2002), Diagnosis of three-dimensional water vapour using slant observations from a GPS network, *Mon. Weather Rev.*, *130*, 386–397.

Machol, J. L., T. Ayers, K. T. Schwenz, K. W. Koenig, R. M. Hardesty, C. J. Senff, M. A. Krainak, J. B. Abshire, H. E. Bravo, and S. P. Sandberg (2004), Preliminary measurements with an automated compact differential absorption lidar for the profiling of water vapor, *Appl. Opt.*, *43*, 3110–3121.

Mapes, B. E., and P. Zuidema (1996), Radiative-dynamical consequences of dry tongues in the tropical troposphere, *J. Atmos. Sci.*, *53*, 620–638.

Martner, B. E., D. B. Wuertz, B. B. Stankov, R. G. Strauch, E. R. Westwater, K. S. Gage, W. L. Ecklund, C. L. Matin, and W. F. Dabberdt (1993), An evaluation of wind profiler, RASS, and microwave radiometer performance, *Bull. Am. Meteorol. Soc.*, *74*, 599–613.

Maschwitz, G., U. Löhnert, S. Crewell, T. Rose, and D. D. Turner (2013), Investigation of ground-based microwave radiometer calibration techniques at 530 hPa, *Atmos. Meas. Technol.*, *6*, 2641–2658, doi:10.5194/amt-6-2641-2013.

Masiello, G., et al. (2013), Comparison of IASI water vapour products over complex terrain with COPS campaign data, *Meteorol. Z.*, *22*, 471–487.

Mattis, I., A. Ansmann, D. Althausen, V. Jaenisch, U. Wandinger, D. Muller, Y. F. Arshinov, S. M. Bobrovnikov, and I. B. Serikov (2002), Relative-humidity profiling in the troposphere with a Raman lidar, *Appl. Opt.*, *41*, 6451–6462, doi:10.1364/AO.41.006451.

Matuura, M., Y. Masuda, H. Inuki, S. Kato, S. Fukao, T. Sato, and T. Tsuda (1986), Radio acoustic measurement of temperature profile in the troposphere and stratosphere, *Nature*, *323*, 426–428.

McNally, A. P., P. D. Watts, J. A. Smith, R. Engelen, G. A. Kelly, J. N. Thepaut, and M. Matricardi (2006), The assimilation of AIRS radiance data at ECMWF, *Q. J. R. Meteorol. Soc.*, *132*, 935–957, doi:10.1256/qj.04.171.

Melfi, S. H., J. D. Lawrence, and M. P. McCormick (1969), Observation of Raman scattering by water vapor in the atmosphere, *Appl. Phys. Lett.*, *15*, 295–297.

Melfi, S. H., D. Whiteman, and R. Ferrare (1989), Observation of atmospheric fronts using Raman lidar moisture measurements, *J. Appl. Meteorol.*, *28*, 789–806.

Menke, W. (1989), *Geophysical Data Analysis: Discrete Inverse Theory*, Academic Press, London.

Metzendorf, S., V. Wulfmeyer, A. Behrendt, F. Späth, and A. Riede (2015), Frequency-Agile Ti: Sapphire laser system with high power and high pulse energy for spectroscopic applications, Conference on Lasers and Electro-Optics, Munich, Germany, 21–25 Jun.

Meunier, V., D. D. Turner, and P. Kollias (2015), On the challenges of tomography retrievals of a 2D water vapor field using ground-based microwave radiometers: An observation system simulation experiment, *J. Atmos. Oceanic Technol.*, *32*, 116–130, doi:10.1175/JTECH-D-13-00194.1.

Mieruch, S., S. Noel, H. Bovensmann, and J. P. Burrows (2008), Analysis of global water vapour trends from satellite measurements in the visible spectral range, *Atmos. Chem. Phys.*, *8*, 491–504.

Milovac, J., K. Warrach Sagi, J. Ingwersen, A. Behrendt, F. Späth, H.-D. Wizemann, and V. Wulfmeyer (2014), Sensitivity of the WRF model to boundary-layer and land-surface parameterizations: Comparisons with differential absorption lidar and eddy covariance measurements, 7th International Scientific Conference on the Global Water and Energy Cycle, Den Haag, Netherlands, 14–17 Jul.

Montmerle, M. (2012), Optimization of the assimilation of radar data at the convective scale using specific background error covariances in precipitation, *Mon. Weather Rev.*, *140*, 3495–3506, doi:10.1175/MWR-D-12-00008.1.

Muller, C. L., L. Chapman, C. S. B. Grimmond, D. T. Young, and X. Cai (2013), Sensors and the city: A review of urban meteorological networks, *Int. J. Climatol.*, *33*, 1585–1600, doi:10.1002/joc.3678.

Muppa, S. K., A. Behrendt, F. Späth, V. Wulfmeyer, S. Metzendorf, and A. Riede (2015), Turbulent humidity fluctuations in the convective boundary layer: Case studies using water vapour DIAL measurements, *Boundary Layer Meteorol.*, in press.

Murphey, H. V., R. M. Wakimoto, C. Flamant, and D. E. Kingsmill (2006), Dryline on 19 June 2002 during IHOP. Part I: Airborne Doppler and LEANDRE II analyses of the thin line structure and convection initiation, *Mon. Weather Rev.*, *134*, 406–430.

Nakamura, H., K. Koizumi, and N. Mannoji (2004), Data assimilation of GPS precipitable water vapor into the JMA mesoscale numerical weather prediction model and its impact on rainfall forecasts, *J. Meteorol. Soc. Jpn.*, *82*, 441–452, doi:10.2151/jmsj.2004.441.

Nehrir, A. R., K. S. Repasky, J. L. Carlsten, M. D. Obland, and J. A. Shaw (2009), Water vapor profiling using a widely tunable, amplified diode-laser-based differential absorption lidar (DIAL), *J. Atmos. Oceanic Technol.*, *26*, 733–745.

Nehrir, A. R., K. S. Repasky, and J. L. Carlsten (2011), Eye-safe diode-laser-based micropulse differential absorption lidar (DIAL) for water vapor profiling in the lower troposphere, *J. Atmos. Oceanic Technol.*, *28*, 131–147.

Neiman, P. J., P. T. May, and M. A. Shapiro (1992), Radio acoustic sounding system (RASS) and wind profiler observations of lower and mid-tropospheric weather systems, *Mon. Weather Rev.*, *120*, 2298–2313.

Newsom, R. K., D. D. Turner, and J. E. M. Goldsmith (2013), Long-term evaluation of temperature profiles measured by an operational Raman lidar, *J. Atmos. Oceanic Technol.*, *30*, 1616–1634, doi:10.1175/JTECH-D-12-00138.1.

Niu, G.-Y., et al. (2012), The community Noah land surface model with multiparameterization options (Noah-MP): 1. Model description and evaluation with local-scale measurements, *J. Geophys. Res.*, *116*, D12109, doi:10.1029/2010JD015139.

O'Gorman, P. A., and T. Schneider (2009), The physical basis for increases in precipitation extremes in simulations of 21st-century climate change, *Proc. Natl. Acad. Sci. U.S.A.*, *106*, 14,773–14,777.

Ohring, G., B. Wielicki, R. Spencer, B. Emery, and R. Datla (2005), Satellite instrument calibration for measuring global climate change—Report of a workshop, *Bull. Am. Meteorol. Soc.*, *86*, 1303–1313.

Oki, T. (1999), The global water cycle, in *Global Energy and Water Cycles*, edited by K. A. Browning and R. J. Gurney, Cambridge Univ. Press, Cambridge, U. K.

Otkin, J. A., D. C. Hartung, D. D. Turner, R. A. Petersen, W. F. Feltz, and E. Janzon (2011), Assimilation of surface-based boundary layer profiler observations during a cool-season weather event using an Observing System Simulation Experiment. Part I: Analysis impact, *Mon. Weather Rev.*, *139*, 2309–2326.

Perler, D., A. Geiger, and F. Hurter (2011), 4D GPS water vapor tomography: New parameterized approaches, *J. Geod.*, *85*, 539–550, doi:10.1007/s00190-011-0454-2.

Peters, G., H. Timmermann, and H. Hinzpeter (1983), Temperature sounding in the planetary boundary layer by RASS—System analysis and results, *Int. J. Remote Sens.*, *4*, 49–63.

Petrova-Mayor, A., V. Wulfmeyer, and P. Weibring (2008), Development of an eye-safe solid-state tunable laser transmitter in the 1.4-1.5-μm wavelength region based on Cr^{4+}:YAG crystal for lidar applications, *Appl. Opt.*, *47*, 1522–1534.

Philipona, R., B. Dürr, A. Ohmura, and C. Ruckstuhl (2005), Anthropogenic greenhouse forcing and strong water vapor feedback increase temperature in Europe, *Geophys. Res. Lett.*, *32*, L19809, doi:10.1029/2005GL023624.

Platt, U. (1994), Differential optical absorption spectroscopy (DOAS), in *Monitoring by Spectroscopic Techniques*, edited by M. W. Sigrist, John Wiley, New York.

Poli, P., P. Moll, F. Rabier, G. Desroziers, B. Chapnik, L. Berre, S. B. Healy, E. Andersson, and F.-Z. El Guelai (2007), Forecast impact studies of zenith total delay data from European near real-time GPS stations in Météo France 4DVAR, *J. Geophys. Res.*, *112*, D06114, doi:10.1029/2006JD007430.

Poli, P., S. B. Healy, and D. P. Dee (2010), Assimilation of Global Positioning System radio occultation data in the ECMWF ERA-Interim reanalysis, *Q. J. R. Meteorol. Soc.*, *136*, 1972–1990, doi:10.1002/qj.722.

Pougatchev, N., T. August, X. Calbet, T. Hultberg, O. Oduleye, P. Schlüssel, B. Stiller, K. S. Germain, and G. Bingham (2009), IASI temperature and water vapor retrievals—Error assessment and validation, *Atmos. Chem. Phys.*, *9*, 6453–6458.

Radlach, M., A. Behrendt, and V. Wulfmeyer (2008), Scanning rotational Raman lidar at 355 nm for the measurement of tropospheric temperature fields, *Atmos. Chem. Phys., 8,* 159–169.

Randel, D. L., T. H. Vonder Haar, M. A. Ringerud, G. L. Stephens, T. J. Greenwald, and C. L. Combs (1996), A new global water vapor dataset, *Bull. Am. Meteorol. Soc., 6,* 1233–1246.

Reichardt, J., U. Wandinger, V. Klein, I. Mattis, B. Hilber, and R. Begbie (2012), RAMSES: German Meteorological Service autonomous Raman lidar for water vapor, temperature, aerosol, and cloud measurements, *Appl. Opt., 51,* 8111–8131.

Repasky, K. S., D. Moen, S. Spuler, A. R. Nehrir, and J. L. Carlsten (2013), Progress towards an autonomous field deployable diode-laser-based differential absorption lidar (DIAL) for profiling water vapor in the lower troposphere, *Remote Sens., 5,* 6241–6259, doi:10.3390/rs5126241.

Revercomb, H. E., et al. (2003), The Atmospheric Radiation Measurement Program's water vapor intensive observation periods: Overview, initial accomplishments, and future challenges, *Bull. Am. Meteorol. Soc., 84,* 217–236, doi:10.1175/BAMS-84-2-217.

Reverdy, M., J. Van Baelen, A. Walpersdorf, G. Dick, M. Hagen, and E. Richard (2009), Water vapour field retrieval with tomography software, *Ann. Meteorol., 44,* 144–145, Deutscher Wetterdienst: Offenbach. [Available at http://www.pa.op.dlr.de/icam2009/extabs.]

Richard, E., A. Buzzi, and G. Zängl (2007), Quantitative precipitation forecasting in the Alps: The advances achieved by the Mesoscale Alpine Programme, *Q. J. R. Meteorol. Soc., 133,* 831–846.

Roberts, R. D., et al. (2008), REFRACTT 2006, *Bull. Am. Meteorol. Soc., 89,* 1535–1548, doi:10.1175/2008BAMS2412.1.

Rocken, C., J. Johnson, T. Van Hove, and T. Iwabuchi (2005), Atmospheric water vapor and geoid measurements in the open ocean with GPS, *Geophys. Res. Lett., 32,* L12813, doi:10.1029/2005GL022573.

Rodgers, C. D. (2000), *Inverse Methods for Atmospheric Sounding, Theory Pract.,* 73 pp., World Scientific, Hackensack, N. J.

Rose, T., S. Crewell, U. Löhnert, and C. Simmer (2005), A network suitable microwave radiometer for operational monitoring of the cloudy atmosphere, *Atmos. Res., 75,* 183–200.

Rosen, R. D. (1999), The global energy cycle, in *Global Energy and Water Cycles,* edited by K. A. Browning and R. J. Gurney, Cambridge Univ. Press, Cambridge, U. K.

Rotach, M. W., et al. (2009), MAP D-PHASE: Real-time demonstration of weather forecast quality in the alpine region, *Bull. Am. Meteorol. Soc., 90,* 1321–1336, doi:10.1175/2009BAMS2776.1.

Rothman, L. S., et al. (2003), The HITRAN molecular spectroscopic database, *J. Quant. Spectros. Radiat. Transfer, 96,* 139–204.

Rothman, L. S., et al. (2005), The HITRAN 2004 molecular spectroscopic database: Edition of 2000 including updates through 2001, *J. Quant. Spectros. Radiat. Transfer, 82,* 5–44.

Rotunno, R., and R. A. Houze (2007), Lessons on orographic precipitation from the Mesoscale Alpine Programme, *Q. J. R. Meteorol. Soc., 133,* 811–830.

Santanello, J. A., C. Peters-Lidard, S. Kumar, C. Alonge, and W.-K. Tao (2009), A modeling and observational framework for diagnosing local land-atmosphere coupling on diurnal time scales, *J. Hydrometeor., 10,* 577–599.

Santanello, J. A., C. Peters-Lidard, and S. Kumar (2011), Diagnosing the sensitivity of local land-atmosphere coupling via the soil moisture-boundary layer interaction, *J. Hydrometeor., 12,* 766–786.

Schneider, T., P. A. O'Gorman, and X. J. Levine (2010), Water vapor and the dynamics of climate changes, *Rev. Geophys., 48,* RG3001, doi:10.1029/2009RG000302.

Schotland, R. M. (1966), Some observations of the vertical profile of water vapor by means of a ground based optical radar, in *Proceedings of the Fourth Symposium on Remote Sensing of the Environment,* vol. 271, Univ. of Mich., Ann Arbor.

Schulz, J., P. Schlüssel, and H. Graßl (1993), Water vapour in the atmospheric boundary layer over oceans from SSM/I measurements, *Int. J. Remote Sens., 14,* 2773–2789.

Schulz, J., et al. (2009), Operational climate monitoring from space: The EUMETSAT Satellite Application Facility on Climate Monitoring (CM-SAF), *Atmos. Chem. Phys., 9,* 1687–1709.

Schwitalla, T., and V. Wulfmeyer (2014), Radar data assimilation experiments using the IPM WRF rapid update cycle, *Meteorol. Z., 1,* 79–102, doi:10.1127/0941-2948/2014/0513.

Schwitalla, T., G. Zängl, H.-S. Bauer, and V. Wulfmeyer (2008), Systematic errors of QPF in low-mountain regions, *Meteorol. Z., 17,* 903–919.

Schwitalla, T., H.-S. Bauer, V. Wulfmeyer, and F. Aoshima (2011), High-resolution simulation over central Europe: Assimilation experiments with WRF 3DVAR during COPS IOP9c, *Q. J. R. Meteorol. Soc., 137,* 156–175, doi:10.1002/qj.721.

Seemann, S. W., E. E. Borbas, R. O. Knuteson, G. R. Stephenson, and H.-L. Huang (2008), Development of a global infrared land surface emissivity database for application to clear sky sounding retrievals from multispectral satellite radiance measurements, *J. Appl. Meteorol. Climatol., 47,* 108–123.

Seneviratne, S. I., T. Corti, E. L. Davin, M. Hirschi, E. B. Jaeger, I. Lehner, B. Orlowski, and A. J. Teuling (2010), Investigating soil moisture-climate interactions in a changing climate: A review, *Earth Sci. Rev., 99,* 125–161.

Senff, C., J. Bösenberg, and G. Peters (1994), Measurement of water vapor flux profiles in the convective boundary layer with lidar and radar RASS, *J. Atmos. Oceanic Technol., 11,* 85.

Sguerso, D., L. Labbouz, and A. Walpersdorf (2013), 14 years of GPS tropospheric delays in the French-Italian border region: A data base for meteorological and climatological analyses, International Workshop "The Role of Geomatics in Hydrogeological Risk", Padua, 26–28 Feb.

Sherwood, S. C., R. Roca, T. M. Weckwerth, and N. G. Andronova (2010), Tropospheric water vapor, convection, and climate, *Rev. Geophys., 48,* RG2001, doi:10.1029/2009RG000301.

Smith, W. L., W. F. Feltz, R. O. Knuteson, H. E. Revercomb, H. M. Woolf, and H. B. Howell (1999), The retrieval of planetary boundary layer structure using ground-based infrared spectral radiance measurements, *J. Atmos. Oceanic Technol., 16,* 323–333.

Soden, B. J., and I. M. Held (2006), An assessment of climate feedbacks in coupled ocean-atmosphere models, *J. Clim., 19,* 3354–3360.

Soden, B. J., D. D. Turner, B. M. Lesht, and L. M. Miloshevich (2004), An analysis of satellite, radiosonde, and lidar observations of upper tropospheric water vapor from the Atmospheric Radiation Measurement Program, *J. Geophys. Res., 109,* D04105, doi:10.1029/2003JD003828.

Soden, B. J., D. L. Jackson, V. Ramaswamy, M. D. Schwarzkopf, and Y. Huang (2005), The radiative signature of upper tropospheric moistening, *Science, 310,* 841–844.

Sokolovskiy, S. V. (2001), Tracking tropospheric radio occultation signals from low Earth orbit, *Radio Sci., 36,* 483–498, doi:10.1029/1999RS002305.

Sokolovskiy, S. V., Y.-H. Kuo, C. Rocken, W. S. Schreiner, D. Hunt, and R. A. Anthes (2006), Monitoring the atmospheric boundary layer by GPS radio occultation signals recorded in the open-loop mode, *Geophys. Res. Lett., 33,* L12813, doi:10.1029/2006GL025955.

Sokolovskiy, S., C. Rocken, W. Schreiner, D. Hunt, and J. Johnson (2009), Postprocessing of L1 GPS radio occultation signals recorded in open-loop mode, *Radio Sci., 44,* RS2002, doi:10.1029/2008RS003907.

Sokolovskiy, S., C. Rocken, W. Schreiner, and D. Hunt (2010), On the uncertainty of radio occultation inversions in the lower troposphere, *J. Geophys. Res., 115,* D22111, doi:10.1029/2010JD014058.

Späth, F., A. Behrendt, S. K. Muppa, S. Metzendorf, A. Riede, and V. Wulfmeyer (2014), High-resolution atmospheric water vapor measurements with a scanning differential absorption lidar, *Atmos. Chem. Phys. Discuss., 14,* 1–43, doi:10.5194/acpd-14-1-2014.

Späth, F., A. Behrendt, and V. Wulfmeyer (2015), Sensitivity of the Rayleigh-Doppler effect with respect to wavelength and backscatter coefficient, 27th International Laser Radar Conference, New York, 5–10 Jul.

Spuler, S. M., K. S. Repasky, B. Morley, D. Moen, M. Hayman, and A. R. Nehrir (2015), Field-deployable diode-laser-based differential absorption lidar (DIAL) for profiling water vapor, *Atmos. Meas. Tech.*, *8*, 1073–1087, doi:10.5194/amt-8-1073-2015.

Stankov, B. B., E. R. Westwater, and E. E. Gossard (1996), Use of wind profiler estimates of significant moisture gradients to improve humidity profile retrieval, *J. Atmos. Oceanic Technol.*, *13*, 1285–1290.

Stankov, B. B., E. E. Gossard, B. L. Weber, R. J. Lataitis, A. B. White, D. E. Wolfe, and D. C. Welsh (2003), Humidity gradient profiles from wind profiling radars using the NOAA/ETL advanced signal processing system (SPS), *J. Atmos. Oceanic Technol.*, *20*, 3–22.

Steinke, S., U. Löhnert, S. Crewell, and S. Liu (2014), Water vapor tomography with two microwave radiometers, *IEEE Geosci. Remote Sens. Lett.*, *11*, 419–423, doi:10.1109/LGRS.2013.2264354.

Stensrud, D. J., et al. (2009), Convective-scale warn-on-forecast system: A Vision for 2020, *Bull Am. Meteorol. Soc.*, *90*, 1487–1499, doi:10.1175/2009BAMS2795.1.

Stephens, G. L. (1994), *Remote Sensing of the Lower Atmosphere*, Oxford Univ. Press, Oxford.

Stephens, G. L., J. Li, M. Wild, C. A. Clayson, N. Loeb, S. Kato, T. L'Ecuyer, P. Stackhouse, M. Lebsock, and T. Andrews (2012), An update of Earth's energy balance in light of latest global observations, *Nat. Geosci.*, *5*, 691–696.

Stevens, B. (2005), Atmospheric moist convection, *Ann. Rev. Earth Plan. Sci.*, *33*, 605–643, doi:10.1146/annurev.earth.33.092203.122658.

Stokes, G. M., and S. E. Schwartz (1994), The Atmospheric Radiation Measurement (ARM) Program: Programmatic background and design of the cloud and radiation test bed, *Bull. Am. Meteorol. Soc.*, *75*, 1201–1221.

Stuhlmann, R., A. Rodriguez, S. Tjemkes, J. Grandell, A. Arriaga, J. L. Bézy, D. Aminou, and P. Bensi (2005), Plans for EUMETSAT's third generation Meteosat geostationary satellite programme, *Adv. Space Res.*, *36*, 375–981.

Stull, R. B. (1988), *An Introduction to Boundary Layer Meteorology*, Springer, Berlin.

Su, Z., et al. (2014), First results of the Earth observation Water Cycle Multi-mission Observation Strategy (WACMOS), *Int. J. Appl. Earth Obs. Geoinf.*, *26*, 270–285.

Summa, D., P. Di Girolamo, H. Bauer, and V. Wulfmeyer (2004), End-to-end simulation of the performance of WALES: Retrieval module, Proceedings of the 22nd International Laser Radar Conference, July 2004, ESA SP-561, 1015–1018.

Sun, J. (2005), Convective-scale assimilation of radar data: Progress and challenges, *Q. J. R. Meteorol. Soc.*, *131*, 3439–3463, doi:10.1256/qj.05.149.

Tarantola, A. (2005), *Inverse Problem Theory and Methods for Model Parameter Estimation*, SIAM, Philadelphia.

Taylor, C. M., R. A. M. de Jeu, F. Guichard, P. P. Harris, and W. A. Dorigo (2012), Afternoon rain more likely over dry soils, *Nature*, *489*, 423–426, doi:10.1038/nature11377.

Teke, K., et al. (2011), Multi-technique comparison of troposphere zenith delays and gradients during CONT08, *J. Geodesy*, *85*, 395–413, doi:10.1007/s00190-010-0434-y.

Theopold, F. A., and J. Bösenberg (1993), Differential absorption lidar measurements of atmospheric temperature profiles: Theory and experiment, *J. Atmos. Oceanic Technol.*, *10*, 165–179, doi:10.1175/1520-0426(1993)010<0165:DALMOA>2.0.CO;2.

Thorne, P. W., et al. (2013), GCOS reference upper air network (GRUAN): Steps towards assuring future climate records, *AIP Conf. Proc.*, *1552*, 1042–1047, doi:10.1063/1.4821421.

Trenberth, K. E., and G. R. Asrar (2014), Challenges and opportunities in water cycle research: WCRP contributions, *Surv. Geophys.*, *35*, 515–532, doi:10.1007/s10712-012-9214-y.

Trenberth, K. E., and L. Smith (2005), The mass of the atmosphere: A constraint on global analyses, *J. Clim.*, *18*, 864–875.

Trenberth, K. E., and L. Smith (2009), The three dimensional structure of the atmospheric energy budget: Methodology and evaluation, *Clim. Dyn.*, *32*, 1065–1079, doi:10.1007/s00382-008-0389-3.

Trenberth, K. E., A. Dai, R. M. Rasmussen, and D. B. Parsons (2003), The changing character of precipitation, *Bull. Am. Meteorol. Soc.*, *84*, 1205–1217, doi:10.1175/BAMS-84-9-1205.

Trenberth, K. E., L. Smith, T. Qian, A. Dai, and J. Fasullo (2007), Estimates of the global water budget and its annual cycle using observational and model data, *J. Hydrometeor.*, *8*, 758–769.

Trenberth, K. E., J. T. Fasullo, and J. Kiehl (2009), Earth's global energy budget, *Bull. Am. Meteorol. Soc.*, *90*, 311–323.

Trenberth, K. E., J. T. Fasullo, and J. Mackaro (2011), Atmospheric moisture transports from ocean to land and global energy flows in reanalyses, *J. Clim.*, *24*, 4907–4924, doi:10.1175/2011JCLI4171.1.

Troller, M., A. Geiger, E. Brockmann, J.-M. Bettems, B. Burki, and H.-G. Kahle (2006), Tomographic determination of the spatial distribution of water vapour using GPS observations, *Adv. Space Res.*, *37*, 2211–2217, doi:10.1016/j.asr.2005.07.002.

Tsuda, T., Y. Masuda, H. Inuki, K. Takahashi, T. Takami, T. Sato, S. Fukao, and S. Kato (1989), High time resolution monitoring of tropospheric temperature with a Radio Acoustic Sounding System (RASS), *Pure Appl. Geophys.*, *130*, 497–507.

Tsuda, T., M. Miyamoto, and J. Furumoto (2001), Estimation of a humidity profile using turbulence echo characteristics, *J. Atmos. Oceanic Technol.*, *18*, 1214–1222.

Turner, D. D., and J. E. M. Goldsmith (1999), Twenty-four-hour Raman lidar water vapor measurements during the Atmospheric Radiation Measurement Program's 1996 and 1997 water vapor intensive observation periods, *J. Atmos. Oceanic Technol.*, *16*, 1062–1076.

Turner, D. D., and U. Löhnert (2014), Information content and uncertainties in thermodynamic profiles and liquid cloud properties retrieved from the ground-based Atmospheric Emitted Radiance Interferometer (AERI), *J. Appl. Meteorol. Climatol.*, *53*, 752–771, doi:10.1175/JAMC-D-13-0126.1.

Turner, D. D., R. A. Ferrare, L. A. Heilman Brasseur, W. F. Feltz, and T. P. Tooman (2002), Automated retrievals of water vapor and aerosol profiles over Oklahoma from an operational Raman lidar, *J. Atmos. Oceanic Technol.*, *19*, 37–50.

Turner, D. D., B. M. Lesht, S. A. Clough, L. C. Liljegren, H. E. Revercomb, and D. C. Tobin (2003), Dry bias and variability in Vaisala RS80-H radiosondes: The ARM experience, *J. Atmos. Oceanic Technol.*, *20*, 117–132.

Turner, D. D., D. C. Tobin, S. A. Clough, P. D. Brown, R. G. Ellingson, E. J. Mlawer, R. O. Knuteson, H. E. Revercomb, T. R. Shippert, and W. L. Smith (2004), The QME AERI LBLRTM: A closure experiment for downwelling high spectral resolution infrared radiance, *J. Atmos. Sci.*, *61*, 2657–2675, doi:10.1175/JAS3300.1.

Turner, D. D., R. A. Ferrare, V. Wulfmeyer, and A. J. Scarino (2014a), Aircraft evaluation of ground-based Raman lidar water vapor turbulence profiles in convective mixed layers, *J. Atmos. Oceanic Technol.*, *31*, 1078–1088, doi:10.1175/JTECH-D-13-00075.1.

Turner, D. D., V. Wulfmeyer, L. K. Berg, and J. H. Schween (2014b), Water vapor turbulence profiles in stationary continental convective mixed layers, *J. Geophys. Res. Atmos.*, *119*, 1–15, doi:10.1002/2014JD022202.

Uppala, S. M., et al. (2005), The ERA-40 reanalysis, *Q. J. R. Meteorol. Soc.*, *131*, 2961–3012, doi:10.1256/qj.04.176.

Van Baelen, J., J.-P. Aubagnac, and A. Dabas (2005), Comparison of near-real time estimates of integrated water vapor derived with GPS, radiosondes, and microwave radiometer, *J. Atmos. Oceanic Technol.*, *22*, 201–210.

Van Baelen, J., M. Reverdy, F. Tridon, L. Labbouz, G. Dick, M. Bender, and M. Hagen (2011), On the relationship between water vapour field evolution and precipitation systems lifecycle, *Q. J. R. Meteorol. Soc.*, *137*, 204–223, doi:10.1002/qj.785.

Van den Hurk, B., M. Best, P. Dirmeyer, A. Pitman, J. Polcher, and J. Santanello (2011), Acceleration of land surface model development over a decade of Glass, *Bull. Am. Meteorol. Soc.*, *92*, 1593–1600.

Vaughan, G., D. P. Wareing, S. J. Pepler, L. Thomas, and V. Mitev (1993), Atmospheric temperature profiles made by rotational Raman scattering, *Appl. Opt.*, *32*, 2758–2764.

Vaughan, J. M., N. J. Geddes, P. H. Flamant, and C. Flesia (1998), Establishment of a backscatter coefficient and atmospheric data base, ESA-CR, 12510/97/NL/RE.

Vautard, R., et al. (2013), The simulation of European heat waves from an ensemble of regional climate models within the EURO-CORDEX project, *Clim. Dyn.*, *41*, 2555–2575, doi:10.1007/s00382-013-1714-z.

Vergados, P., A. J. Mannucci, and C. O. Ao (2014), Assessing the performance of GPS radio occultation measurements in retrieving tropospheric humidity in cloudiness: A comparison study with radiosondes, ERA-Interim, and AIRS data sets, *J. Geophys. Res. Atmos.*, *119*, 7718–7731, doi:10.1002/2013JD021398.

Vergados, P., A. J. Mannucci, C. O. Ao, J. H. Jiang, and H. Su (2015), On the comparisons of tropical relative humidity in the lower and middle troposphere among COSMIC radio occultations and MERRA and ECMWF data sets, *Atmos. Meas. Tech.*, *8*, 1789–1797, doi:10.5194/amt-8-1789-2015.

Vogelmann, H., and T. Trickl (2008), Wide-range sounding of free-tropospheric water vapor with a differential-absorption lidar (DIAL) at a high-altitude station, *Appl. Opt.*, *47*, 2116–2132.

Wagner, G., V. Wulfmeyer, and A. Behrendt (2011), Detailed performance modeling of a pulsed high-power single-frequency Ti:Sapphire laser, *Appl. Opt.*, *50*, 5921–5937, doi:10.1364/AO.50.005921.

Wagner, G., V. Wulfmeyer, F. Späth, A. Behrendt, and M. Schiller (2013a), Performance and specifications of a pulsed high-power single-frequency Ti:Sapphire laser for water-vapor differential absorption lidar, *Appl. Opt.*, *52*, 2454–2469, doi:10.1364/AO.52.002454.

Wagner, T., S. Beirle, H. Sihler, and K. Mies (2013b), A feasibility study for the retrieval of the total column precipitable water vapour from satellite observations in the blue spectral range, *Atmos. Meas. Tech.*, *6*, 2593–2605, doi:10.5194/amt-6-2593-2013.

Wakimoto, R. M., H. V. Murphey, E. V. Browell, and S. Ismail (2006), The "Triple Point" on 24 May 2002 during IHOP. Part I: Airborne Doppler and LASE analyses of the frontal boundaries and convection initiation, *Mon. Weather Rev.*, *134*, 231–250.

Walpersdorf, A., O. Bock, E. Doerflinger, F. Masson, J. Van Baelen, A. Somieski, and B. Buerki (2004), Data analysis of a dense GPS network operated during the ESCOMPTE campaign: First results, *Phys. Chem. Earth*, *29*, 201–211, doi:10.1016/j.pce.2004.01.002.

Wandinger, U. (2005), Raman lidar, in *Lidar: Range-Resolved Optical Remote Sensing of the Atmosphere*, edited by C. Weitkamp, Springer, New York.

Wang, J., L. Zhang, A. Dai, T. Van Hove, and J. Van Baelen (2007), A near-global 2-hourly data set of atmospheric precipitable water from ground-based GPS measurements, *J. Geophys. Res.*, *112*, D11107, doi:10.1029/2006JD007529.

Wang, K., and R. E. Dickinson (2012), A review of global terrestrial evapotranspiration: Observation, modeling, climatology, and climatic variability, *Rev. Geophys.*, *50*, RG2005, doi:10.1029/2011RG000373.

Ware, R., et al. (1996), GPS sounding of the atmosphere from low Earth orbit: Preliminary results, *Bull. Am. Meteorol. Soc.*, *77*, 19–38.

Warrach-Sagi, K., and V. Wulfmeyer (2010), Streamflow data assimilation for soil moisture analysis, *Geosci. Model Dev.*, *3*, 1–12, doi:10.5194/gmd-3-1-2010.

Warrach-Sagi, K., T. Schwitalla, V. Wulfmeyer, and H.-S. Bauer (2013), Evaluation of a climate simulation based on the WRF-NOAH model system: Precipitation in Germany, *Clim. Dyn.*, *41*, 755–774, doi:10.1007/s00382-013-1727-7.

Weckwerth, T. M., and D. Parsons (2006), A review of convection initiation and motivation for IHOP 2002, *Bull. Am. Meteorol. Soc.*, *134*, 5–22.

Weckwerth, T. M., J. W. Wilson, and R. M. Wakimoto (1996), Thermodynamic variability within the convective boundary layer due to horizontal convective rolls, *Mon. Weather Rev.*, *124*, 769–784.

Weckwerth, T. M., V. Wulfmeyer, R. M. Wakimoto, R. M. Hardesty, J. W. Wilson, and R. M. Banta (1999), NCAR-NOAA lower tropospheric water vapor workshop, *Bull. Am. Meteorol. Soc.*, *80*, 2339–2357.

Weckwerth, T. M., C. R. Pettet, F. Fabry, S. Park, M. A. LeMone, and J. W. Wilson (2005), Radar refractivity retrieval: Validation and application to short-term forecasting, *J. Appl. Meteorol.*, *44*, 285–300.

Weckwerth, T. M., L. J. Bennett, L. J. Miller, J. Van Baelen, P. Di Girolamo, A. M. Blyth, and T. J. Hertneky (2014), An observational and modeling study of the processes leading to deep, moist convection in complex terrain, *Mon. Weather Rev.*, *142*, 2687–2708, doi:10.1175/MWR-D-13-00216.1.

Weisman, M. L., and J. B. Klemp (1982), The dependence of numerically simulated convective storms on vertical wind shear and buoyancy, *Mon. Weather Rev.*, *110*, 504–520.

Wentz, F. J., L. Ricciardulli, K. Hilburn, and C. Mears (2007), How much more rain will global warming bring?, *Science*, *317*, 233–235.

Westwater, E. R., and O. N. Strand (1968), Statistical information content of radiation measurements used in indirect sensing, *J. Atmos. Sci.*, *25*, 750–758.

Westwater, E. R., B. B. Stankov, D. Cimini, Y. Han, J. A. Shaw, B. M. Lesht, and C. N. Long (2003), Radiosonde humidity soundings and micro-wave radiometers during Nauru99, *J. Atmos. Oceanic Technol.*, *20*, 953–971, doi:10.1175/1520-0426(2003)20<953:RHSAMR>2.0.CO;2.

Whiteman, D. N. (2003a), Examination of the traditional Raman lidar technique: I. Evaluating the temperature-dependent lidar equations, *Appl. Opt.*, *42*, 2571–2592.

Whiteman, D. N. (2003b), Examination of the traditional Raman lidar technique: II. Evaluating the ratios for water vapor and aerosols, *Appl. Opt.*, *42*, 2593–2608.

Whiteman, D. N., S. H. Melfi, and R. A. Ferrare (1992), Raman lidar system for the measurement of water vapor and aerosols in the Earth's atmosphere, *Appl. Opt.*, *31*, 3068–3082.

Whiteman, D. N., et al. (2001), Raman lidar measurements of water vapor and cirrus clouds during the passage of Hurricane Bonnie, *J. Geophys. Res.*, *106*, 5211–5225, doi:10.1029/2000JD900621.

Whiteman, D. N., et al. (2006a), Raman lidar measurements during the International H_2O Project. Part I: Instrumentation and analysis techniques, *J. Atmos. Oceanic Technol.*, *23*, 157–169.

Whiteman, D. N., et al. (2006b), Raman water vapor lidar measurements during the International H_2O Project. Part II: Case studies, *J. Atmos. Oceanic Technol.*, *23*, 170–183.

Whiteman, D. N., D. Venable, and E. Landulfo (2011), Comments on "Accuracy of Raman lidar water vapor calibration and its applicability to long-term measurements", *Appl. Opt.*, *50*, 2170–2176.

Wickert, J., and G. Gendt (2006), Fernerkundung der Erdatmosphäre mit GPS, *Promet*, *32*, 80–88.

Wickert, J., T. Schmidt, G. Beyerle, R. König, S. Heise, L. Grunwaldt, G. Michalak, C. Reigber, and N. Jakowski (2004), The radio occultation experiment aboard CHAMP: Operational data analysis and validation of vertical profiles, *J. Meteorol. Soc. Jpn.*, *82*, 381–395.

Wickert, J., et al. (2009), GPS radio occultation: Results from CHAMP, GRACE and FORMOSAT-3/COSMIC, *Terr. Atmos. Oceanic Sci.*, *20*, 35–50.

World Meteorological Organization (2004), Statement of guidance regarding how well satellites and in situ sensor capabilities meet WMO user requirements in several application areas, TD No. 1052.

World Meteorological Organization (2005), Implementation plan for the evolution of space and surface-based sub-systems of the GOS, TD No. 1267.

Wöhling, T., S. Gayler, E. Priesack, J. Ingwersen, H.-D. Wizemann, P. Högy, M. Cuntz, S. Attinger, V. Wulfmeyer, and T. Streck (2013), Multiresponse, multiobjective calibration as a diagnostic tool to compare accuracy and structural limitations of five coupled soil-plant models and CLM3.5, *Water Resour. Res.*, *49*, 8200–8221, doi:10.1002/2013WR014536.

Wulfmeyer, V. (1998), Ground-based differential absorption lidar for water-vapor and temperature profiling: Requirements, development, and specifications of a high-performance laser transmitter, *Appl. Opt.*, *37*, 3804–3824.

Wulfmeyer, V. (1999a), Investigation of turbulent processes in the lower troposphere with water-vapor DIAL and Radar-RASS, *J. Atmos. Sci.*, *56*, 1055–1076.

Wulfmeyer, V. (1999b), Investigations of humidity skewness and variance profiles in the convective boundary layer and comparison of the latter with large eddy simulation results, *J. Atmos. Sci.*, *56*, 1077–1087.

Wulfmeyer, V., and J. Bösenberg (1996), Single-mode operation of an injection-seeded alexandrite ring laser for application in water-vapor and temperature differential absorption lidar, *Opt. Lett.*, *21*, 1150–1152.

Wulfmeyer, V., and J. Bösenberg (1998), Ground-based differential absorption lidar for water-vapor profiling: Assessment of accuracy, resolution, and meteorological applications, *Appl. Opt.*, *37*, 3825–3844.

Wulfmeyer, V., and C. Walther (2001a), Future performance of ground-based and airborne water vapor differential absorption lidar. I: Overview and theory, *Appl. Opt.*, *40*, 5304–5320.

Wulfmeyer, V., and C. Walther (2001b), Future performance of ground-based and airborne water vapor differential absorption lidar. II: Simulations of the precision of a near-infrared, high-power system, *Appl. Opt.*, *40*, 5321–5336.

Wulfmeyer, V., J. Bösenberg, S. Lehmann, C. Senff, and S. Schmitz (1995), Injection-seeded alexandrite ring laser: Performance and application in a water-vapor differential absorption lidar, *Opt. Lett.*, *20*, 638–640.

Wulfmeyer, V., et al. (2003), Workshop report lidar research network water vapor and wind, *Meteorol. Z.*, *12*, 5–24.

Wulfmeyer, V., H. Bauer, P. Di Girolamo, and C. Serio (2005), Comparison of active and passive remote sensing from space: An analysis based on the simulated performance of IASI and spaceborne differential absorption lidar, *Remote Sens. Environ.*, *95*, 211–230.

Wulfmeyer, V., H.-S. Bauer, M. Grzeschik, A. Behrendt, F. Vandenberghe, E. V. Browell, S. Ismail, and R. Ferrare (2006), 4-dimensional variational assimilation of water-vapor differential absorption lidar data: The first case study within IHOP_2002, *Mon. Weather Rev.*, *134*, 209–230.

Wulfmeyer, V., et al. (2008), The convective and orographically-induced precipitation study: A research and development project of the World Weather Research Program for improving quantitative precipitation forecasting in low-mountain regions, *Bull. Am. Meteorol. Soc.*, *89*, 1477–1486, doi:10.1175/2008BAMS2367.1.

Wulfmeyer, V., D. D. Turner, S. Pal, and E. Wagner (2010), Can water vapour Raman lidar resolve profiles of turbulent variables in the convective boundary layer?, *Bound.-layer Meteorol.*, *136*, 253–284, doi:10.1007/s10546-010-9494-z.

Wulfmeyer, V., et al. (2011), The Convective and Orographically Induced Precipitation Study (COPS): The scientific strategy, the field phase, and first highlights, *Q. J. R. Meteorol. Soc.*, *137*, 3–30, doi:10.1002/qj.752.

Wulfmeyer, V., A. Behrendt, H.-S. Bauer, T. Schwitalla, and K. Warrach-Sagi (2014a), Observations and simulations of soil-vegetation-atmosphere feedback with a new lidar sensor synergy and the WRF-NOAH-MP model in the grey zone, 7th International Scientific Conference on the Global Water and Energy Cycle, Den Haag, Netherlands, 14–17 Jul.

Wulfmeyer, V., K. Warrach-Sagi, T. Schwitalla, H.-S. Bauer, and J. Milovac (2014b), Towards seamless mesoscale prediction of the land system for Europe, The World Weather Open Science Conference, Montreal, Canada, 16–21 Aug.

Wulfmeyer, V., et al. (2014c), Consistent hydro-meteorological large eddy simulation of water budgets in mesoscale catchments: Overkill or necessity?, AGU Chapman Conference, Luxembourg City, Luxembourg, 23–26 Sept.

Xie, F., S. Syngergaard, E. R. Kursinski, and B. Herman (2006), An approach for retrieving marine boundary layer refractivity from GPS occultation data in the presence of superrefraction, *J. Atmos. Oceanic Technol.*, *23*, 1629–1644.

Xie, F., D. L. Wu, C. O. Ao, A. J. Mannucci, and E. R. Kursinski (2012), Advances and limitations of atmospheric boundary layer observations with GPS occultation over Southeast Pacific Ocean, *Atmos. Chem. Phys.*, *12*, 903–918, doi:10.5194/acp-12-903.

Yu, X., and T.-Y. Lee (2010), Role of convective parameterization in simulations of a convection band at grey-zone resolutions, *Tellus A*, *62*, 617–632, doi:10.1111/j.1600-0870.2010.00470.x.

Zhang, M., and F. Zhang (2012), E4DVar: Coupling an ensemble Kalman filter with four-dimensional variational data assimilation in a limited-area weather prediction model, *Mon. Weather Rev.*, *140*, 587–600, doi:10.1175/MWR-D-11-00023.1.

Zhang, Y., W. B. Rossow, and P. W. Stackhouse Jr. (2006), Comparison of different global information sources used in surface radiative flux calculation: Radiative properties of the near-surface atmosphere, *J. Geophys. Res.*, *111*, D13106, doi:10.1029/2005JD006873.

Zhou, D. K., A. M. Larar, X. Liu, W. L. Smith, L. L. Strow, P. Yang, P. Schlüssel, and X. Calbet (2011), Global land surface emissivity retrieved from satellite ultraspectral IR measurements, *IEEE Trans. Geosci. Remote Sens.*, *49*, 1277–1290.

Zhou, L., R. E. Dickinson, Y. Tian, M. Jin, K. Ogawa, H. Yu, and T. Schmugge (2003), A sensitivity study of climate and energy balance simulations with use of satellite-derived emissivity data over northern Africa and the Arabian Peninsula, *J. Geophys. Res.*, *108*(D24), 4795, doi:10.1029/2003JD004083.

Ziegler, C. L., and E. N. Rasmussen (1998), The initiation of moist convection at the dryline: Forecasting issues from a case study perspective, *Weather Forecasting*, *13*, 1106–1131.

Zolina, O., C. Simmer, K. Belyaev, S. K. Gulev, and P. Koltermann (2013), Changes in the duration of European wet and dry spells during the last 60 years, *J. Clim.*, *26*, 2022–2047, doi:10.1175/JCLI-D-11-00498.1.

Zus, F., M. Grzeschik, H.-S. Bauer, and V. Wulfmeyer (2008), Design and optimization of the IPM MM5 GPS slant path 4DVAR system, *Meteorol. Z.*, *17*, 867–885, doi:10.1127/0941-2948/2008/0339.

Zus, F., J. Wickert, H.-S. Bauer, T. Schwitalla, and V. Wulfmeyer (2011), Experiments of GPS slant path data assimilation with an advanced MM5 4DVAR system, *Meteorol. Z.*, *20*, 173–184, doi:10.1127/0941-2948/2011/0232.

Zus, F., M. Bender, Z. Deng, G. Dick, S. Heise, M. Shang-Guan, and J. Wickert (2012), A methodology to compute GPS slant total delays in a numerical weather model, *Radio Sci.*, *47*, RS2018, doi:10.1029/2011RS004853.

Zus, F., G. Dick, J. Douša, S. Heise, and J. Wickert (2014), The rapid and precise computation of GPS slant total delays and mapping factors utilizing a numerical weather model, *Radio Sci.*, *49*, 207–216, doi:10.1002/2013RS005280.